



저작자표시-비영리-변경금지 2.0 대한민국

이용자는 아래의 조건을 따르는 경우에 한하여 자유롭게

- 이 저작물을 복제, 배포, 전송, 전시, 공연 및 방송할 수 있습니다.

다음과 같은 조건을 따라야 합니다:



저작자표시. 귀하는 원저작자를 표시하여야 합니다.



비영리. 귀하는 이 저작물을 영리 목적으로 이용할 수 없습니다.



변경금지. 귀하는 이 저작물을 개작, 변형 또는 가공할 수 없습니다.

- 귀하는, 이 저작물의 재이용이나 배포의 경우, 이 저작물에 적용된 이용허락조건을 명확하게 나타내어야 합니다.
- 저작권자로부터 별도의 허가를 받으면 이러한 조건들은 적용되지 않습니다.

저작권법에 따른 이용자의 권리는 위의 내용에 의하여 영향을 받지 않습니다.

이것은 [이용허락규약\(Legal Code\)](#)을 이해하기 쉽게 요약한 것입니다.

[Disclaimer](#)

공학박사학위논문

Carbon nanotube based
thermo-electrochemical cells
for harvesting waste heat

폐열 수집을 위한 탄소나노튜브 기반
열전기화학 전지

2015년 2월

서울대학교 대학원

기계항공공학부

임 형 욱

Abstract

Carbon nanotube based thermo-electrochemical cells for harvesting waste heat

Hyeongwook Im

School of Mechanical and Aerospace Engineering

Seoul National University

Harvesting energy from low-grade waste heat has received much attention due to the world's growing energy problem. Critical needs for harnessing waste heat are to improve the efficiency of thermal energy harvesters and decrease their cost. Thermal electrochemical cell (also known as thermogalvanic cell or thermocell) that provides electrical power originating from the temperature dependence of electrochemical redox potentials is becoming attractive alternative for low-grade heat recovery. A thermocell consists of two electrodes operating at different temperatures and placed in contact with redox-based electrolyte. The inter-electrode temperature difference causes difference in the redox potential of the electrolyte, generating electrical power. The thermally generated potential derives

electrons in the external circuit and ions in the electrolyte, thus electrical current and power can be delivered.

A large source of waste heat can be found in power plants or various industrial facilities where large amounts of waste heat are lost through numerous pipes that carry hot fluid. To effectively harvest waste thermal energy from these arbitrary shaped heat sources, plastic thermocells with all pliable materials, such as polyethylene terephthalate (PET), fabrics, and wires were developed. The plastic thermocells are flexible enough to be wrapped around cylindrical shapes and to be wearable on the human body. The electrical energy generated from waste pipe heat using a serial array of the thermocells and voltage converters can power a typical commercial light emitting diode (LED). Also, the thermocell charges up a capacitor when worn on thermocell embedded T-shirt by a person.

Thermocells have major advantages of simple design, direct thermal-to-electric energy conversion, zero carbon emission and low cost, however they presently have no commercial applications because of their low energy conversion efficiencies and low areal output power of thermocells. Therefore, a significant efficiency increase is required for thermocells to become commercially attractive. The deployed optimization strategies to improve thermocell efficiency involve use of CNT aerogel sheets as electrodes, removal of low activity carbonaceous impurities that limit electron transfer kinetics, decoration of CNT sheets with catalytic platinum nanoparticles, mechanical compression of nanotube sheets to tune

conductivity and porosity, and the utilization of cylindrical cell geometry. The output power density generated by thermocell with the optimized aerogel sheet reached 6.6 W/m^2 , which corresponds to a Carnot-relative efficiency (η_r) of 4.2%. To date this η_r is the highest reported value in thermocells.

Keywords: Carbon nanotube, Thermo-electrochemical cell, Harvesting waste heat, High efficiency thermocell, Flexible thermocell film

Student number: 2008-30863

Contents

| | |
|--|-----|
| Abstract..... | i |
| Contents..... | iv |
| List of tables | vi |
| List of figures | vii |
| Chapter 1. Introduction..... | 1 |
| 1.1 Motivation & research background..... | 1 |
| 1.2 Thesis objectives | 2 |
| Chapter 2. Thermocell and Carbon nanotubes | 4 |
| 2.1 Thermocell fundamentals | 4 |
| 2.1.1 Principle of operation | 4 |
| 2.1.2 Open-circuit potential..... | 6 |
| 2.1.3 Figure of merit and power conversion efficiency..... | 8 |
| 2.2 Carbon nanotubes | 10 |
| 2.2.1 Geometric structure of CNT | 12 |
| 2.2.2 Synthesis and purification of pristine CNT | 15 |
| 2.2.3 Raman spectroscopy for CNT characterization..... | 15 |
| Chapter 3. Flexible Thermocell Film | 18 |
| 3.1 Introduction | 18 |
| 3.2 Chapter aims..... | 19 |
| 3.3 Experimental setup..... | 19 |
| 3.3.1 Preparation of CNT-textile electrodes..... | 19 |
| 3.3.2 Fabrication of plastic thermocells | 21 |
| 3.3.3 Thermocell testing and characterization..... | 23 |
| 3.4 Results and discussion..... | 24 |
| 3.4.1 Material characteristics..... | 24 |

| | |
|--|------------|
| 3.4.2 Enhanced electrode performance with CNT | 30 |
| 3.4.3 Characterization of plastic thermocell..... | 39 |
| 3.4.4 Harvesting energy from human body and heat pipe..... | 51 |
| 3.5 Conclusion..... | 57 |
| Chapter 4. CNT Aerogel Sheet Electrodes for Thermocells .. | 58 |
| 4.1 Introduction | 58 |
| 4.2 Chapter Aims..... | 59 |
| 4.3 Experimental setup..... | 59 |
| 4.3.1 Preparation and post-treatment of CNT aerogel sheet electrodes | 59 |
| 4.3.2 Flow cell configuration for evaluation of diffusion limiting current | 62 |
| 4.3.3 Thermocell testing and characterization..... | 66 |
| 4.4 Results and discussion..... | 68 |
| 4.4.1 Determination of mass transfer coefficient CNT aerogel sheet | 68 |
| 4.4.2 Thermal optimization of surface purity of sheet electrode..... | 74 |
| 4.4.3 Mechanical compression for optimization of ohmic resistance | 85 |
| 4.4.4 Decoration CNT aerogel sheet with Pt nanoparticles..... | 91 |
| 4.4.5 Cylinder-type thermocell configuration | 97 |
| 4.5 Conclusion..... | 103 |
| Chapter 5. Discussion and concluding remarks | 105 |
| Bibliography | 108 |
| 초 록 | 121 |

List of tables

Table 1. Physical properties of CNT and their applications.

Table 2. Physical properties of the electrolyte at 20°C.

Table 3. Summary of data obtained from harvesting experiments performed using cylindrical thermocell.

List of figures

- Figure 2-1. Illustration of a thermocell operation of an aqueous electrolyte during power generation.
- Figure 2-2. Classification and structure of CNTs.
- Figure 3-1. Optical photograph of dipping process for CNT coating on ACT.
- Figure 3-2. Schematic depicting the structure of the flexible thermocell.
- Figure 3-3. Photograph of the fabricated plastic thermocell.
- Figure 3-4. SEM images of the a) pristine and b) CNT coated activation textile.
- Figure 3-5. Nitrogen adsorption isotherms at 77 K for ACT and CNT-ACT samples.
- Figure 3-6. The cumulative pore volume in the mesopore range derived non-local density functional theory (NLDFT).
- Figure 3-7. Resistance stability test for different bending curvatures.
- Figure 3-8. Dependence of open-circuit potential on the temperature difference between hot and cold electrodes.
- Figure 3-9. Thermocell discharge and specific output power as a function of the current density of pristine the ACT and C-ACT electrodes.
- Figure 3-10. Comparison of three internal resistances of the thermocell with pristine ACT and CNT coated ACT electrodes.
- Figure 3-11. Cyclic voltammograms of pristine and CNT coated ACT sheet.
- Figure 3-12. Nyquist impedance plots for ACT and C-ACT electrodes. Inset shows the Randle's equivalent circuit.
- Figure 3-13. Sheet resistance of the two textile electrodes.

- Figure 3-14. Time-dependent overall internal resistance change of the thermocell with ACT and C-ACT electrodes.
- Figure 3-15. Dependence of cell potential on current with increasing time from the start of energy harvesting. The inset shows the dependence of internal resistance on time.
- Figure 3-16. Plots of cell potential (solid square) and specific output power (open square) versus current density at steady state.
- Figure 3-17. E-I curves and output power versus current density.
- Figure 3-18. Maximum specific output power with respect to the temperature difference.
- Figure 3-19. Dependence of internal resistance on operating temperature.
- Figure 3-20. Mass transport resistance as a function of operating temperature.
- Figure 3-21. Dependence of open-circuit voltage and short-circuit current density on time with a temperature difference of 3.4°C .
- Figure 3-22. Temperature distribution comparison of calculated and measured temperatures at each interface in the thermocell.
- Figure 3-23. Photograph of the T-shirt embedded with the thermocell and capacitor, the latter for storing the power generated from the thermocell.
- Figure 3-24. Charge/discharge of a capacitor connected to the thermocell.
- Figure 3-25. Normalized maximum power output for various curvature radii.
Inset: photograph of a thermocell wrapped around a hot fluid pipe for energy harvesting.
- Figure 3-26. Circuit diagram depicting the lighting system for the LED, composed of thermocell, voltage converter and LED (the actual

red light of the LED is shown within the dark circle in the LED part).

Figure 4-1. Experimental setup for preparation of a planar-type CNT electrode. The inset shows a SEM image of a CNT sheet electrode.

Figure 4-2. Optical image of a furnace with halogen-lamp-heated quartz for thermal annealing.

Figure 4-3. a) Experimental setup of electrochemical flow cell for determination of mass transfer coefficient. b) Exploded view of the flow cell.

Figure 4-4. SEM images of a) CNT buckypaper and b) CNT aerogel sheet.

Figure 4-5. Optical image of assembled cylinder-type thermocell.

Figure 4-6. Characterization of mass transfer kinetics for CNT buckypaper and aerogel sheet. Polarization curves and dependence of limiting current on ferrocyanide concentration (inset) for a) the buckypaper and b) the aerogel sheet.

Figure 4-7. Illustrations and SEM micrographs (inset) providing comparison of the morphologies to ion transport (all scale bars are 300 nm long).

Figure 4-8. Raman spectrum for an as-drawn CNT sheet, showing I_D/I_G ratio of about 0.76.

Figure 4-9. The dependence of I_D/I_G ratio on oxidation temperature for a 5 minute anneal of CNT aerogel sheets in ambient air.

Figure 4-10. The dependence of the I_D/I_G ratio for CNT aerogel sheets on oxidation time in ambient air at 340°C.

Figure 4-11. HR-TEM images of a) as-drawn, b) 5 minute treated, and c) 15 minute treated CNT aerogel sheets (all scale bars are 5 nm long).

Figure 4-12. Cell voltage versus current density (top) and cell power density versus current density (bottom) for samples having different thermal oxidation times.

Figure 4-13. Maximum power density normalized to the inter-electrode temperature difference ($P_{MAX}/\Delta T^2$) as a function of thermal oxidation time.

Figure 4-14. The dependence of activation resistance and the sum of ohmic and mass transport resistance on thermal oxidation time.

Figure 4-15. Density change of the CNT electrode as a function of the mechanical compression (The inset illustrates the mechanical compression of a planar CNT electrode.).

Figure 4-16. $P_{MAX}/\Delta T^2$ generated by the thermocell as a function of the electrode density.

Figure 4-17. The dependence of mass transport and (inset) ohmic resistances on the electrode density.

Figure 4-18. Schematic illustration of the effect of mechanical compression on the structure and properties of the CNT aerogel network. The ohmic resistance decreases with increasing compression, but too high a compression decreases pore size, thereby restricting ion diffusion.

Figure 4-19. TEM image of CNTs uniformly decorated with Pt nanoparticles.

Figure 4-20. a) HR-TEM image of individual CNT decorated by Pt nanoparticles. b) Size distribution of Pt nanoparticles on CNTs.

Figure 4-21. Cyclic voltammograms obtained at a 100 mV/s scan rate using as-drawn, thermally oxidized, and thermally oxidized and Pt deposited CNT electrodes.

Figure 4-22. Electroactive surface area and redox potential difference for the above various CNT electrodes.

Figure 4-23. Nyquist impedance plots for various electrodes. The inset shows a close-up of the high frequency region of the curves.

Figure 4-24. Experimental setup for preparation of cylindrical CNT electrode.

Figure 4-25. Photograph and SEM image of the CNT electrode.

Figure 4-26. Optical images of a) cylindrical CNT electrode before (top) and after repeated compressions (bottom) in the compression jig (between which the cylindrical CNT sheet electrode was rotated about its long axis in the compression jig) and b) the two-part grooved template used as a compression jig for the compression of the cylindrical electrode.

Figure 4-27. Cell voltage and power density versus current density for variously treated cell electrodes.

Figure 4-28. Energy conversion efficiency relative to a Carnot cycle for various CNT electrodes in the cylindrical cell configuration. All sheet samples (except the as-drawn) were purified by thermal oxidation before assembly into cylindrical electrodes.

Chapter 1. Introduction

1.1 Motivation & research background

Power plants and various industrial processes produce large amount of by-product waste heat. This thermal energy is typically available at temperature below 130°C and can be converted into electricity at relatively low efficiencies [1-5]. More commonly, waste heat is released to the environment by means of cooling towers or by exchanging thermal energy with river or ocean water. Other examples of utilizing low-grade heat are geothermal energy and solar thermal systems [2,6,7].

An alternative conversion process utilizes an electrochemical pathway to provide thermogalvanic energy conversion [4,7-12]. A thermocell, also known as a thermogalvanic cell, is an electrochemical cell in which electrical energy is generated by the temperature difference between two half-cells. Using an aqueous electrolyte, a thermocell can operate at low temperature (below 130°C) to provide a voltage originating from the temperature dependent electrochemical redox potentials of hot and cold electrodes.

Numerous advances have been made in small-scale thermal energy harvesting using thermoelectric, metal/semiconductor thermocouples, ferromagnetic materials and Stirling engine technology, etc [5,13-15]. However, physical and material limitations and cost have prevented the wide application of current thermal energy harvesting technology [4,13].

Despite present low energy conversion efficiencies, thermocells have been the potential advantages of simple design, direct thermal-to-electric energy conversion, continuous operation, low expected maintenance, zero carbon emissions and low cost.

While semiconductor-based solid-state thermoelectrics can reach at least ~20% of Carnot efficiency, the power conversion efficiencies of thermocells are presently no higher than about ~2.63% of Carnot efficiency [16]. However, conventional solid-state thermoelectrics are expensive and inflexible, so they seem unsuitable for such applications as wrapping around a hot pipe that exits a chemical plant. In these applications, and many others where the thermal energy would otherwise be lost, the target is to maximize energy output as expressed as Wh/dollar, and in this regime the electrochemical thermal cells might have major advantages [17].

1.2 Thesis objectives

This thesis work aims to develop flexible thermocells with carbon nanotube (CNT) based flexible textile electrode and to improve power conversion efficiency of thermocells using CNT aerogel sheet and multiple optimization strategies.

The catalytic nature of CNTs could enhance the charge transfer kinetics for redox reaction. Consequently, investigations will be made into the feasibility of the CNTs as high performance electrode for thermocells with aqueous electrolyte. The use of porous and hierarchical structure of electrode may afford a larger electroactive surface area. As can be predicted

from the Tafel equations, a higher electroactive area would result in an increase in current generation.

The use of CNT textile electrode to attain the flexibility of thermocells will be considered. For the purpose, CNTs, particularly SWNT, are to be well dispersed in aqueous solution. Inspired by dyeing process, textile is dipped in the CNT colloidal solution and dried in oven. Consequently CNT-textile electrode will be simply obtained. With the flexible thermocells, waste thermal energy from arbitrary shaped heat sources including hot pipes or human body could be effectively harvested.

Structure and charge transfer kinetics of electrodes are an important aspect of thermocell power generation as it directly affects the power conversion efficiency. The use of aerogel structure of CNT sheet and adaption of diverse optimization approaches on the sheet electrode will be considered. The high surface area and ultra-low areal density of CNT aerogel sheet could facilitate ion transport within the electrode. In addition, Removal of undesirable impurities, optimal compression, and decoration of platinum nanoparticles will also be investigated to enhance thermocell efficiency.

Chapter 2. Thermocell and Carbon nanotubes

2.1 Thermocell fundamentals

2.1.1 Principle of operation

A thermocell is a non-isothermal electrochemical cell used to convert thermal energy directly into electricity. Figure 2-1 schematically illustrates a generic aqueous electrolyte thermocell, which utilizes temperature dependent redox couples. Two electrodes are presently placed at different temperature zones and the electrodes are in contact with electrolyte with or without a permeable membrane interposed in the electrolyte. The inter-electrode temperature difference generates an electrical potential difference because of the temperature dependence of electrode redox potential, even though the electrodes may be identical and immersed in the same solution. When the cell is connected to an external electrical load, the thermally generated potential drives electrons in the external circuit and power can be delivered. Continuous operation of the thermocell requires diffusion of the reaction product formed at one electrode to the other electrode, where it can then become a reactant.

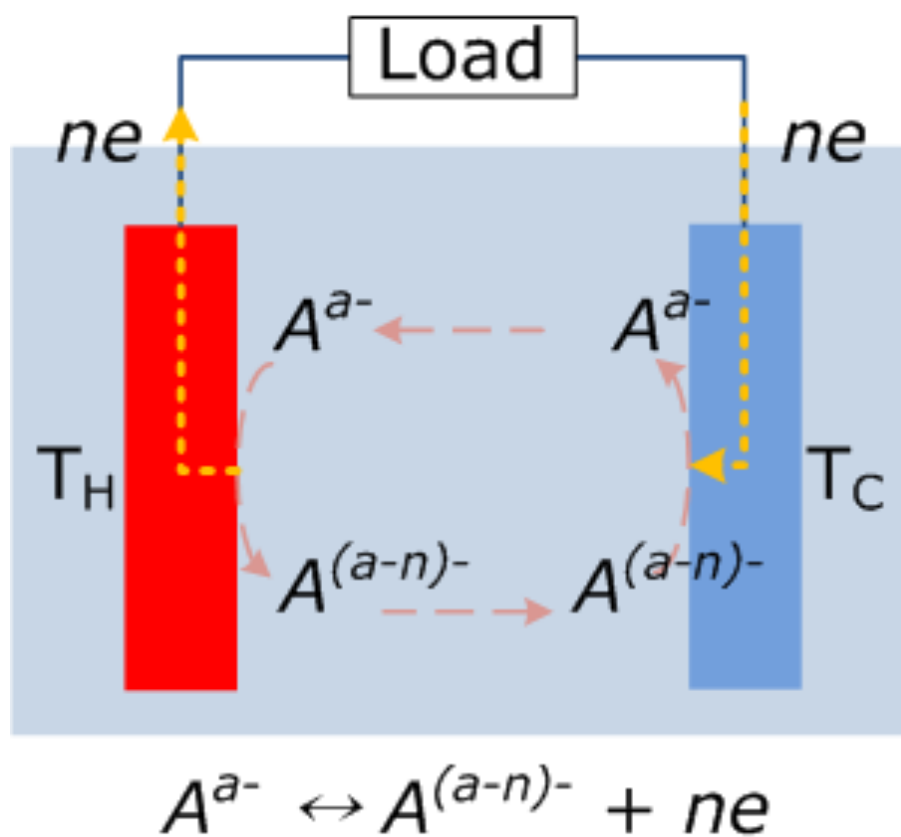


Figure 2-1. Illustration of a thermocell operation of an aqueous electrolyte during power generation.

2.1.2 Open-circuit potential

The thermoelectric potential in a thermocell is generated by the temperature dependence of the free energy difference between reactant and product of a reaction taking place at the electrolyte-electrode interface. The origin of this potential is analogous to that of potentials produced by thermocouples. A minor effect arises from the thermal diffusion potential, which is due to ion migration driven by the temperature difference in the electrolyte (Soret effect) [8,18,19]. However, for most systems of interest, the electrode potentials dominate and the thermal diffusion potential can be neglected for practical purposes, since it is about three orders of magnitude lower than the electrode potential, making only negligible contribution to the total electromotive force (EMF) [20,21].

Strictly speaking, processes occurring during thermocell power production are not thermodynamically reversible. Therefore, they have been used to develop the theory of thermodynamics of irreversible processes [20-23]. The early literature on thermogalvanic cells is mainly concerned with the dependence of open-circuit potential difference on the temperature difference between the electrodes [21,22,24]. In particular, the presented theory calculates the thermoelectric coefficient $\partial E/\partial T$, which represents the temperature dependence of the open-circuit potential produced by the cell. If the redox reaction for a hypothetical redox system ($A + ne \leftrightarrow B$) in the thermocell is given, then the thermoelectric coefficient can be expressed as:

$$nF(\partial E/\partial T)_{t=\infty} = (S_B + \hat{S}_B) - (S_A + \hat{S}_A) - n\bar{S}_e \cong S_B - S_A \quad (1.1)$$

where n is the number of electrons involved in the above hypothetical redox reaction. F is faraday constant, the symbols S_A and S_B are the partial molar entropies of species A and B, and their respective Eastman entropies are denoted by \hat{S}_A and \hat{S}_B , accordingly [18,19]. The Eastman entropy of transport arises from the interaction of an ion and its hydration shell with the solution. Thus, when an ion is transported from one half cell to another in a thermocell system (or is destroyed in one and formed in the other), it carries both its partial molar entropy and the Eastman entropy of transport into the half cell. The sum of these two contributions is often designated as the total transported entropy, which is thus given by $\bar{S}_i = S_i + \hat{S}_i$. The quantity \bar{S}_i is the transported entropy of the electrons in the metallic electrodes and the leads which are maintained at different temperature. This term usually makes only a negligible contribution to $(\partial E/\partial T)_{t=\infty}$, and is typically only 1% of thermocell potential [20,21]. It should be noted that the subscript ∞ , in eq. 1.1 implies that sufficient time has been allowed for the system to reach a steady state. Initially, the thermoelectric coefficient is a little above the long-term steady-state value. The fall of the initial value is attributed to the Soret effect, which arises because the molecules around the hot electrode diffuse more readily than those around the cold electrode, thus the initially homogeneous solution slowly develops a concentration gradient between the hot electrode and the cold electrode. The concentration gradient may take even days for the final steady value of $\partial E/\partial T$ to be achieved because the Soret effect is quite small [10]. Moreover, the transported entropy of the electrons is also negligible. Therefore it is common to use the

initial temperature dependence, which corresponds to deletion of the Eastman entropies of transport and transported entropy of the electrons in eq. 1.1.

However, the above thermodynamic results for thermocells can only be applied to open-circuit potential conditions. They are not able to predict the discharge behavior when a net current is flowing through a cell as electric power is produced [22]. The power output from thermocells depends not only on $\partial E/\partial T$ but also on the current delivery characteristics of the cell. Experimental measurements may be the only reliable way to determine power generation rates and efficiency of a thermocell. Hence, many observations (such as the time and the output current dependence of the cell potential) can be explained only by incorporating measured electrochemical kinetic parameters into the theoretical analysis.

2.1.3 Figure of merit and power conversion efficiency

The efficiency parameter commonly used to describe thermoelectric performance is the figure of merit, Z , which is defined as [25]:

$$Z = (\partial E/\partial T)^2 \cdot \sigma/\kappa \quad (1.2)$$

where $\partial E/\partial T$ (the thermoelectric coefficient) is the temperature dependence of the inter-electrode potential difference, σ is the electrical conductivity and κ is the thermal conductivity of the electrolyte. Thus the ratio σ/κ shows the relative influence of electrical and thermal conductivities on

thermocell operation. Electrical conductivity is mainly attributed to ionic conduction through the electrolyte materials between hot and cold electrodes. Electrolyte thermal conductivity is due to conduction and convection of heat through the redox couple and background solution.

The power conversion efficiency (PCE), Φ , of a thermocell is defined as the ratio of electrical power output (P) from the cell to thermal power flowing ($\partial Q/\partial t$) through the cell:

$$\eta = P/[k \cdot A(\partial T/\partial x) + I \cdot \Delta T \cdot \Delta S/(nF)] \cong P_{\max}/k \cdot A(\partial T/\partial x) \quad (1.3)$$

The first term in the denominator, $k \cdot A(\partial T/\partial x)$, is the rate of heat flow from the hot electrode to the cold electrode and the second term, $I \cdot \Delta T \cdot \Delta S/(nF)$, is the reversible heat of the cell reaction. The symbol, k , represents the thermal conductivity of the electrolyte, $\partial T/\partial x$ is the temperature gradient between the cell electrodes, and A is the cross-sectional area of the thermocell. The quantities I and ΔT are the current and the absolute temperature differences, respectively. The entropy change for the cell reaction is denoted by ΔS and n is the number of electrons transferred in the cell reaction. Note that inclusion of the reversible heat of reaction, i.e., $I \cdot \Delta T \cdot \Delta S/(nF)$, in eq. 1.3 is appropriate only in a thermocell system which involves net consumption of electrolyte. Hence, this term can be eliminated for a thermocell that operates to provide continuous conversion of thermal energy to electricity.

The electrical output power in eq. 1.3 is commonly expressed as the maximum value, P_{\max} , which occurs when the external load resistance is set

equal to the internal resistance of the cell. P_{\max} in eq. 1.3 can be obtained from experimental characteristic curves of potential difference, E , versus current, I . In the simplest case, in which such $E-I$ curves are linear, it is easy to show that P_{\max} is given by the rectangle of greatest area under the $E-I$ curve. Hence, $P_{\max} = 0.25E_{OC}I_{SC}$, where E_{OC} is the open-circuit potential difference and I_{SC} is the short-circuit current delivered by the thermocell. When the $E-I$ characteristic curves are non-linear, P_{\max} can conveniently be determined from the maximum of a graph of I^2R against R , where R is a variable load resistance.

Finally, the most useful parameter for describing the efficiency of power conversion devices is η_r (η/η_c), the power conversion efficiency relative to that of a Carnot cycle. The maximum efficiency for the conversion of heat energy to electrical energy is given by the Carnot expression, $\eta_c = (T_1 - T_2)/T_2$, where T_1 and T_2 are the lower and higher absolute temperatures of the respective electrodes.

2.2 Carbon nanotubes

Since their discovery in 1991 by Iijima [26], carbon nanotubes (CNTs) have been of great interest, both from a fundamental point of view and future oriented applications. Their large length (up to several microns) and small diameter (a few nanometers) result in a large aspect ratio. The most important feature of these structures is their electronic, mechanical, optical and chemical characteristics (Table 1). Various experiments, which were carried out transmission electron microscopy (TEM), scanning tunneling

microscopy (STM), resistivity and Raman spectroscopy, are consistent with identifying the CNTs with cylindrical graphene sheets of sp^2 -bonded carbon atoms.

Different types of CNTs can be produced in various ways. The most common techniques are discharge, laser ablation, chemical vapor deposition. These raw carbon nanotubes are difficult to be adapted to various applications because of lower yield production and strong interaction of van der Waals force and hydrophobic nature. Therefore, large-scale production and purification are necessary for future applications to be realized.

Table 1. Physical properties of CNT and their applications.

| Properties | | Characteristics | Applications |
|-----------------------|-----------------------|--|------------------------------------|
| Electrical properties | Conductivity | Metal/Semiconductor | Bio/chemical sensor |
| | Resistivity | $\sim 10^{-9} \Omega \cdot \text{cm}$ | |
| | Max. current density | $\sim 10^{19} \text{ A/cm}^2$ | Nanoelectronics |
| Mechanical properties | Elastic modulus | $\sim 1 \text{ TPa}$ | Nanocomposite |
| | Max. tensile strength | $\sim 30 \text{ GPa}$ | |
| | Thermal conductivity | $\sim 1800\text{-}6000 \text{ W/m}\cdot\text{K}$ | |
| Geometric properties | Aspect ratio | $> 10,000$ | Field emission |
| | Surface area | $100\text{-}700 \text{ m}^2/\text{g}$ | Super-capacitor Hydrogen sensor |

2.2.1 Geometric structure of CNT

Ideally, a carbon nanotube consist of one carbon single-walled nanotube (SWNT) or more carbon multi-walled nanotube (MWNT) seamless cylindrical shells of graphite. Each shell is made of sp^2 carbon atoms that form a hexagonal network without any edges. The MWNT of interlayer spacing is about 0.34 nm. The CNTs are typically longer than a micrometer, with diameters ranging from less than 1 nm to several dozen nanometers. Most frequently, the diameter of carbon nanotubes varies roughly between 0.4 nm and 3 nm for SWNTs and from 1.4 nm to 100 nm for MWNTs [27]. As a result of these dimensions and this aspect ratio, CNTs are expected to have some features of low-dimensional materials.

CNTs can be distinguished into SWNT, which a cylinder with inly one external wall; MWNTs, which are made of multiple coaxial cylinders. To define a SWNT in terms of its geometry structure formation, it is easy to approach from the original structure of the graphene. Figure 2-2 represents a schematic diagram of graphene and vectors to define the CNT structure. The chiral vector (C_h) connecting the points which map onto each other when the unrolled sheet is rolled up to form a nanotube, which can be expressed as

$$C_h = na + mb \equiv (n, m) \quad (1.4)$$

where a and b are the unit vectors and integers (n, m) . The vector $(n, 0)$ denote zigzag type and the vectors (n, n) denote armchair type, and the larger

the value of n , the larger the diameter of a rolled up nanotube. The chiral angle θ of the nanotube with respect to the zigzag direction ($\theta = 0^\circ$) and the unit vectors a and b of the hexagonal honeycomb lattice. The armchair tube corresponds to $\theta = 30^\circ$ on this direction. All the armchair tubes show metallic behavior and others show either semiconducting or metallic depending on their (n,m) configuration. In general, metallic tubes are formed only if $n - m = 3p$, where p is an integer, otherwise semiconducting. Thus, in principle, one can expect a third of bulk SWNT materials are metallic and two thirds are semiconducting. In terms of the integers (n,m) , the rolled-up tube diameter

$$d_t = C_{hl}/\pi = a_0\sqrt{3(n^2 + nm + m^2)}/\pi \quad (1.5)$$

where a_0 is the nearest-neighbor C-C distance, i.e., is 1.42 Å in graphite, C_{hl} is the length of the chiral vector C_h , and the chiral angle θ is given by

$$\theta = \tan^{-1}[\sqrt{3}m/(m + 2n)] \quad (1.6)$$

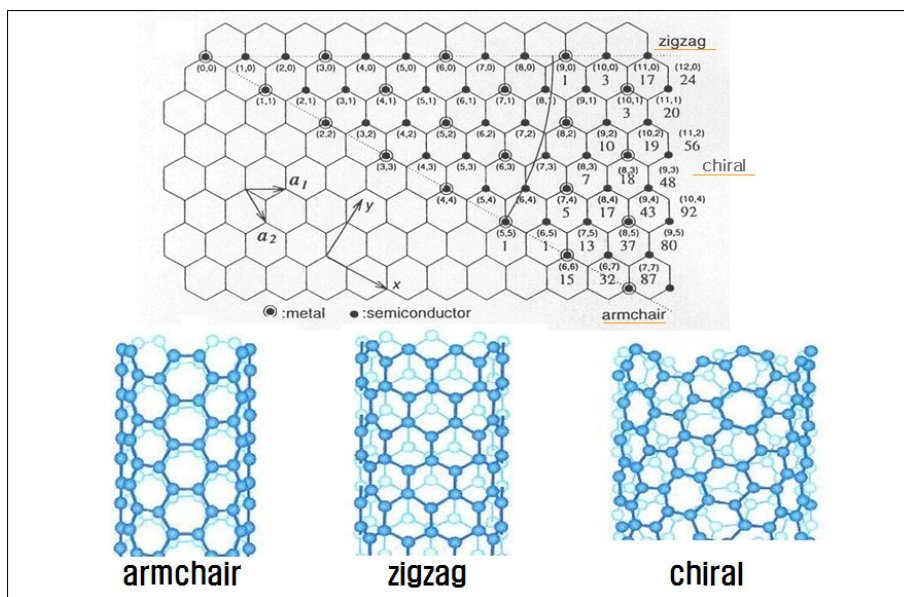


Figure 2-2. Classification and structure of CNTs.

2.2.2 Synthesis and purification of pristine CNT

SWNT and MWNT are usually produced by arc-discharge [28], laser ablation [29], chemical vapor deposition [30], or gas-phase catalytic process (HiPco) methods [31]. The abovementioned methods are impossible to avoid impurities, consist of carbon-coated metal catalysts and carbon nanoparticles or amorphous carbon. In addition, structural defects, such as dangling bond, are often found in most type of carbon nanotubes. The main techniques applied for purification of CNTs are oxidation of contaminants [32,33], flocculation and selective sedimentation [34], filtration [35], size-exclusion chromatography [36], selective interaction with organic polymers [37,38], or microwave irradiation [39,40].

2.2.3 Raman spectroscopy for CNT characterization

Raman spectroscopy has been widely utilized for characterization of CNTs with respect to their diameter (i.e., the assignment of the chirality of SWNT) and electronic structure, as well as purity [41]. When incident light interact with a CNT, photons are scattered with a certain frequency. Most of the electrons, which are excited come back to the initial energy level, emitting light with the same frequency as the incident light, which is called Rayleigh scattering. A very small of photons is scattered showing a frequency shift from the incident light, resulting the relative vibrational energy level of atomic structure of CNT. This is so-called Raman scattering.

The Raman spectra present different features being all sensitive to the chirality, such as the radial breathing mode (RBM), where all the carbon atoms are moving in-phase in the radial direction, the G-band where neighboring atoms are moving in opposite directions along the surface of the tube as in 2D graphite, the dispersive disorder induced D-band. The RBM frequency is reciprocally dependent on the tube diameter d_t as $\omega_{RBM} = 248/d_t$ [42].

The G-band is thus an intrinsic feature of CNTs that is closely related to vibrations in all sp^2 carbon materials. The most important aspect of the G-band is the characteristic Raman lineshape which differs in accordance with whether the nanotube is semiconducting or metallic, allowing to readily distinguishing between both types. This band shows two different components, the lower frequency component associated with vibrations along the circumferential direction, (G^-), and the higher frequency component, (G^+), attributed to vibrations along G the direction of the nanotube axis. Precious studies show that the first component is dependent of diameter of CNT while the second, the higher frequency component, doesn't present this dependence, which differs according to metallic or semiconducting nanotubes. The D-band in graphite involves scattering from a defect, which breaks the basic symmetry of the graphene sheet, it is observed in sp^3 carbons containing porous, impurities or other symmetry-breaking defects. On the other hand, the second-order 2D-band doesn't require an elastic defect-related scattering process, and is observable for defect-free sp^2 carbons.

Carbon multi-walled nanotubes (MWNTs) are made of concentric graphene sheets rolled in a cylindrical form with diameters of tens of nanometers [43] and because of this large diameter of the outer tubes for typical MWNT and because they contain an ensemble of CNTs with diameters ranging from small to very large, most of the characteristic differences that distinguish the Raman spectra in SWNT from the spectra for graphite are not so evident in MWNT. For example, the RBM feature associated with a small diameter inner tube can sometimes be observed when a good resonance condition is established, but this is not the usual result, since the RBM signal from large diameter tubes is usually too weak to be observable and the ensemble average of inner tube diameter broadens the signal [44].

Whereas the G^+ - G^- splitting is large for small diameter SWNT tubes, the corresponding splitting of the G band in MWNT is both small in intensity and seared out due to the effect of the diameter distribution within the individual MWNT, and because of the variation between different tubes in an ensemble of MWNT in typical experimental samples. Therefore the G-band feature predominantly exhibits a weakly asymmetric characteristic lineshape, with a peak appearing close to the graphite frequency. The most effective radiation influence is expected in the case of the electron irradiation of MWNT. This is explained by the possibility not only that radiation defects occur during irradiation, which will contribute to the degradation of nanotubes, but also that seems appear due to the broken connections as vacancies are generated [45].

Chapter 3. Flexible Thermocell Film

3.1 Introduction

The human body consistently maintains its temperature at 36°C for its whole life and simultaneously releases thermal energy of about 100 watts to the surroundings [46]. Based on Carnot efficiency, a maximum power of about 5 watts [47] –which is equivalent to the power needed to operate a portable smart electronic device- is available from the released body heat [48]. Recently, low power technology has become more feasible, due to the progressive advances in electronic devices, so that the energy scavenged from body heat is expected to either replace or augment battery usage [49,50].

Thermoelectric generators are envisioned as a host for harvesting low-grade thermal energy. In the past decades, numerous advances have been made in thermoelectric devices [49,51-55], the basic unit of which typically consists of n-type and p-type semiconductors. However, the relatively small thermoelectric coefficient (~tens of microvolts per Kelvin) is the main obstacle to harvesting of thermal energy, which is typically available at temperatures below 130°C [56]. Moreover, there still remain obstacles such as rare and fragile thermoelectric materials and complicated fabrication processes being required [13,57].

3.2 Chapter aims

In this chapter, an efficient method that converts low-grade waste thermal energy such as heat released from the human body into electricity is presented using an all-carbon electrode with hierarchical porosity that is designed for a thermal electrochemical cell. The thermocell presented here utilizes the temperature dependence of the ferricyanide/ferrocyanide redox couples and employs the flexibility of an activated carbon textile electrode that is coated with carbon nanotubes (CNTs). With these components, the thermocell is flexible enough to wear on clothes and to wrap around cylindrical shape such as pipes. The wearability for harnessing human body heat is demonstrated by means of a plastic thermocell connected to a capacitor that is embedded into a T-shirt, which is in turn worn by a person. Practical use of thermocell is demonstrated with a serial thermocell array that can power a typical commercial light emitting diode (LED).

3.3 Experimental setup

3.3.1 Preparation of CNT-textile electrodes

In order to obtain activated carbon textile (ACT, CH15, Kuraray Chemical, Japan) coated with CNTs, it is necessary to prepare a well dispersed colloidal solution of CNTs. Commercially available purified carbon single-walled nanotube (SWNT, ASP-100F produced by Il-jin Nanotech) and

dodecylbenzenesulfonate (SDBS, Sigma-Aldrich) as an anionic surfactant to make the SWNT colloidal solution were used. SWNTs were added to 57 mM SDBS aqueous solution at a concentration of 2 mg/mL followed by dispersal using ultrasonication for 12 h. C-ACT was obtained by simple dipping and drying process, as shown Figure 3-1. When pristine ACT was dipped into the colloidal solution, the ACT quickly swelled with a large amount of the solution due to its highly porous structure. The C-ACT was subsequently rinsed with deionized water several times to remove redundant SDBS, and then dried in an oven.

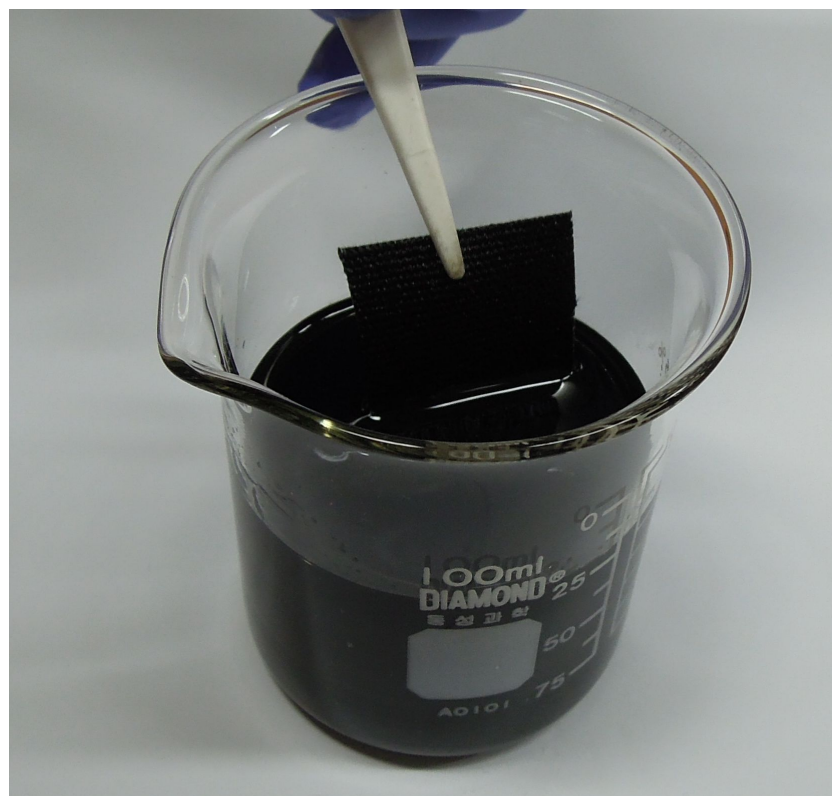


Figure 3-1. Optical photograph of dipping process for CNT coating on ACT.

3.3.2 Fabrication of plastic thermocells

To fabricate a thermocell that is pliable enough to accommodate any shape of heat source including a body or curved shape, a plastic thermocell that consists of all flexible materials such as polyethylene terephthalate (PET), fabrics and wires (Figure 3-2). For the half-cell, collecting wire, and CNT coated ACT were stacked in order. Then, separator and adhesive tape were placed between two half-cells. The thermocell structure was completed by one-step hot press at 120°C for 20 s. Figure 3-3 shows optical photograph of assembled plastic thermocell. The fabricated thermocell is 600 μm thick and has a highly flexible nature.

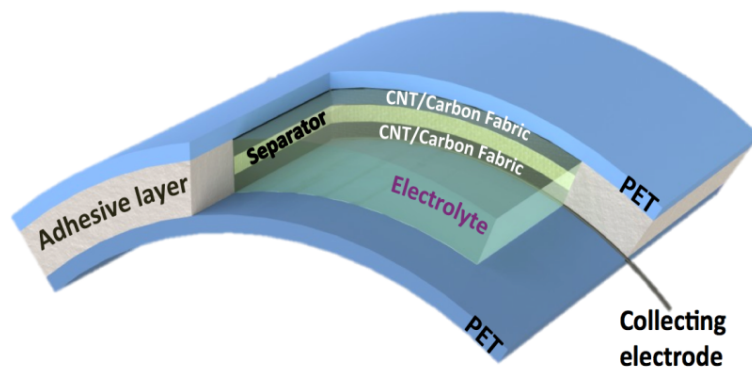


Figure 3-2. Schematic depicting the structure of the flexible thermocell.

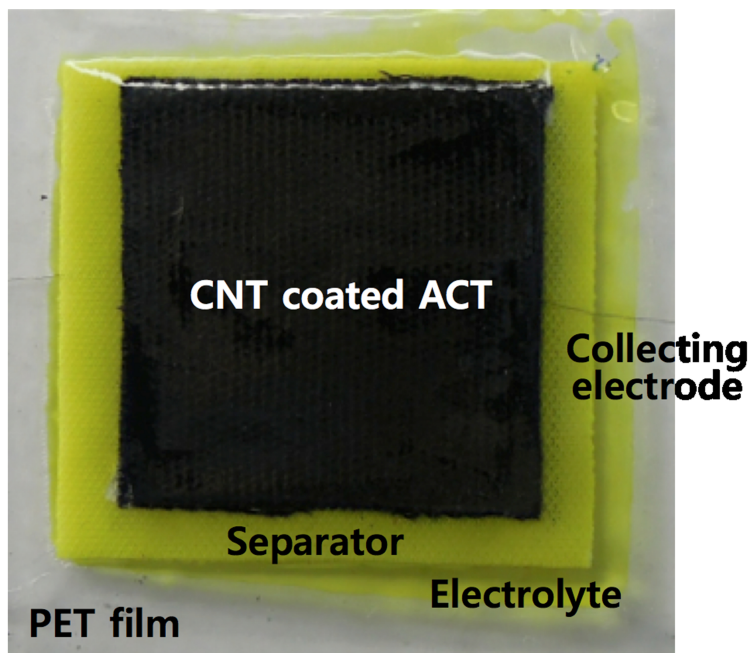


Figure 3-3. Photograph of the fabricated plastic thermocell.

3.3.3 Thermocell testing and characterization

Hot and cold temperatures were controlled by circulating water from a thermostatic bath with an accuracy of $\pm 0.1^{\circ}\text{C}$. The potential and current output from the cell were measured using a voltage-current meter (Keithley, 2000 Multimeter) for characterizing power output with respect to external resistive loads. Sheet resistance of the samples was simply measured by a four-point probe instrument (Changmin Tech, CMT-SR2000N). Electrochemical impedance measurements were conducted using a commercial instrument (Zahner, IM6ex). N_2 absorption isotherms (at 77K) up to 1 bar were measured using a Micromeritics ASAP 2020 static volumetric gas adsorption instrument. Prior to the sorption analysis, samples in the analysis chamber were subject to a vacuum of 10^{-5} Torr at 150°C for 12 hours to remove the impurities. The cyclic voltammetry (Eco Chemie, PGSTAT30) analysis was carried out using ACT and C-ACT as a working electrode in 10 mM $\text{K}_4\text{Fe}(\text{CN})_6$ solution with a scan rate of 5 mV/s. Platinum (Pt) and saturated calomel electrodes were used as counter and reference electrodes, respectively.

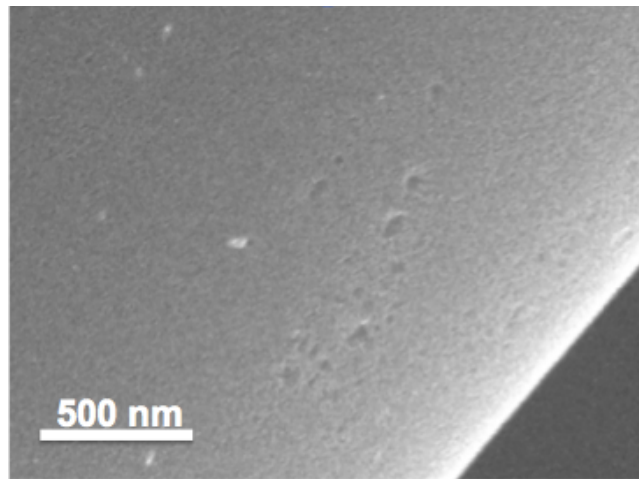
3.4 Results and discussion

3.4.1 Material characteristics

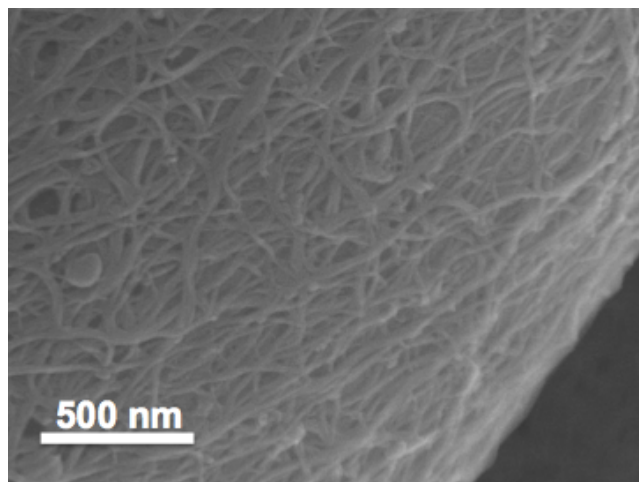
Inspired by the solution-based CNT coating method [58], the CNT-coated textile sheet was simply prepared by dipping ACT into a colloidal solution of CNTs, followed by drying in oven. The fabrication process is similar to that widely used dyeing fibers and fabrics in the textile industry. It was observed that the CNT solution instantly soaked into the textile and the CNT networks formed conformally on the surface of the individual textile fibers, as shown in Figure 3-4a and b.

Figure 3-5 shows the nitrogen adsorption isotherms of the ACT and CNT coated ACT samples. The ACT appeared to be a microporous material, based on the observation of a typical Type I isotherm with an initial sharp increase at relatively low pressures ($P/P_0 < 0.1$). In contrast, the CNT coated ACT exhibited combined characteristics of type I/II materials, with slight increases at both low and high pressures and a moderate slope at intermediate pressures. These properties indicated hierarchical porous characteristics typical of the presence of both micropores and mesopores. Analyses of the pore size distributions of ACT- and C-ACT electrodes were performed using Brunauer-Emmett-Teller (BET) method. BET surface area ($1726 \text{ m}^2/\text{g}$) of pristine ACT is decreased to $1180 \text{ m}^2/\text{g}$ after CNT coating. However, it is noteworthy from Figure 3-6 that the cumulative pore volume of C-ACT increases with increasing pore size from micropores to mesopores in contrast to the ACT, which shows a cumulative volume

saturated at micropores. Due to the highly flexible feature of the C-ACT, there are no significant change in resistance with the bending curvature, as shown in Figure 3-7.



(a)



(b)

Figure 3-4. SEM images of the a) pristine and b) CNT coated activation textile.

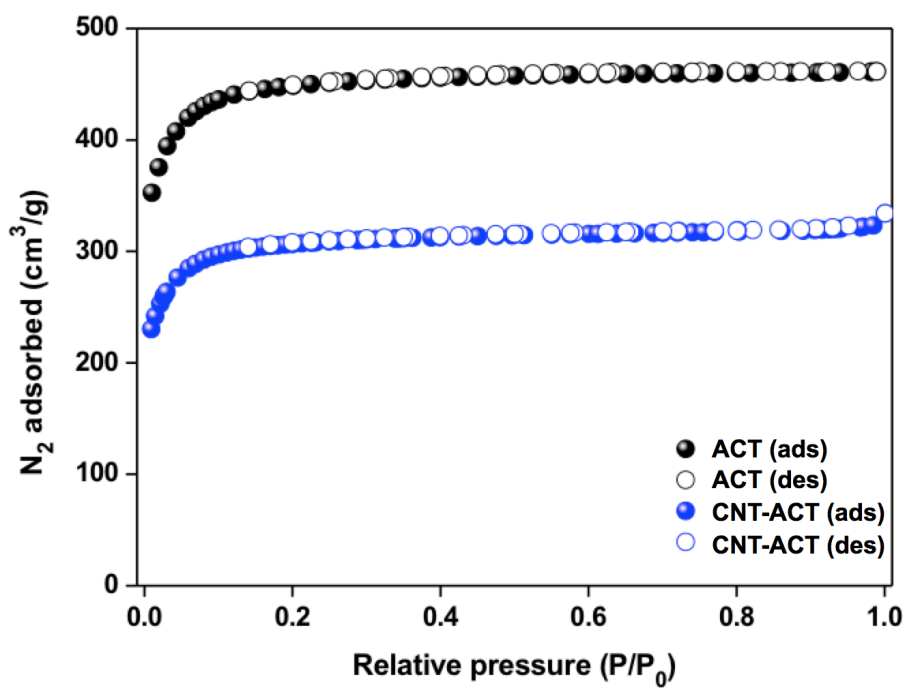


Figure 3-5. Nitrogen adsorption isotherms at 77 K for ACT and CNT-ACT samples.

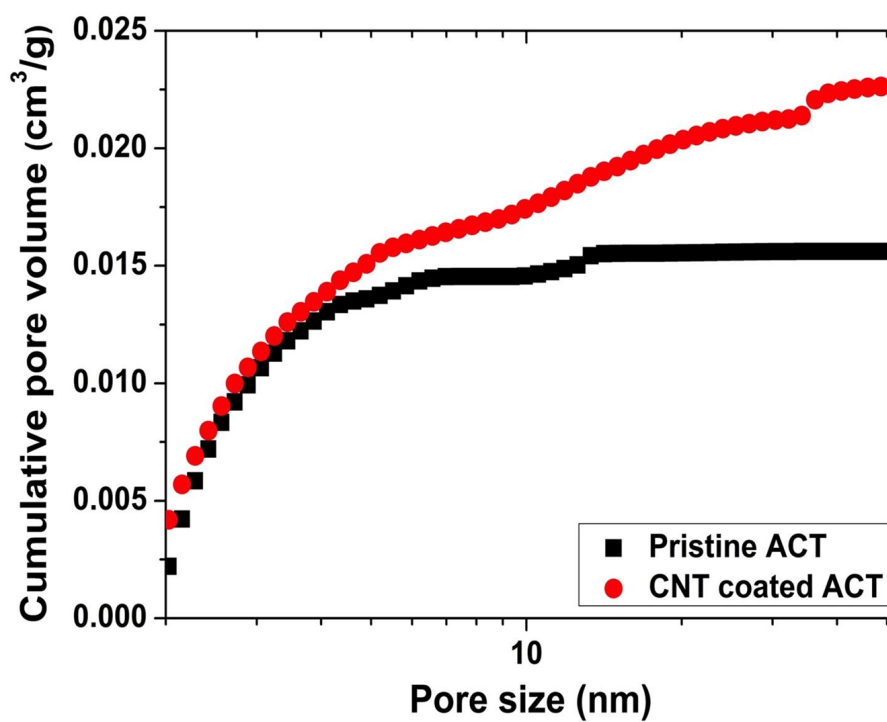


Figure 3-6. The cumulative pore volume in the mesopore range derived non-local density functional theory (NLDFT).

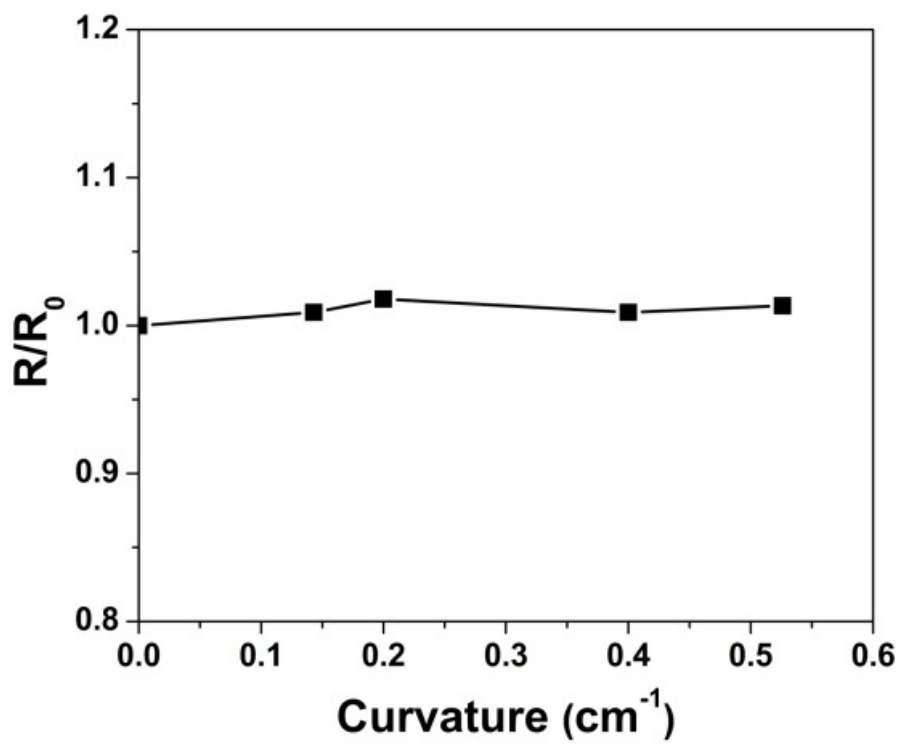


Figure 3-7. Resistance stability test for different bending curvatures.

A 0.4 M ferricyanide/ferrocyanide redox couple, the concentration of which is close to saturation, was used as an aqueous electrolyte. The thermoelectric coefficient of the redox couple was obtained by measuring the temperature dependence of the potential difference over a temperature range from 0 to 15°C, as shown in Figure 3-8. The thermoelectric coefficient ($\sim 1.4\text{mV/K}$) is in good agreement with previous reports (1.4 to 1.5 mV/K) [11,20]. Compared with other redox couples such as Cu^{2+}/Cu , Fe^{2+}/Fe and $\text{Np}^{4+}/\text{Np}^{3+}$, the ferricyanide/ferrocyanide electrolyte is better suited for harvesting low-grade thermal energy by virtue of its relatively higher thermoelectric power and larger exchange current density [9,59].

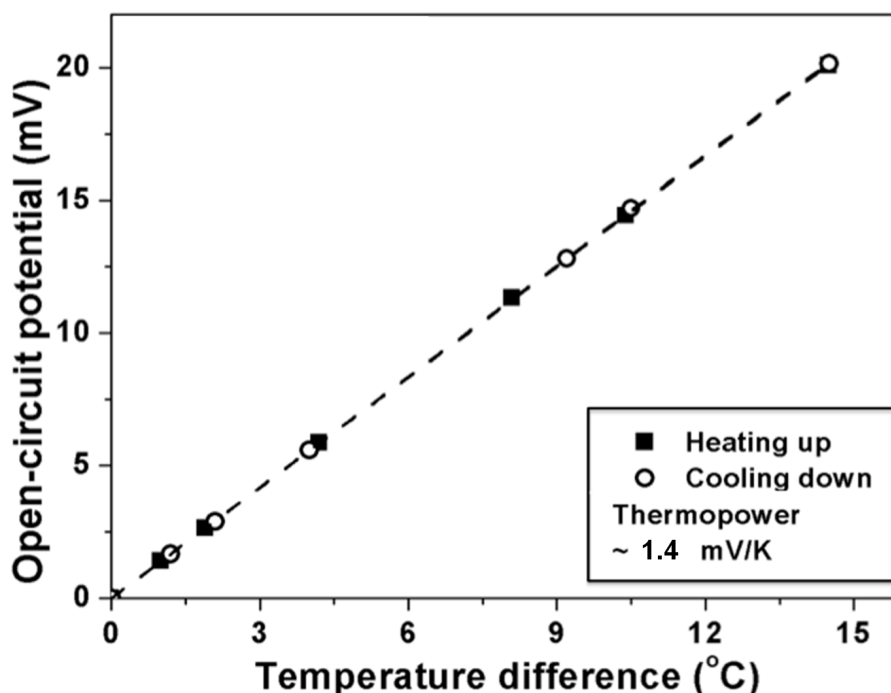


Figure 3-8. Dependence of open-circuit potential on the temperature difference between hot and cold electrodes.

3.4.2 Enhanced electrode performance with CNT

For the choice of electrode material, charge transfer reaction and activation barrier at the electrode/electrolyte interface have to be considered because they are the two most important factors that determine the electrochemical performance. The electrode performance is generally related to surface area and catalytic behavior of electrodes [60,61]. Activated carbon textiles having a high specific surface area are good candidates for electrode materials [62-64]. Moreover, carbon nanotubes have been widely employed in electrochemical applications due to fast carrier transportation, superior chemical stability and excellent catalytic activity [65-67]. Therefore, the performance of the device is expected to be enhanced by incorporating CNTs into the ACT electrode sheet. In addition, the flexible feature of the textile allows fabrication of a pliable thermocell that is compatible with curved heat sources.

The performance of the thermocell with ACT is compared to that with a C-ACT electrode. As shown in Figure 3-9, the C-ACT electrode yielded a current density (j_{SC}) of 189.25 mA/m² and a power density (P_{MAX}) of 90.38 μ W/m², corresponding to a normalized current density ($j_{SC}/\Delta T$) of 139.15 mA/m²K and a normalized specific power density ($P_{MAX}/\Delta T^2$) of 48.86 μ W/m²K² values, which are much higher than the corresponding ones for the thermocell with pristine ACT (62.32 mA/m²K and 21.9 μ W/m²K², respectively). The enhanced performance of the C-ACT electrode can be explained by the reduction of three primary internal resistances (Figure 3-10), i.e., activation, ohmic and mass transport resistances.

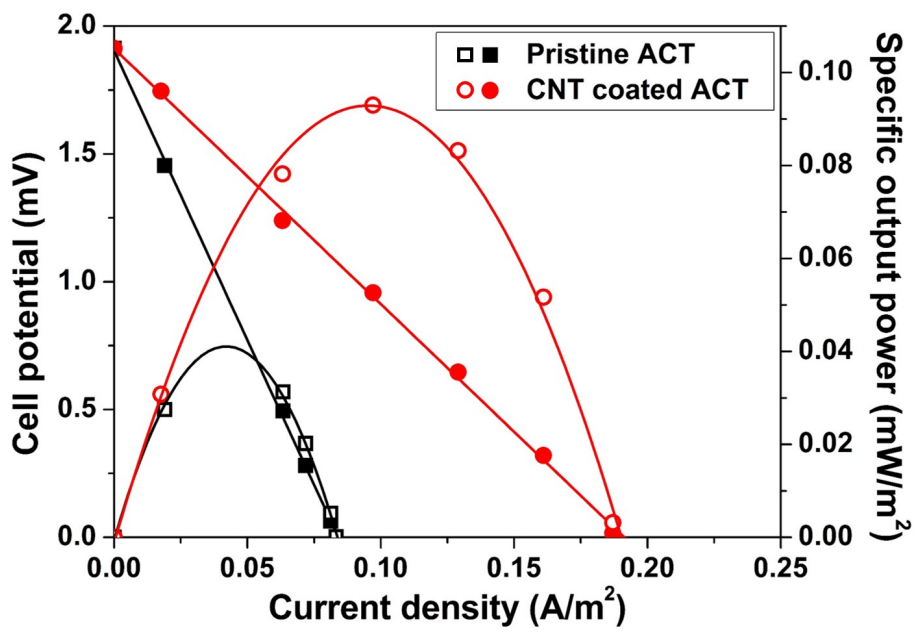


Figure 3-9. Thermocell discharge and specific output power as a function of the current density of pristine the ACT and C-ACT electrodes.

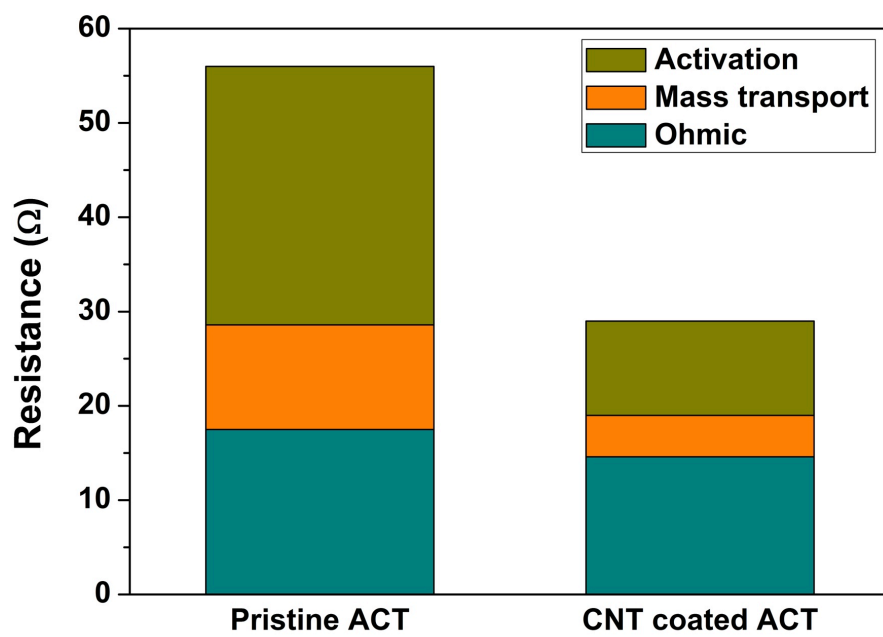


Figure 3-10. Comparison of three internal resistances of the thermocell with pristine ACT and CNT coated ACT electrodes.

It is well known that CNTs have fast electron transfer characteristics due to their high local density of states and quasi-reversible redox process [58,68]. Therefore, coating CNT on an ACT electrode might reduce the activation barrier in thermocell reaction [61]. Cyclic voltammetry (CV) measurements were carried out to compare reaction characteristics of ACT and C-ACT electrodes. Due to the decrease in the BET surface area, the peak current is slightly reduced when CNT network is formed on the ACT fibers. However, It is clearly observed from Figure 3-11 that the redox potential difference decreased from 239 to 135 mV after incorporating CNTs. Furthermore, as shown in Figure 3-12, the diameter of the semi-circle on the complex plane in the Nyquist plot was smaller for the C-ACT electrode compared to the ACT electrode. Note that the diameter of the semi-circle represents the kinetic resistance (R_{ct}) of the Faradaic reaction based on the Randle's equivalent circuit model [69,70] shown in the inset of Figure 3-12. These measurements indicate that the CNT coated on activation barrier in thermocell reactions. Because of the improved reaction characteristics, the activation resistance was significantly reduced by 63% (from 27.4 to 10 Ω) as shown in Figure 3-10.

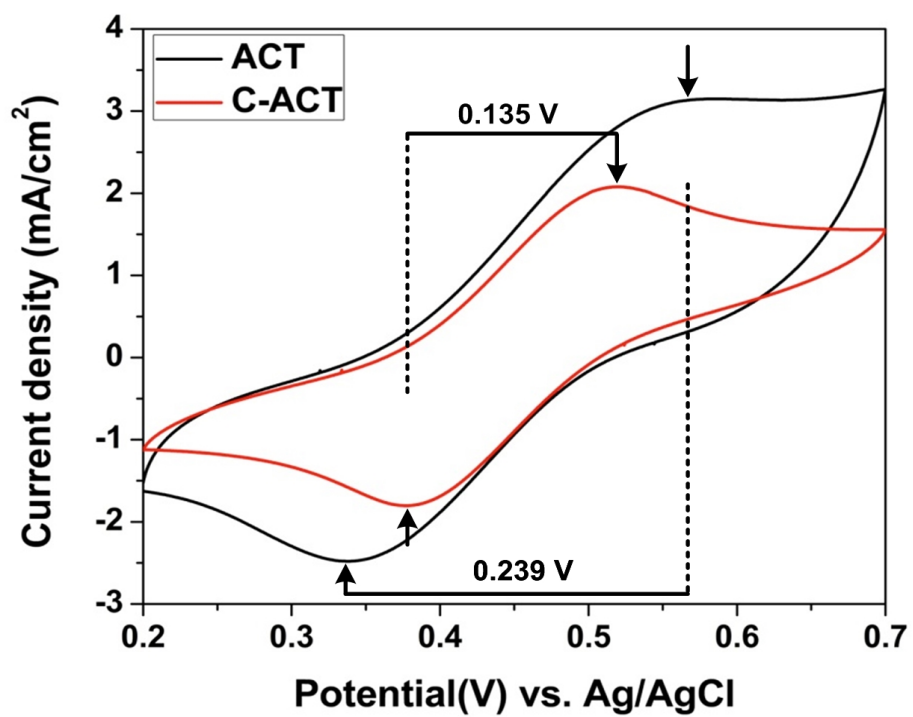


Figure 3-11. Cyclic voltammograms of pristine and CNT coated ACT sheet.

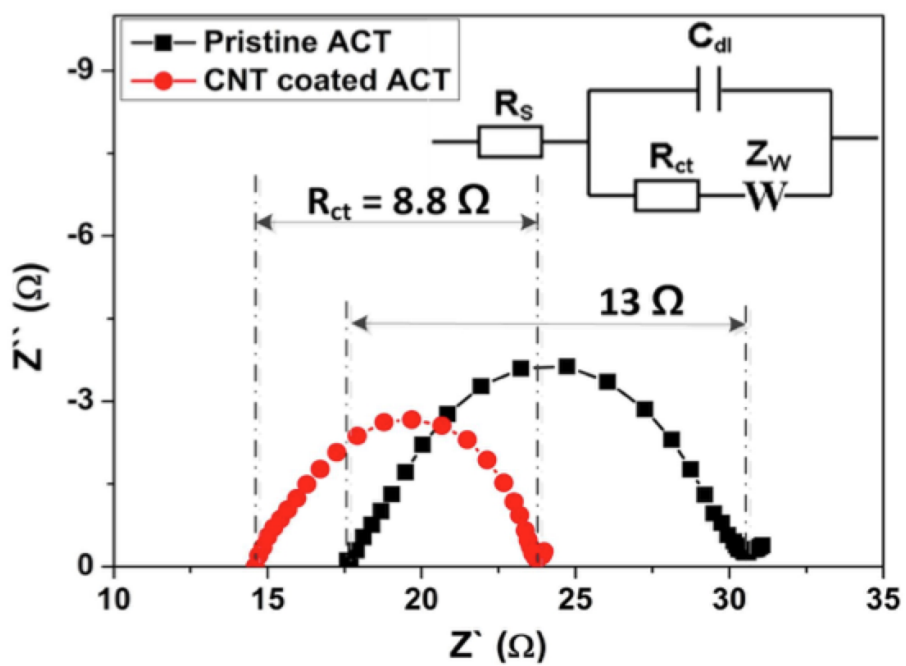


Figure 3-12. Nyquist impedance plots for ACT and C-ACT electrodes. Inset shows the Randle's equivalent circuit.

Ohmic resistance in a thermocell is caused by equivalent series resistance (ESR), typically composed of electrode and electrolyte resistances. While changes in electrical resistance of electrolyte are negligible because both thermocells have same inter-electrode spacing and electrolyte concentration, the CNT coated on ACT leads to almost a fivefold decrease in the sheet resistance of ACT (from 14 to 3 $\Omega/\text{sq.}$) as shown in Figure 3-13. From the analysis of electrochemical impedance spectroscopy (EIS) measurements, it is confirmed that the ESR decreased from 17.5 to 14.6 Ω when the C-ACT is utilized (Figure 3-11).

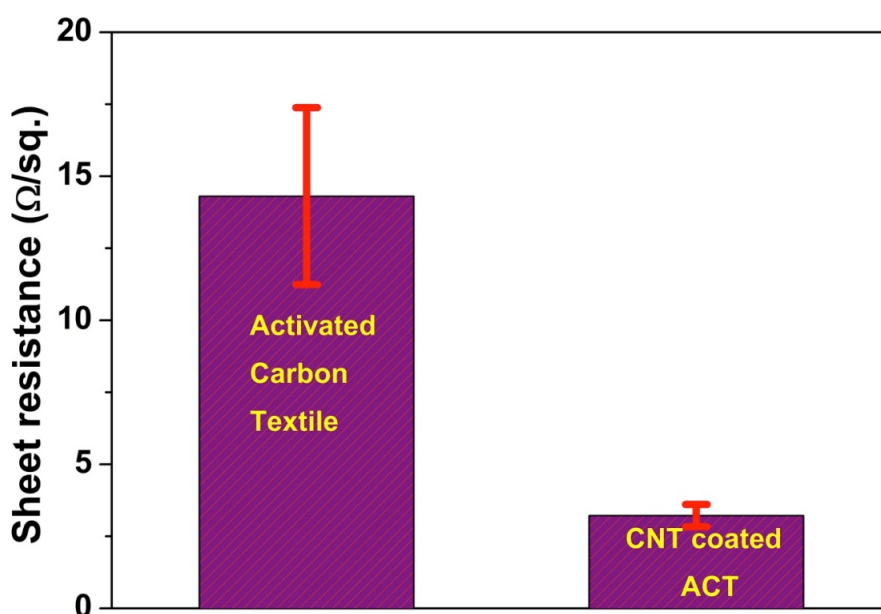


Figure 3-13. Sheet resistance of the two textile electrodes.

A mass transport process is needed to transfer the reaction product formed at one electrode to the other electrode for continuous operation in a thermocell [17]. In general, diffusion processes due to both thermal (Soret diffusion) and concentration (Fickian diffusion) gradients, and convective process due to density gradients [18,19,21,71] contribute to mass transport in thermocells. Therefore, mass transport resistance can be evaluated by measuring the time dependence of internal resistance of the thermocell (Figure 3-14). Though a highly porous electrode composed of micropores only, such as ACT, has significant advantages in terms of providing large electrochemical reaction sites, it might hinder the mass transport of reactants and products. It is noted in this regard that an electrode with hierarchical pore structure facilitates enhanced diffusion of ions into the electrode, as in vascular structures in nature [72-76]. The hierarchical feature of C-ACT pores is expected to improve mass transport resistance by contributing to enhanced ion transport. As shown in Figure 3-14, the increase in the internal resistance of the thermocell with a C-ACT electrode is relatively smaller than that with ACT and the resistance settles quickly down to a steady state within 60 s.

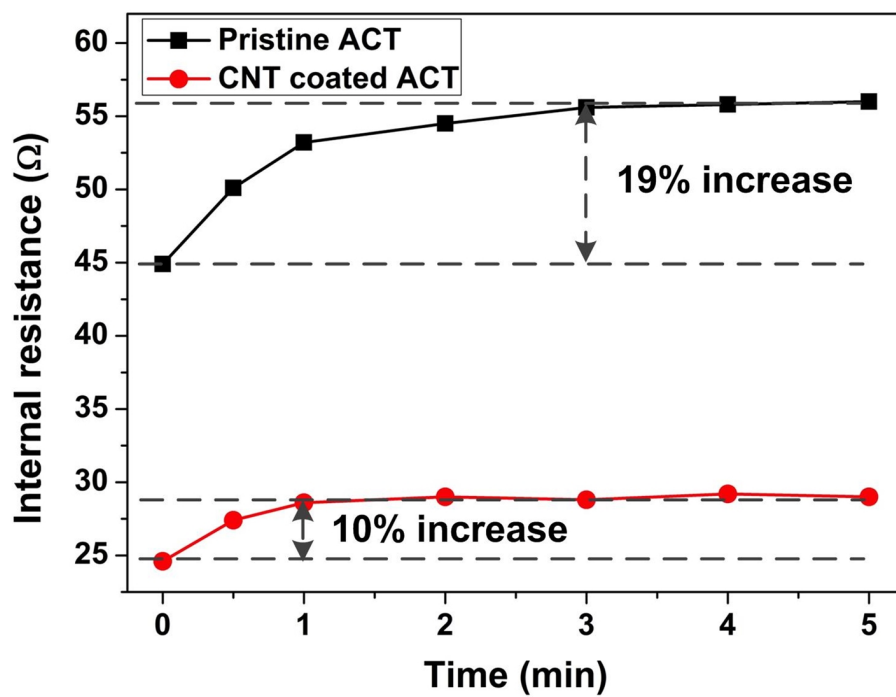


Figure 3-14. Time-dependent overall internal resistance change of the thermocell with ACT and C-ACT electrodes.

3.4.3 Characterization of plastic thermocell

Discharge characteristics of the thermocell are shown in Fig. 3-15. The voltage–current (E–I) relationship is given in Figure 3-15 as a function of time. In the measurements, the operating temperature—which is defined as the average of the temperatures at the hot and cold electrodes—was fixed at 20.5°C and the temperature difference was maintained at 3.4°C. The working area (C-ACT electrode size) was 2 cm × 2 cm. The internal resistance, i.e., the slope of the E–I curve, increases during cell discharge, reaching a steady state of 30.5 Ω (the inset of Figure 3-15). Due to the relatively short traveling path of ions (about 100 μm) and hierarchical porous structure of the electrode, the steady-state discharge of the thermocell could be reached within 1 min. The resistance variation from the initial to the steady state was measured to be 1.7 Ω. The cell potential and specific output power as a function of the current density at steady state is shown in Figure 3-16. It can be seen that the plastic thermocell generated j_{SC} of 0.39 A/m² (current of 152 μA) and P_{MAX} of 0.46 mW/m² (output power of 184 nW), indicating that power generation from body heat is feasible.

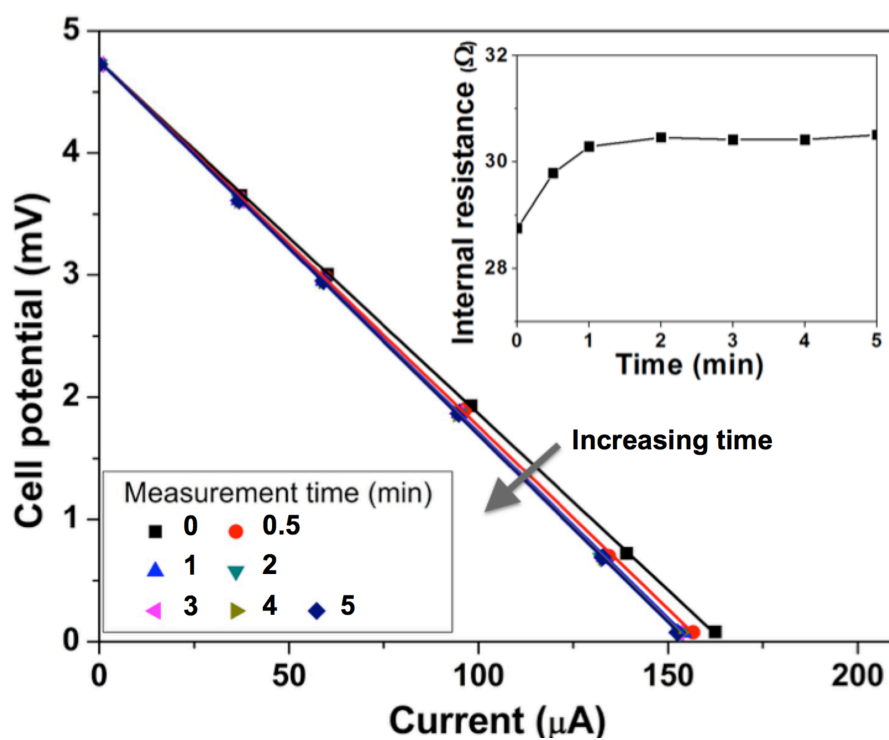


Figure 3-15. Dependence of cell potential on current with increasing time from the start of energy harvesting. The inset shows the dependence of internal resistance on time.

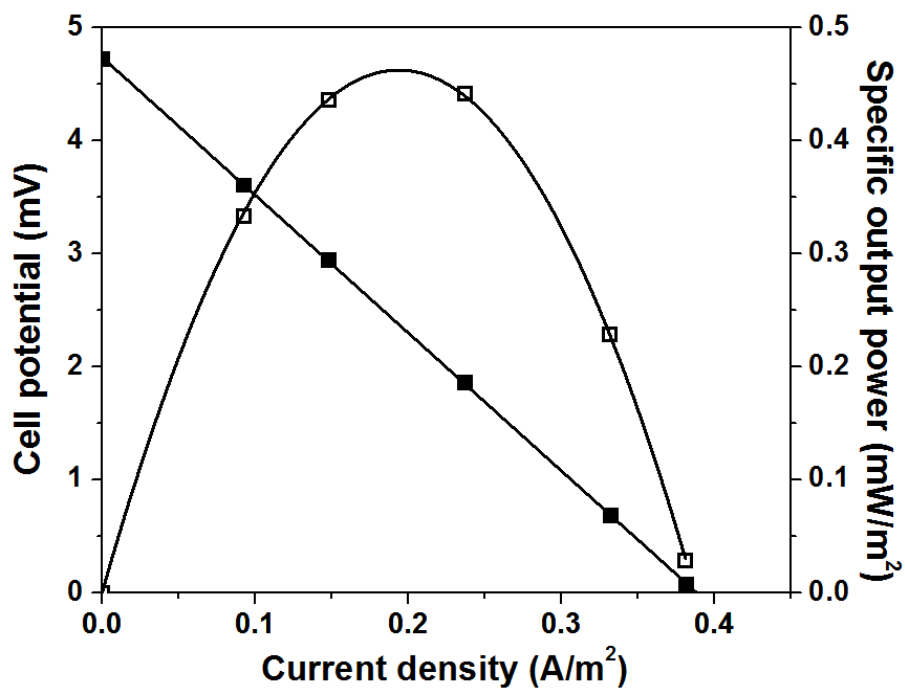


Figure 3-16. Plots of cell potential (solid square) and specific output power (open square) versus current density at steady state.

To explore the feasibility of power generation from a human body, the ambient temperature for the thermocell was varied, ranging from 5°C (cold weather) to 30°C (hot weather), while the other electrode was maintained at 36°C, which is the human body temperature. Because of the relatively high thermal resistance of the PET substrate, the temperature drop mainly occurs across the outer substrate layer, so that an ambient temperature of 5°C with the other electrode maintained at 36°C yielded a temperature difference of 3.4°C. Ambient temperatures of 10, 20, and 30 °C correspond to actual temperature differences of 2.9, 1.8, and 0.6°C, respectively.

As shown in Figure 3-17, the open-circuit potential (V_{OC}) increases with increasing temperature difference, resulting in a quadratic increase of the maximum power generated, P_{MAX} , which increases from 0.02 mW/m² for $\Delta T = 0.6^\circ\text{C}$ to 0.46 mW/m² for $\Delta T = 3.4^\circ\text{C}$ (Figure 3-18). For the maximum temperature difference used in the experiment (i.e., an operating temperature of 20.5°C), the thermocell gave a normalized current density of 0.114 A/m²K and a normalized maximum power density of 39.56 $\mu\text{W}/\text{m}^2\text{K}^2$.

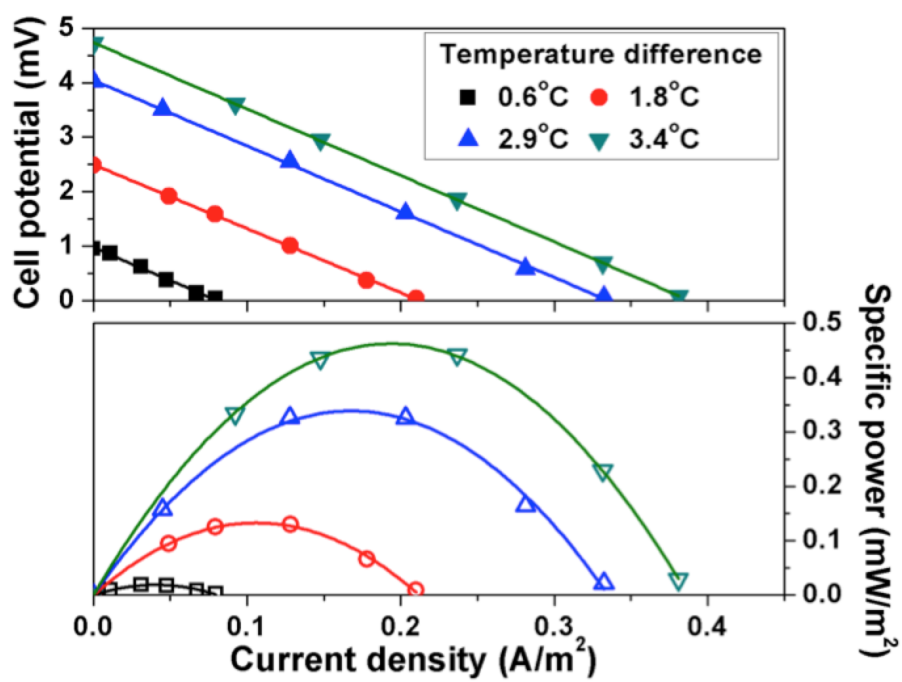


Figure 3-17. E-I curves and output power versus current density.

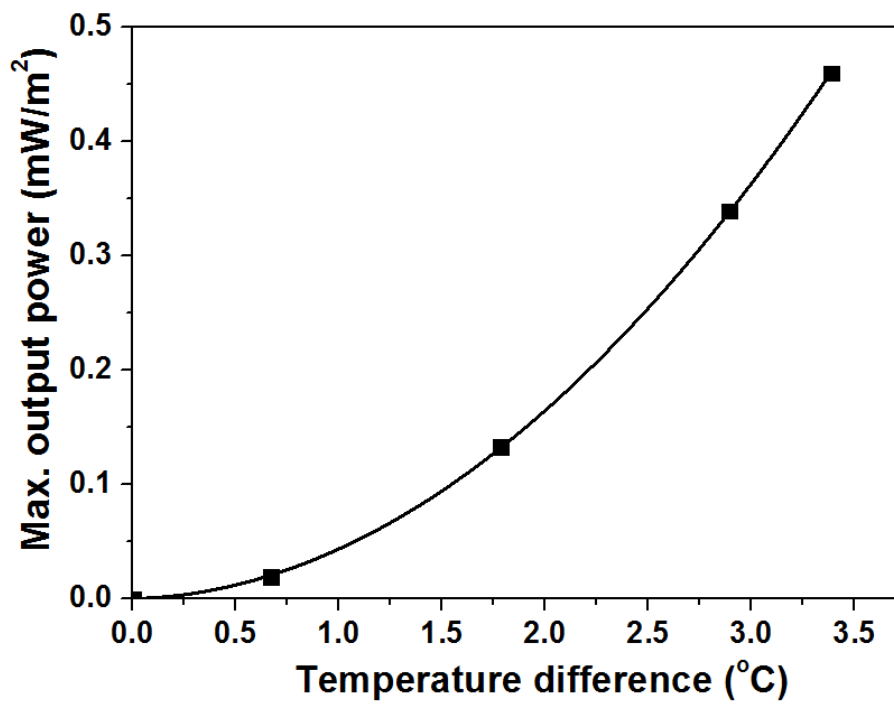


Figure 3-18. Maximum specific output power with respect to the temperature difference.

As shown in Figure 3-19, the internal resistance decreases with increasing operating temperature. An increase in the temperature should lead to an improvement in ion transport through the separator and also diffusion within the electrodes [17], resulting in an enhancement of the mass transport (Figure 3-20). This enhancement is confirmed by the result that the thermocell provided $j_{SC}/\Delta T$ of $0.122 \text{ A/m}^2\text{K}$ and $P_{MAX}/\Delta T^2$ of $42.83 \text{ } \mu\text{W/m}^2\text{K}^2$ at the high operating temperature of 33°C , values which are higher than those at an operating temperature of 20.5°C .

The thermocell produced stable values of V_{OC} and j_{SC} during 48 h of operation (Figure 3-21), which indicates that the device should be stable in long-term operation.

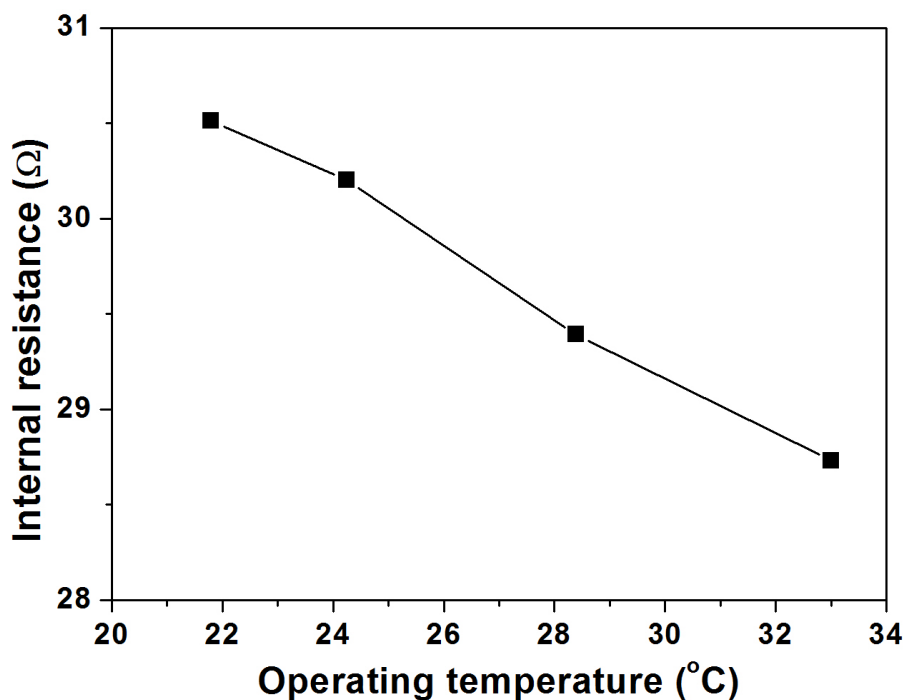


Figure 3-19. Dependence of internal resistance on operating temperature.

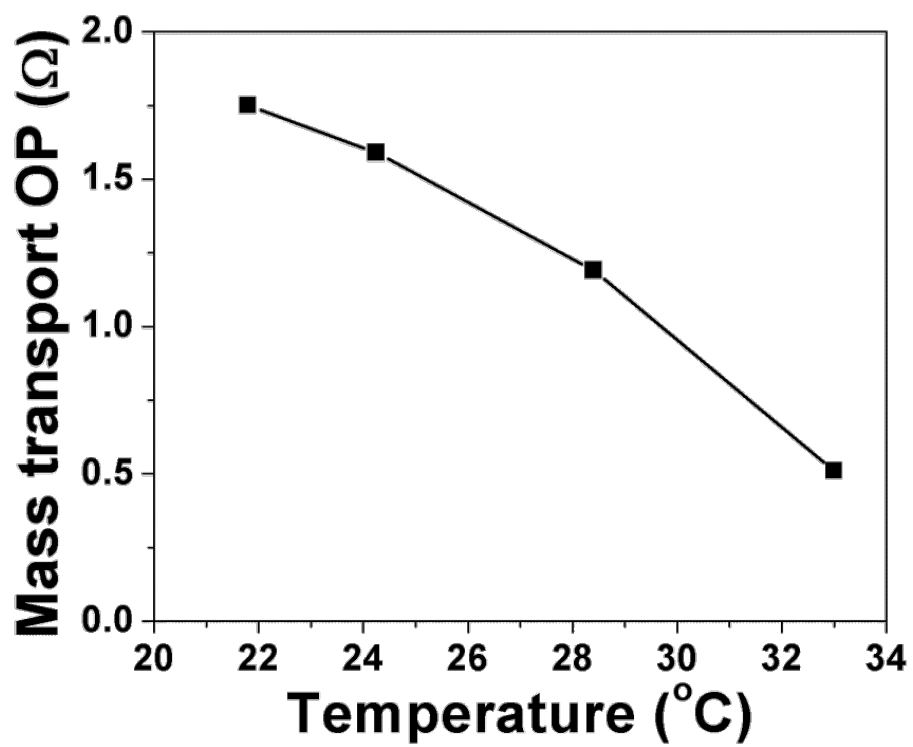


Figure 3-20. Mass transport resistance as a function of operating temperature.

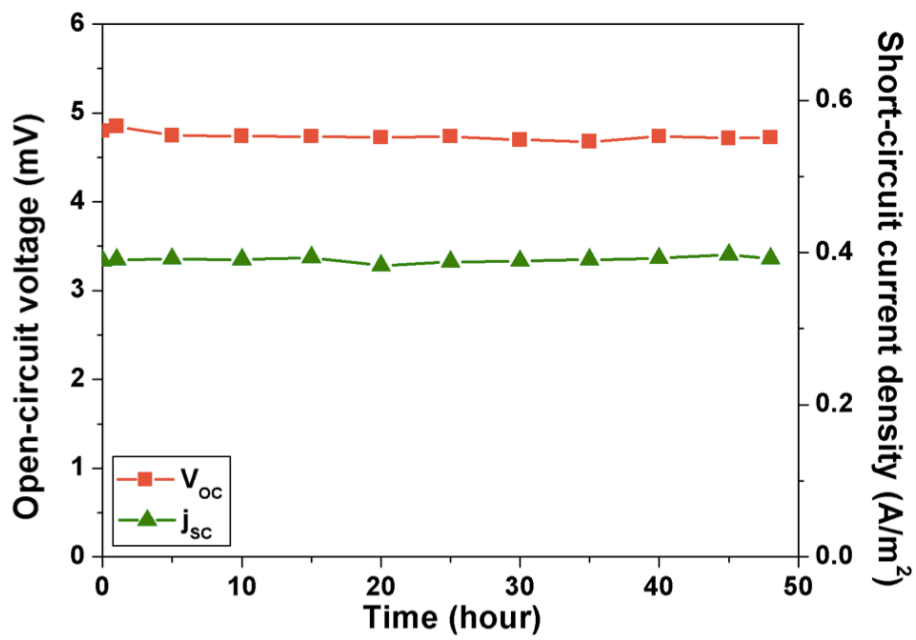


Figure 3-21. Dependence of open-circuit voltage and short-circuit current density on time with a temperature difference of $3.4^{\circ}C$.

The energy conversion efficiency (η) of the thermocells was calculating using

$$\eta = \frac{(1/4)V_{OC} \cdot I_{SC}}{A_c \cdot \kappa (\Delta T/d)} \quad (3.1)$$

where V_{OC} is the open-circuit voltage, I_{SC} is the short-circuit current, A_c is the cross sectional area of the cell, κ is the thermal conductivity of the electrolyte, ΔT is the temperature difference between electrodes and d is the electrode separation distance.

A direct comparison of PCE of different power conversion devices would be inaccurate, owing to complications that arise from the difference in operating temperatures used. A convenient method of standardizing power conversion measurements in thermal converters is to compare their power conversion efficiency (η_r), relative to that of a Carnot engine operating between the same temperatures.

$$\eta_r = \frac{\eta}{(\Delta T/T_H)} \quad (3.2)$$

where T_H is the hot temperature.

The relative power conversion efficiency was calculated using the eq. 3.1 and 3.2. The efficiency relative to a Carnot engine of the thermocell is 0.078% ($\eta_r = 0.078\%$).

Using thermal resistance model, the unexpected low temperature difference in the thermocell is analyzed as following

In steady state conduction, it is possible to take “thermal resistances” as the analog to electrical resistances. The analog of Q is current, and the analog of the temperature difference, $T_H - T_C$, is the voltage difference. From this perspective, the heat transferred can be defined as

$$Q = \frac{\kappa \cdot A}{L} (T_H - T_C) = \frac{T_H - T_C}{R_\theta} \quad (3.3)$$

where, κ is the thermal conductivity, A and L are the area and length, respectively, and R_θ is the thermal resistance.

For our thermocell configuration, the overall thermal resistance is given by

$$\begin{aligned} R_\theta &= R_{PET} + R_{electrolyte} + R_{PTE} \\ &= \frac{L_{PET}}{\kappa_{PET} \cdot A_{PET}} + \frac{L_{electrolyte}}{\kappa_{electrolyte} \cdot A_{electrolyte}} + \frac{L_{PET}}{\kappa_{PET} \cdot A_{PET}} \end{aligned} \quad (3.4)$$

Using the thermal conductivities and dimensions, the thermal resistance of PET is obtained as 1.67 K/W, showing higher value than that (1.45 K/W) of the electrolyte even though thickness is much thinner. Figure 3-22 shows that the theoretical temperature distribution is well matched to the measured temperatures.

In order to utilize heat from external sources more effectively, the thermal resistance of the packaging layer should be reduced so that the temperature drop across the outer wall is minimized. If stainless steel is used as the packaging layer under the same conditions of a total temperature difference

of 31°C (surrounding temperature of 5°C), the thermal resistance of the layer and the temperature difference between the electrodes will be 1.54×10^{-2} K/W and 19°C, respectively. In such a case, the output power will be increased to 58 mW/m².

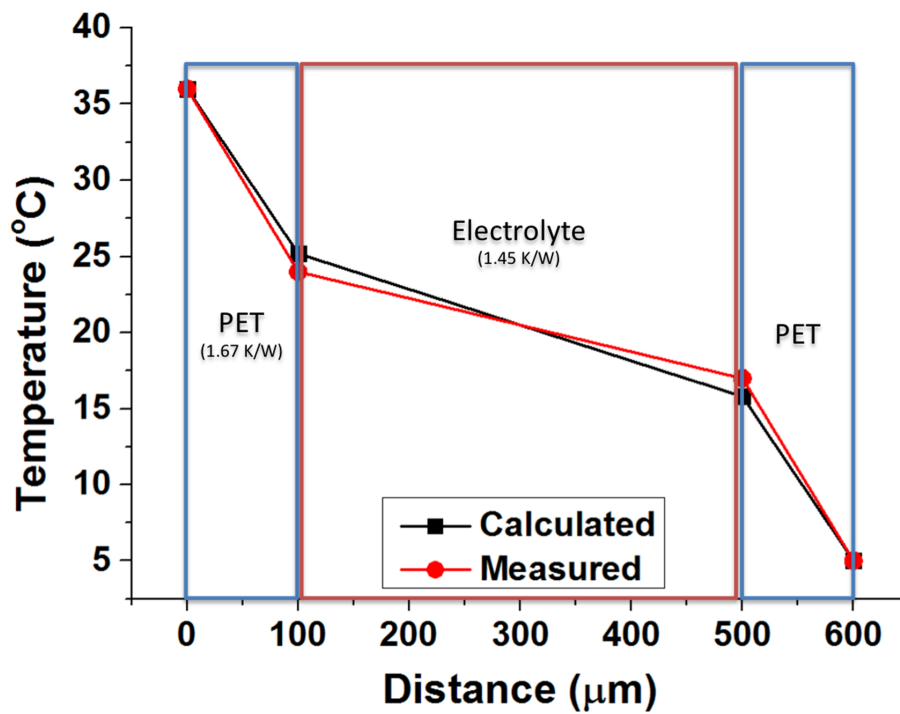


Figure 3-22. Temperature distribution comparison of calculated and measured temperatures at each interface in the thermocell.

3.4.4 Harvesting energy from human body and heat pipe

A good way to harness the heat from a human body is to attach the thermocell to a shirt. As a demonstration, a T-shirt embedded with the plastic thermocell was connected to a capacitor, which could be charged up by the power generated from the thermocell (Figure 3-23). The capacitor has a structure identical to that of the plastic thermocell, the only difference being the electrolyte of 1.0 M KCl solution. Figure 3-24 shows the charge/discharge behavior of the capacitor when the shirt was put on and off, demonstrating that the body heat can be harvested effectively with the thermocell T-shirt (power output of 11.7 nW).

A large source of waste heat can be found in power plants or various industrial facilities where large amounts of waste heat are lost through numerous pipes that carry hot fluids [16]. This waste heat can be harvested when a thermocell is employed. As proof of concept, a flexible thermocell was wrapped around a pipe with various curvatures, as depicted in the inset of Figure 3-25. The power generated from the thermocell without curvature, P_0 , was 0.54 mW/m^2 with a pipe temperature of 80°C and an ambient temperature of 24°C . It is interesting to observe that the power from the thermocell increases by more than 30% when it is wrapped around pipe (Figure 3-25), although the incremental increase diminishes as the curvature is increased. The increase could be attributed to the reduced contact resistance between the collecting wire and the textile electrode caused by the compression created when the thermocell is wrapped around the pipe.

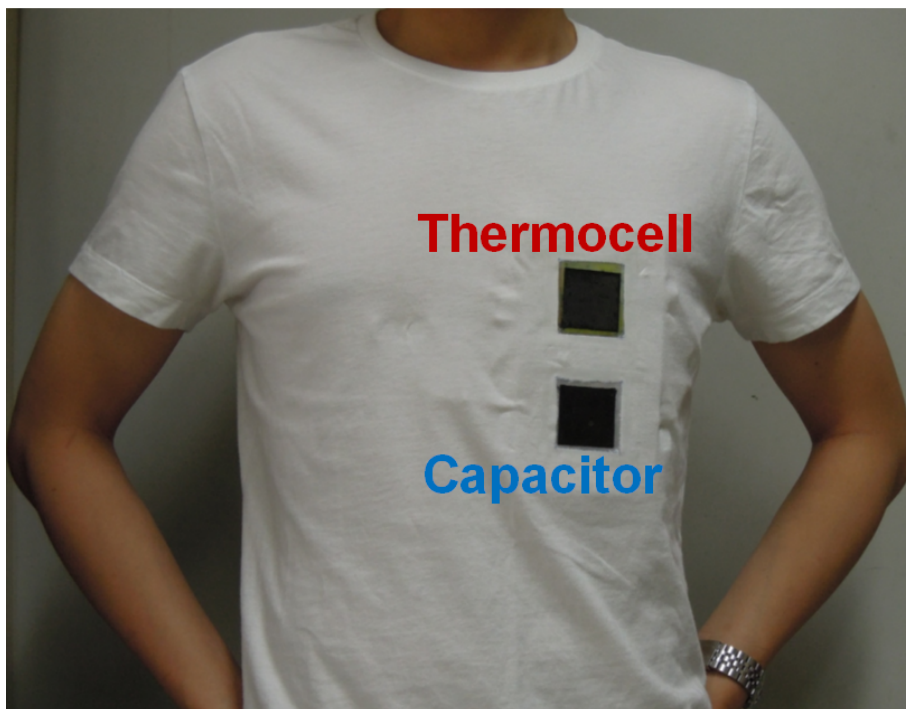


Figure 3-23. Photograph of the T-shirt embedded with the thermocell and capacitor, the latter for storing the power generated from the thermocell.

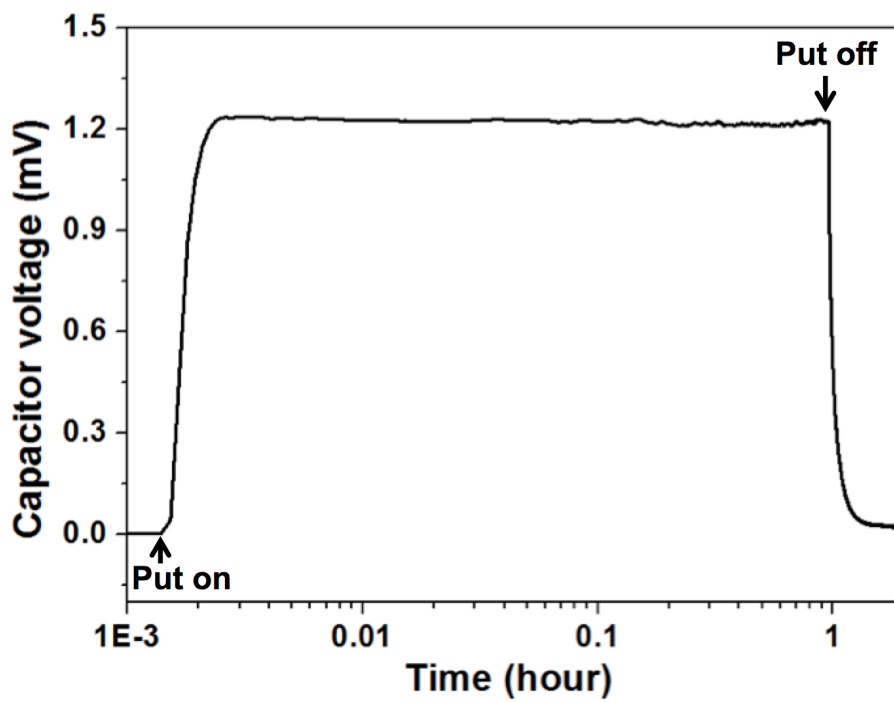


Figure 3-24. Charge/discharge of a capacitor connected to the thermocell.

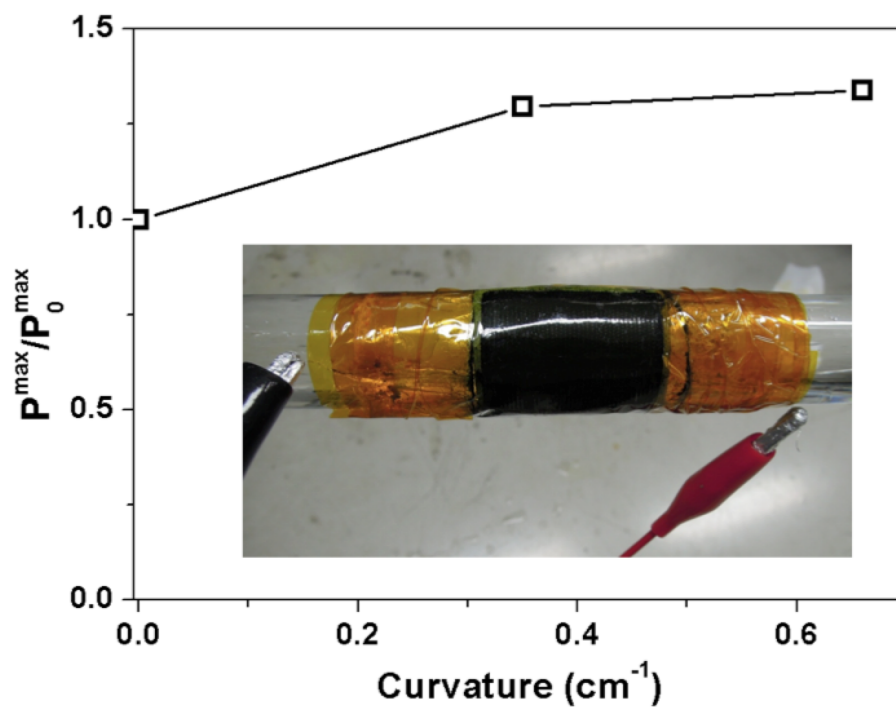


Figure 3-25. Normalized maximum power output for various curvature radii. Inset: photograph of a thermocell wrapped around a hot fluid pipe for energy harvesting.

A question that should be raised is whether the low power scavenged from low level heat sources can ever be put to good use. Although progressive advances in electronics should enable good use of the low power to the point of either replacing or augmenting battery usage with even human body heat, a commercial LED can be turned on with the thermocell fabricated here. For this purpose, four-serial plastic thermocells and a home-made voltage converter circuit were used, as shown in Figure 3-26. The serially connected thermocells generated a voltage of about 100 mV from a pipe with hot water of 80°C. Since the generated voltage is not high enough to light up a commercial LED with typical turn-on voltage of about 1.5 V, the output voltage was boosted using the converter circuit. The serially connected thermocell, modeled as an ideal source and a series resistance, is connected to an inductor through a transistor, which is used as a switch device and controlled by periodic pulses. With the converter circuit, the LED was turned on and stayed on. The actual red light from the LED is shown within the dark circle in the LED part of Figure 3-26.

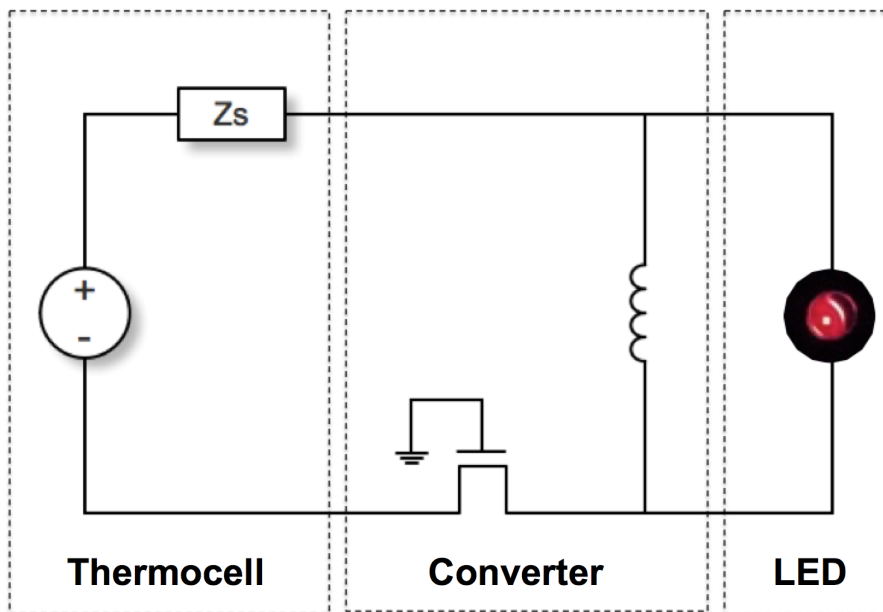


Figure 3-26. Circuit diagram depicting the lighting system for the LED, composed of thermocell, voltage converter and LED (the actual red light of the LED is shown within the dark circle in the LED part).

3.5 Conclusion

In conclusion, plastic thermo-electrochemical cells involving aqueous potassium ferricyanide/ferrocyanide electrolyte have been investigated as an alternative to conventional thermoelectrics for thermal energy harvesting. Plastic thermocells consist of all pliable materials such as polyethylene terephthalate (PET), fabrics, and wires. The plastic thermocell is flexible enough to be wearable on the human body and to be wrapped around cylindrical shapes. Hierarchical porous textiles coated with CNTs were also developed as an electrode to enhance the thermocell performance by lowering the three primary resistances.

In cold weather conditions (a surrounding temperature of 5 °C), the thermocell generates a short-circuit current density of 0.39 A/m² and maximum power density of 0.46 mW/m² from body heat (temperature of 36 °C).

For practical use, it is shown that the thermocell charges up a capacitor when worn on a T-shirt by a person.

It has been also demonstrated that the electrical energy generated from waste pipe heat by a serial array of the thermocells can power a typical commercial LED whose turn-on voltage is 1.5 V. The results indicate that the thermocell developed here can serve as a self-sustainable energy source. The flexible thermo- electrochemical device introduced here should inspire further research in the area of waste heat recovery.

Chapter 4. CNT Aerogel Sheet Electrodes for Thermocells

4.1 Introduction

Abundant heat from low-grade thermal streams is wasted because of the absence of efficient, inexpensive devices that convert this heat into electricity. To increase the energy conversion efficiency of thermocells, carbon nanomaterials have been introduced as cell electrodes to take advantage of the fast redox processes, high thermal and electrical conductivities, and high gravimetric surface areas that these materials can provide. Hu et al [4] reported an energy conversion efficiency as high as 1.4%, relative to Carnot cycle efficiency, when carbon multi-walled nanotube (MWNT) buckypaper was used for thermocell electrodes. This efficiency was raised to 2.6% by introducing a carbon single-walled nanotube (SWNT)/reduced graphene oxide (rGO) composite electrode [16]. Improved mass transport due to enhanced porosity of the optimized SWNT/rGO composite was found responsible for the efficiency enhancement. Despite recent advances in thermocell technology, a significant efficiency increase is required for thermocells to become commercially attractive, considering that the Carnot relative efficiency has to be 2 to 5% for commercial viability [12].

4.2 Chapter Aims

In this chapter, planar and cylindrically wound carbon nanotube (CNT) aerogel sheet as thermocell electrodes and various additional ways to optimize Carnot efficiency are exploited. The deployed optimization strategies to improve thermocell performance involve use of carbon nanotube aerogel sheets as electrodes, removal of low activity carbonaceous impurities that limit electron transfer kinetics, decoration of CNT sheets with catalytic platinum nanoparticles, mechanical compression of nanotube sheets to tune conductivity and porosity, and the utilization of cylindrical cell geometry. The output power density generated by a described cylindrical thermocell reached 6.6 W/m^2 for a 51°C inter-electrode temperature difference, which corresponds to a Carnot-relative efficiency of 4.2% (i.e., 4.2% of the maximum energy conversion efficiency possible for a heat engine operating between two given temperatures).

4.3 Experimental setup

4.3.1 Preparation and post-treatment of CNT aerogel sheet electrodes

Vertically aligned MWNT arrays were grown on an iron-catalyst-coated silicon (Si) substrate by chemical vapor deposition of acetylene gas [77]. The diameter and height of MWNTs are $\sim 10 \text{ nm}$ and $\sim 200 \mu\text{m}$, respectively.

As shown in Figure 4-1, CNT sheet was continuously drawn from a sidewall of the MWNT forests using a dry spinning process [17] and wrapped around a rectangular tungsten frame for planar-type electrodes and tungsten wire for cylinder-type electrodes, using a connected rotating motor at 10 rpm. The planar electrode has a thickness of 100 μm and area of $1.0 \times 1.0 \text{ cm}^2$ and the cylinder electrodes had a diameter and width of 3 mm and 2.0 cm, respectively. Thermal annealing of the carbon nanotube sheets to remove carbonaceous impurities was performed in ambient atmosphere using a halogen-lamp-heated quartz tube furnace (Figure 4-2), which had a ramp time to target temperatures (from 300 to 400°C) of one minute.

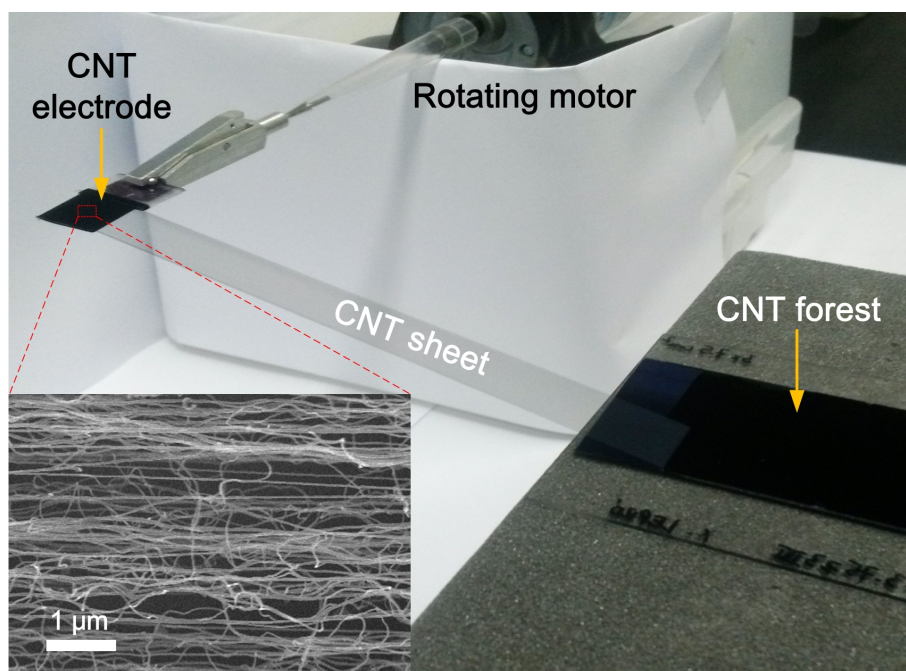


Figure 4-1. Experimental setup for preparation of a planar-type CNT electrode. The inset shows a SEM image of a CNT sheet electrode.

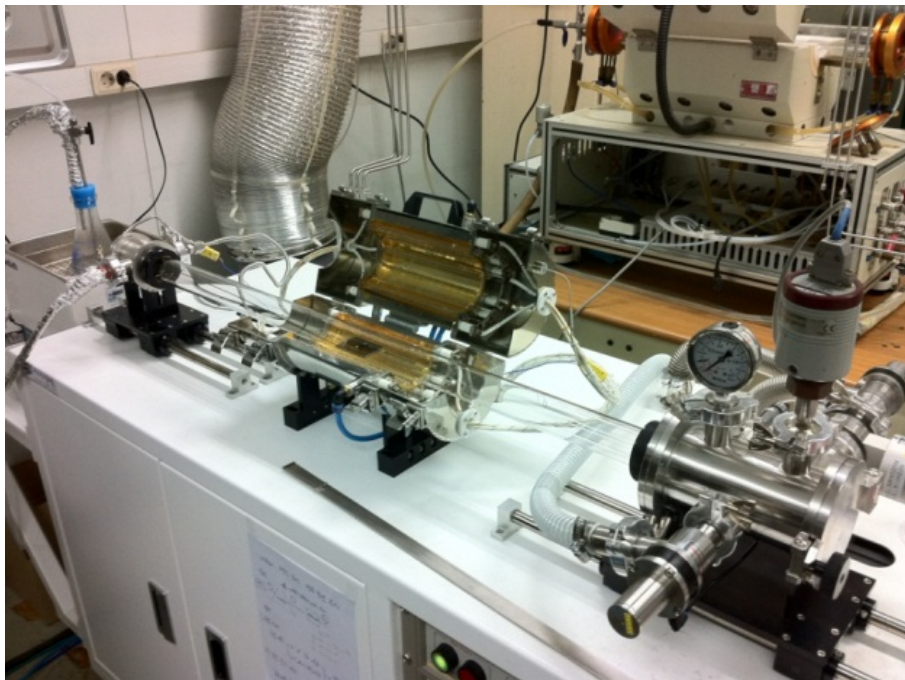


Figure 4-2. Optical image of a furnace with halogen-lamp-heated quartz for thermal annealing.

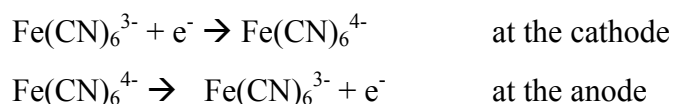
For deposition of platinum nanoparticles by chemical reduction of a platinum salt solution [78], 3.75 mg of K_2PtCl_4 (Aldrich) was dissolved in 50 mL of diluted ethylene glycol solution (3:2 by volume ethylene glycol:deionized DI water). Afterwards, the described thermally-oxidized CNT sheet electrodes were immersed in the synthetic solution and Pt nanoparticle deposition was permitted for 3 hours at $100^\circ C$ with weak stirring to prevent mechanical damage to CNT sheet. After the reaction, the pH of the solution was decreased to 2 using HCl and the electrode was washed with DI water several times to remove excess ethylene glycol. In order to avoid liquid-based aerogel densification during liquid evaporation, the electrodes were not dried before use in the thermocells.

4.3.2 Flow cell configuration for evaluation of diffusion limiting current

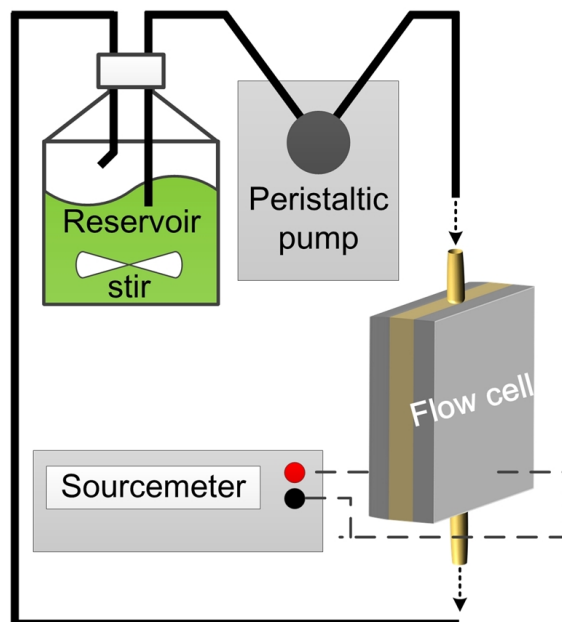
Mass transfer coefficients were derived from the limiting current method based on the reduction of ferricyanide ions. The experiments were performed using electrochemical flow cell configuration as shown in Figure 4-3. The cell is formed with parallel collecting electrodes with an inter-electrode distance of 10 mm. $1.0 \times 1.0 \text{ cm}^2$ of CNT samples were placed on the center of the collecting electrodes ($4.0 \times 1.5 \text{ cm}^2$) and other exposed area was covered with insulating PET film (Figure 4-3b). The buckypaper electrode (Figure 4-4a) was made by filtration process with MWNT colloidal solution. The sheet electrode (Figure 4-4b) was fabricated using dry spinning method as explained previously. The volumetric densities of

the buckypaper and the sheet were measured as 174 and 4.8 mg/cm³, respectively. The thickness of the CNT samples were set to 100 μm. the electrolyte is stored in a glass container and circulated through the electrolytic cell by peristaltic pump (Longer pump, BT100-2J). The electrolyte flow rate was kept at 6.6 × 10⁻⁶ m³/s for laminar flow in a cell channel. A power supply (Keithley, 2400 Sourcemeter) is used to drive electrochemical reactions.

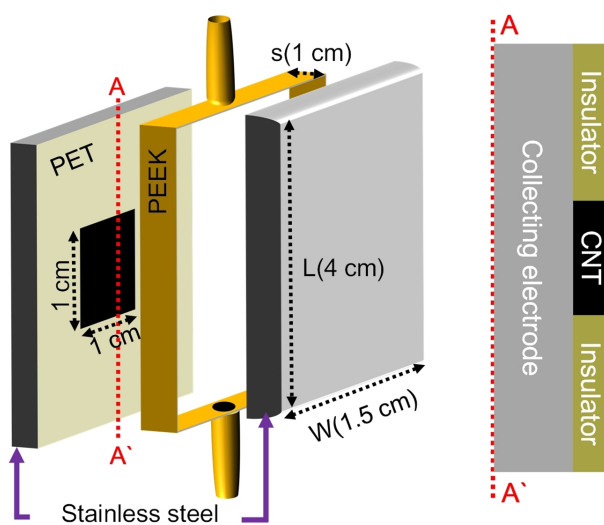
The reactions in this system are as followings:



Aqueous solution of potassium ferricyanide ranging from 20 to 80 mM in 0.5 M NaOH was used to determine the dependence of limiting current on the concentration of reduction ion. The ferrocyanide concentration was double the ferricyanide concentration to ensure a limiting reaction rate at the cathode.

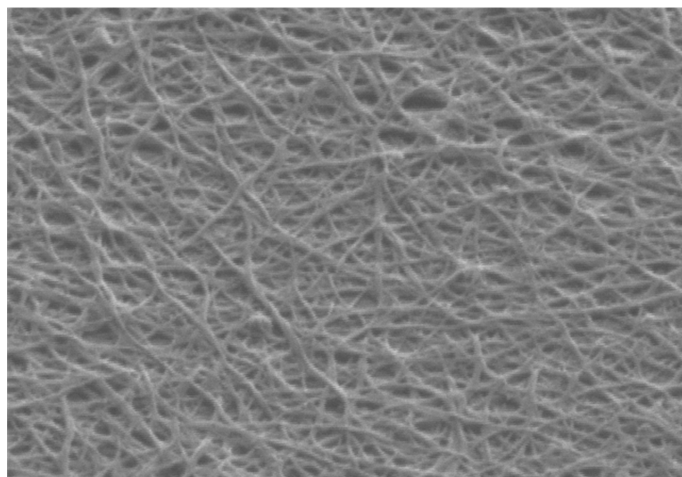


(a)

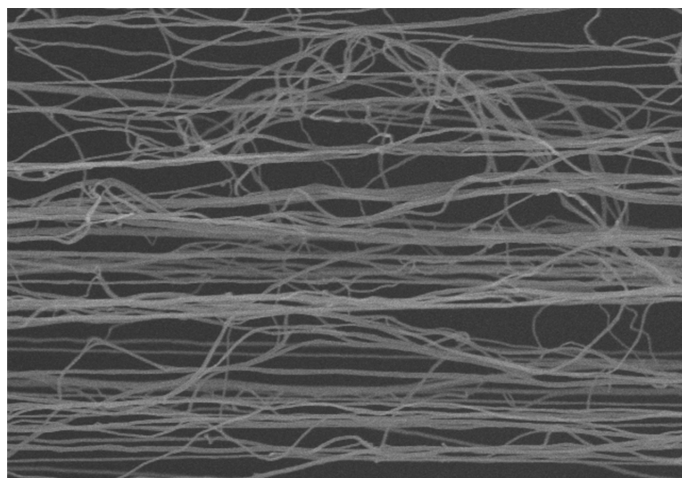


(b)

Figure 4-3. a) Experimental setup of electrochemical flow cell for determination of mass transfer coefficient. b) Exploded view of the flow cell.



(a)



(b)

Figure 4-4. SEM images of a) CNT buckypaper and b) CNT aerogel sheet.

4.3.3 Thermocell testing and characterization

The electrolyte used in all tests was 0.4 M aqueous solution of $\text{Fe}(\text{CN})_6^{4-}/\text{Fe}(\text{CN})_6^{3-}$. For evaluation of planar thermocells, the cell was placed between two fluid-heated plates that were connected to hot and cold thermostatic bath to provide $\pm 0.1^\circ\text{C}$ control of plate temperatures. For cylindrical thermocell testing, the glass wall surrounding each cell electrode (which are separated by 2.5 cm) was wrapped and bonded with a TYGON[®] tube, through which cooling fluid or heating fluid was passed. While the hot and cold fluid temperatures were 100°C and 30°C , respectively, temperature drops between the heating and cooling sources and the respective electrodes reduced the inter-electrode temperature difference (obtained from the measured V_{OC} and thermo-electrochemical Seebeck coefficient) from 70°C to $\Delta T \sim 51.4^\circ\text{C}$. A voltage-current meter (Keithley, 2000 Multimeter) was used for characterizing cell voltage versus cell current for different external resistive loads, the thereby determining power output. The glass tube having 3 mm inside diameter was used for the cylinder thermocell experiments (Figure 4-5).

Raman spectra as a function of the thermal oxidation times and the temperature used for removing carbonaceous impurities were recorded 514 nm excitation using a Renishaw in Via Raman Microscope. Sample structure was further characterized by field-emission scanning electron microscopy (FE-SEM, Hitachi-S4800) and high-resolution transmission electron microscopy (HR-TEM, JEM-300F). electrochemical impedance measurements were conducted in the frequency range between 10 kHz and

50 mHz using a commercial instrument (Zahner, IM6ex). Cyclic voltammetry (using a Digi-Ivy, DY 2100 instrument) used a 10 mM $\text{K}_3\text{Fe}(\text{CN})_6$ with 0.1 M KCl as the supporting electrolyte in aqueous solution and a scan rate of 100 mV/s. Platinum and Ag/AgCl electrodes were used as counter and reference electrodes, respectively, for the CV measurements.

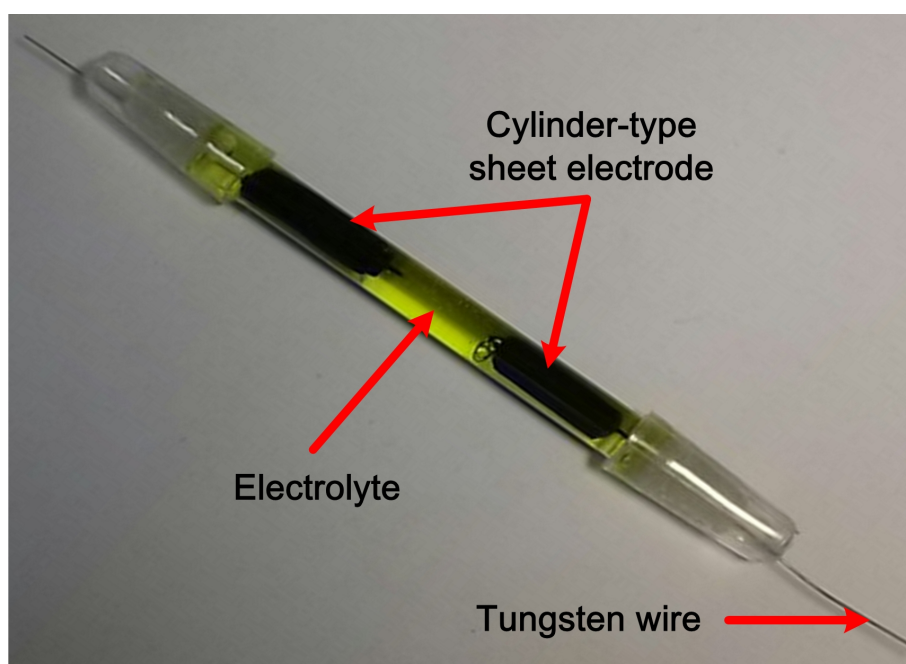


Figure 4-5. Optical image of assembled cylinder-type thermocell.

4.4 Results and discussion

4.4.1 Determination of mass transfer coefficient CNT aerogel sheet

Since the current output of thermocells is determined by the number of ions reacting on external and internal electrode surfaces, fast mass transport of redox molecules into porous electrodes is required for high performance. The MWNT aerogel sheets have a high surface area and an ultra-low areal density [79]. Moreover, compared to conventional CNT buckypaper (made by filtration-based sheet fabrication), the porous and highly aligned CNT architecture of the sheet provide less tortuous ionic diffusion pathways, as shown in Figure 4-4. The specific surface area and pore volume of the aerogel sheet was measured as $147 \text{ m}^2/\text{g}$ and $0.228 \text{ m}^3/\text{g}$, respectively, which are much higher values than $81 \text{ m}^2/\text{g}$ and $0.164 \text{ m}^3/\text{g}$ of the buckypaper. These features facilitate high ion accessibility when these sheets are used as electrodes. Mass transport characteristics of CNT buckypaper and aerogel sheet using electrochemical flow cell were investigated. Mass transfer coefficient (k) can be determined by diffusion-limiting current method [80,81].

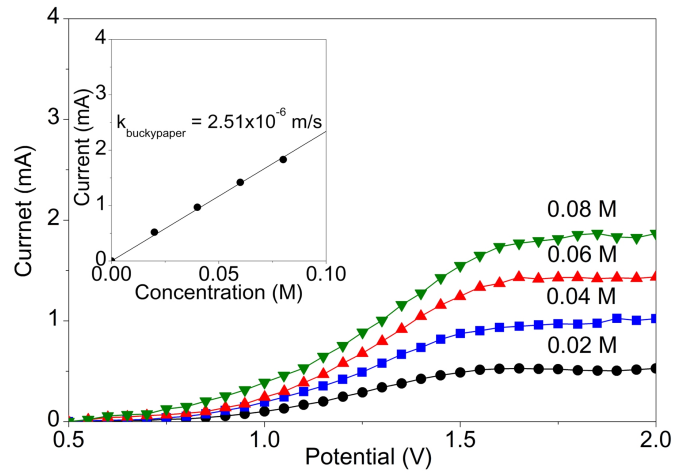
Diffusion limiting current technique is relatively simple and fast method for characterization of mass transport properties. Furthermore, this method is quite accurate for transport rate measurement compared to other methods, including weight loss, hydrodynamic pressure-drop measurements. The limiting-current method is based on driving an electrochemical reaction to

the maximum possible rate, where it is limited by mass transport. The limit is indicated by a current plateau on a polarization curve plot. Therefore, the rate of electrochemical reaction (current) depends only on rate of mass transfer as follows:

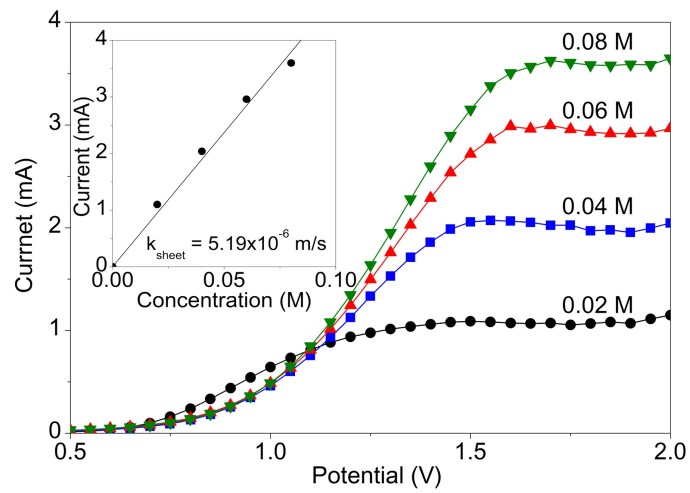
$$k = \frac{i_L}{nFAC_\infty} \quad (4.1)$$

where i_L is the limiting current, n is the number of electrons, F is the faraday constant. A is the electrode area, C_∞ is the bulk species concentration.

Polarization curves of the buckypaper and the aerogel sheet are shown in Figure 4-6a and b, respectively. The limiting currents (plateau region) are clearly observed and show different values between CNT buckypaper and aerogel sheet. The limiting currents as a function of the concentration for the buckypaper (inset of Figure 4-6a) and the aerogel sheet (inset of Figure 4-6b) are presented, showing a linear dependence. From the eq. 4.1, the mass transfer coefficients of the buckypaper and the sheet are obtained as 2.51×10^{-6} and 5.19×10^{-6} m/s, respectively. The aerogel sheet has 2.0 fold higher k value than the buckypaper. This indicates that facile diffusion of the redox ions occurs deep within the CNT network, resulting in faster access to higher redox-active surface area and correspondingly increased current, as schematically depicted in Figure 4-7.



(a)

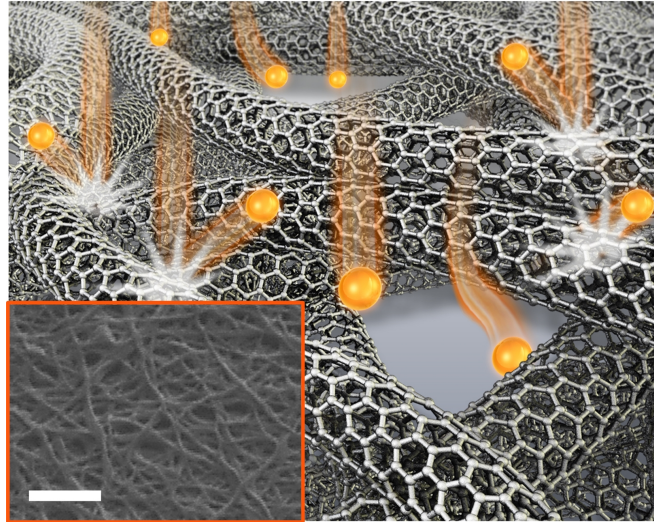


(b)

Figure 4-6. Characterization of mass transfer kinetics for CNT buckypaper and aerogel sheet. Polarization curves and dependence of limiting current on ferrocyanide concentration (inset) for a) the buckypaper and b) the aerogel sheet.

CNT buckypaper

- Random network / poor transport



CNT aerogel sheet

- Aligned morphology / facile diffusion

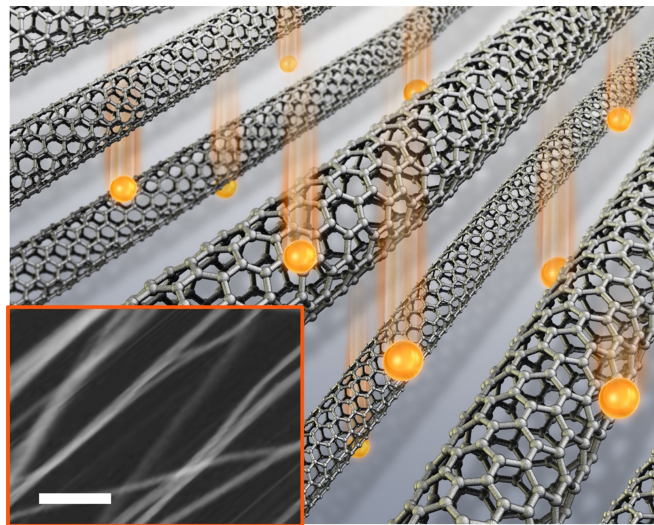


Figure 4-7. Illustrations and SEM micrographs (inset) providing comparison of the morphologies to ion transport (all scale bars are 300 nm long).

To model mass transport processes, dimensional analysis is commonly used. The application to the description of the mass transport processes that occur in an electrochemical cell gives three nondimensional groups: the Sherwood number (Sh); the Reynolds number (Re); and the Schmidt number (Sc). These groups relate the mass transport coefficient with the diffusivity D (m^2/s), the characteristic length parameter d_e (m), the fluid velocity u (m/s), and the kinematic viscosity of the fluid ν (m^2/s). The physical properties of the electrolyte are presented in Table 2 [80].

An approximation of the mass transfer coefficient was also obtained theoretically, on the basis of the definition of the Sherwood parameter. This taking profits from the relationship proposed by Leveque (eq. 4.2), for a laminar flow in a rectangular channel, and of the definitions of Re and Sc parameters.

$$Sh = \frac{k \cdot d_e}{D} \quad (4.2)$$

$$Sh = 1.85 \left[Re \cdot Sc \frac{d_e}{L} \right]^{1/3} \quad (4.3)$$

where

$$Re = \frac{u \cdot d_e}{L} \quad (4.4)$$

$$Sc = \frac{\nu}{D} \quad (4.5)$$

$$d_e = \frac{2(L \times s)}{L + s} \quad (4.6)$$

Table 2. Physical properties of the electrolyte at 20°C.

| | | |
|--|-------------------------|----------------------------|
| Concentration of $\text{Fe}(\text{CN})_6^{3-}$ | 0.005 | M |
| Concentration of $\text{Fe}(\text{CN})_6^{4-}$ | 0.01 | M |
| Concentration of NaOH | 0.5 | M |
| Density | 1020.5 | Kg/m^3 |
| Viscosity | 1.105×10^{-3} | $\text{Kg/m}\cdot\text{s}$ |
| Kinematic viscosity | 1.083×10^{-6} | m^2/s |
| Diffusivity of ferricyanide ion | 6.631×10^{-10} | m^2/s |
| Schmidt number | 1633 | |

For electrolyte flow of $6.6 \times 10^{-6} \text{ m}^3/\text{s}$, Sh and Re numbers of 139 and 650 are respectively obtained using eq. 4.3 and 4.4, respectively, showing that the flow is laminar in the flow channel of the cell (Re number less than 2100). The mass transfer coefficient value, calculated using eq. 4.2, results therefore to be $5.76 \times 10^{-6} \text{ m/s}$. This theoretical value of k is consistent with the experimentally determined mass transfer coefficient of the sheet electrode ($5.19 \times 10^{-6} \text{ m/s}$), suggesting that the homogeneous laminar flow is formed in the channel and the CNT electrode might suffer from uniform mass transport limitation.

4.4.2 Thermal optimization of surface purity of sheet electrode

It is well known that impurities, such as carbonaceous byproducts, are introduced during CNT synthesis [82]. A coating of these impurities on CNTs could restrict charge exchange with redox ions in the electrolyte, thereby degrading cell performance [83]. Various efforts have been made to remove undesirable amorphous carbon from CNT surfaces, for the purpose of improving performance for diverse applications of CNTs [83,84]. Taking advantage of the difference in oxidation rate in air between CNT and byproducts, forest-drawn CNT sheets, which are ultimately used as electrodes were purified using thermal oxidation method.

To find the optimum heating schedule, the oxidation temperature was first varied in the range of 300-400°C, while the oxidation time was held constant at 5 minutes. The purity of the CNT sheets was characterized using

Raman spectroscopy for 514 nm excitation. The Raman spectrum for an as-drawn sheet is shown in figure 4-8.

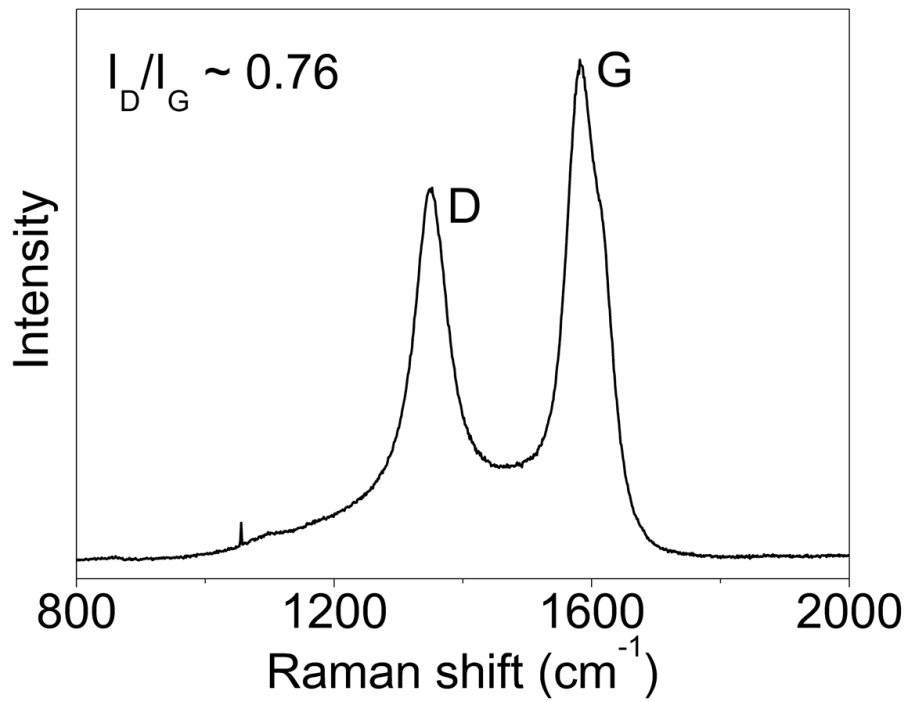


Figure 4-8. Raman spectrum for an as-drawn CNT sheet, showing I_D/I_G ratio of about 0.76.

The effect of oxidation temperature on the Raman intensity ratio of D band to G band (I_D/I_G) is shown in Figure 4-9, where the D band peak corresponds to defective carbon (like in amorphous carbon or carbon in defect sites) and the G band arises from ordered sp^2 carbons [42]. The minimum ratio I_D/I_G occurs at anneal temperature between 325 and 350°C, signifying that higher anneal temperatures should not be used for annealing times as short as 5 minutes. For further optimization of CNT aerogel sheet quality, the anneal temperature was fixed at 340°C and the heating time was varied between 0 and 60 minutes in order to further minimize the I_D/I_G ratio (Figure 4-10). The merit of this method for removing CNT impurities was confirmed by HR-TEM images of MWNTs in the annealed sheets. The non-annealed MWNT (Figure 4-11a) is covered with a carbonaceous coating, which is reduced by the 5 minute anneal at 340°C (Figure 4-11b), and eliminated by a 15 minute anneal at 340°C (Figure 4-11c), which corresponds to the minimum obtained ratio of I_D/I_G in Figure 4-10

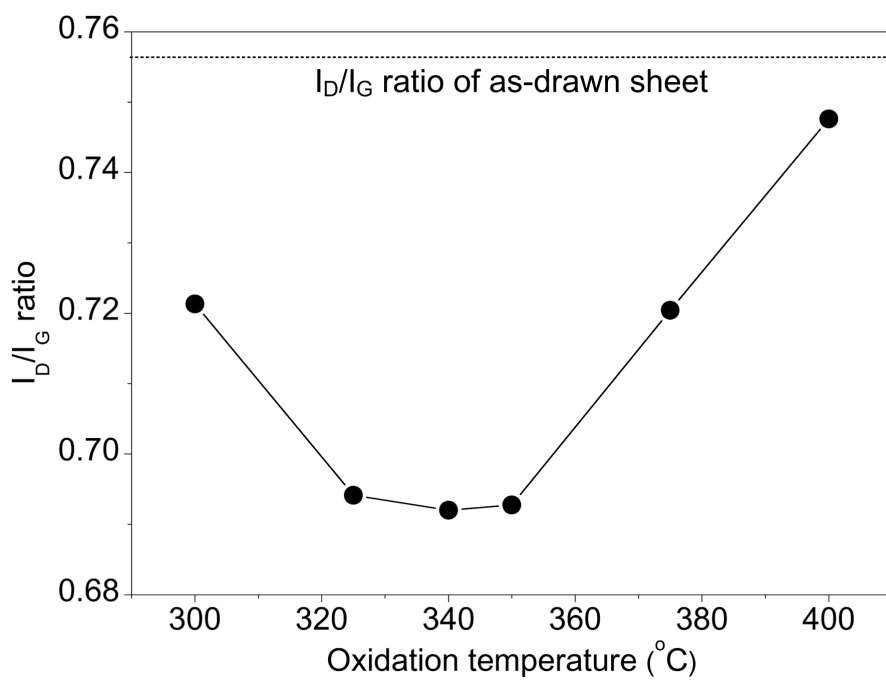


Figure 4-9. The dependence of I_D/I_G ratio on oxidation temperature for a 5 minute anneal of CNT aerogel sheets in ambient air.

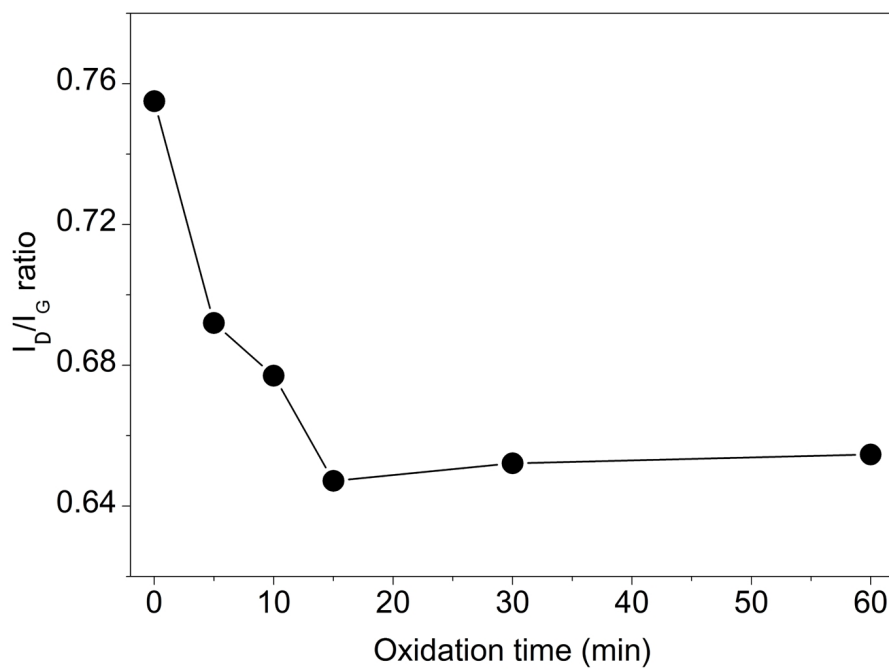
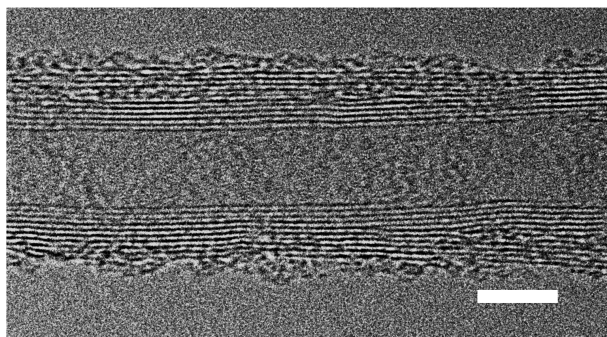
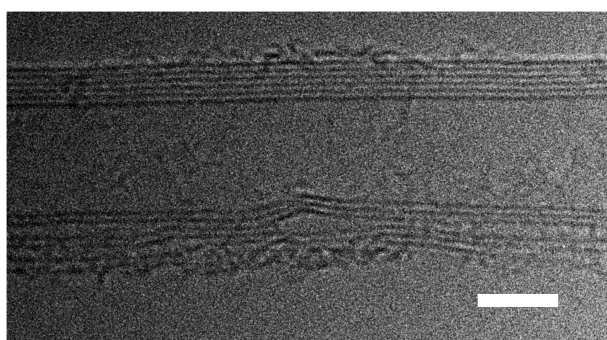


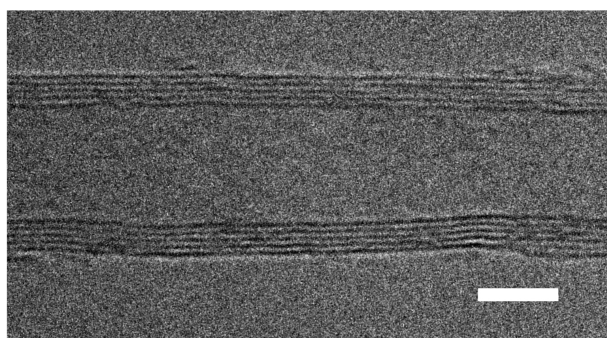
Figure 4-10. The dependence of the I_D/I_G ratio for CNT aerogel sheets on oxidation time in ambient air at 340°C.



(a)



(b)



(c)

Figure 4-11. HR-TEM images of a) as-drawn, b) 5 minute treated, and c) 15 minute treated CNT aerogel sheets (all scale bars are 5 nm long).

Thermocell performance was strongly affected by the annealing time at 340°C, as shown in Figure 4-12. In this experiment, the hot plate temperature was maintained at 25°C and cold plate temperature was at 5°C. While this temperature difference (ΔT) of 20°C was applied between heating and cooling plates, the actual ΔT between the electrodes, which was calculated using the open-circuit voltage and the observed thermo-electrochemical Seebeck coefficient (1.4 mV/K), was smaller (17.5°C). This difference is caused by thermal resistances (and corresponding temperature drops) at the interfaces between hot and cold electrodes and the respective heating and cooling plates. The curves of cell voltage versus areal current density and the corresponding power density curves obtained for various thermal oxidation times (shown in Figure 4-9) reveal that a lower I_D/I_G ratio, indicating that a cleaner CNT sheet, yields a higher maximum output power. The maximized areal power density (P_{MAX}), normalized to the square of the inter-electrode temperature difference (ΔT^2), is shown as a function of thermal oxidation time at 340°C in Figure 4-13. A 186% increase (from 0.07 to 0.13 mW/m²K²) in the $P_{MAX}/\Delta T^2$ is seen to have resulted from removing carbonaceous impurities from the surfaces of CNTs and CNT bundles. This optimum thermal oxidation condition (15 minutes at 340°C) was used for further experiments.

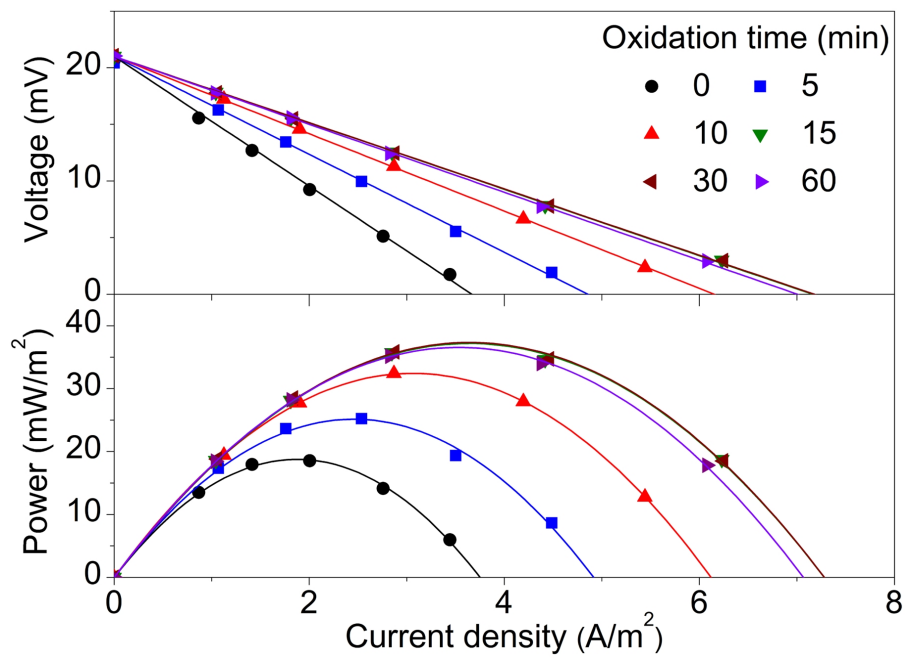


Figure 4-12. Cell voltage versus current density (top) and cell power density versus current density (bottom) for samples having different thermal oxidation times.

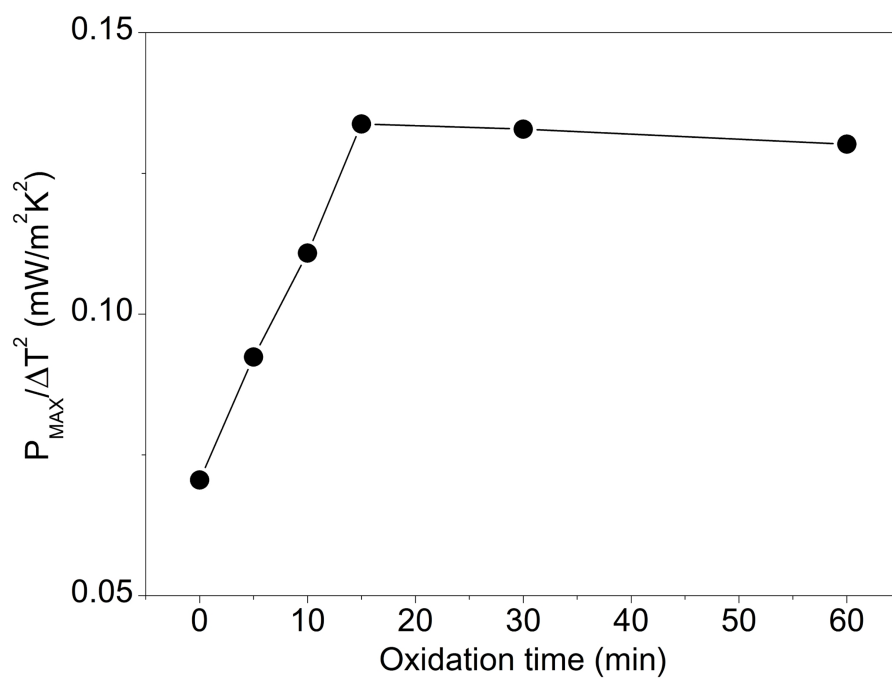


Figure 4-13. Maximum power density normalized to the inter-electrode temperature difference ($P_{MAX}/\Delta T^2$) as a function of thermal oxidation time.

To explain this major improvement in performance, electrochemical impedance measurements was used to characterize the three primary internal resistances of the thermocell (i.e., the activation, ohmic, and mass transport resistances) [85]. The activation resistance is the loss incurred in overcoming the activation barrier associated with reactions at the electrodes. The ohmic resistance is mainly due to the series resistances of electrode and electrolyte and the mass transport resistance is associated with the kinetics of ion diffusion and convection in the thermocell. The changes in these internal resistances with respect to heating time during sheet oxidation at 340°C are shown in Figure 4-14. This figure shows that a major reduction in the activation resistance is realized by removal of carbonaceous impurities, while the decrease in the combined ohmic and mass transport resistances is much smaller. This result indicates that amorphous carbon covering the surface of CNT hinders electrochemical reaction, resulting in performance degradation.

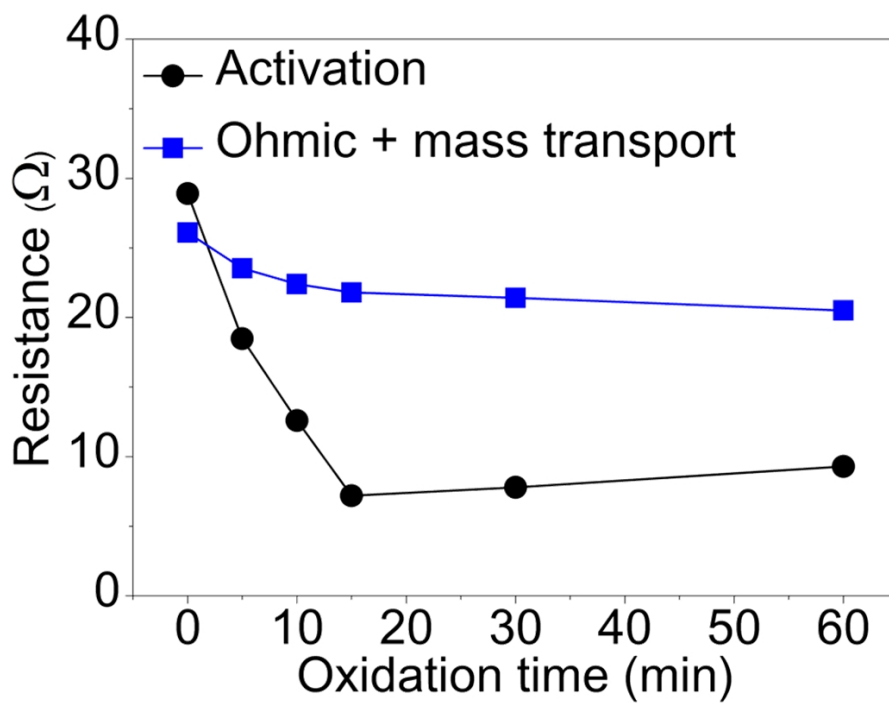


Figure 4-14. The dependence of activation resistance and the sum of ohmic and mass transport resistance on thermal oxidation time.

4.4.3 Mechanical compression for optimization of ohmic resistance

The fact that the electrode is an aerogel implies that increased contact between CNTs (and correspondingly decreased inter-electrode electrical and thermal resistances) could be realized by compressing the electrode. However, it should also be realized that the correspondingly increased density can restrict the speed and extent of ion transport into electrode depths. To evaluate these opposing effects, mechanical compression of a planar electrode was accomplished by pressing CNT sheets (wrapped on the tungsten frame used for electrode fabrication), using two silicon wafers that were coated with gold films (which provide low adhesion to the CNT sheet stack). The dependence of electrode density on the mechanical compression is presented in the Figure 4-15. As expected, density of the CNT electrode increases with increasing compressive strain. The maximum obtained power density, normalized to ΔT^2 , is plotted in Figure 4-16 as a function of the density of the electrode. These results show that $P_{MAX}/\Delta T^2$ is maximized for ~15% sheet compression, and that this compression provides a 23% increase in this performance metric (from 0.13 to 0.16 mW/m²K²).

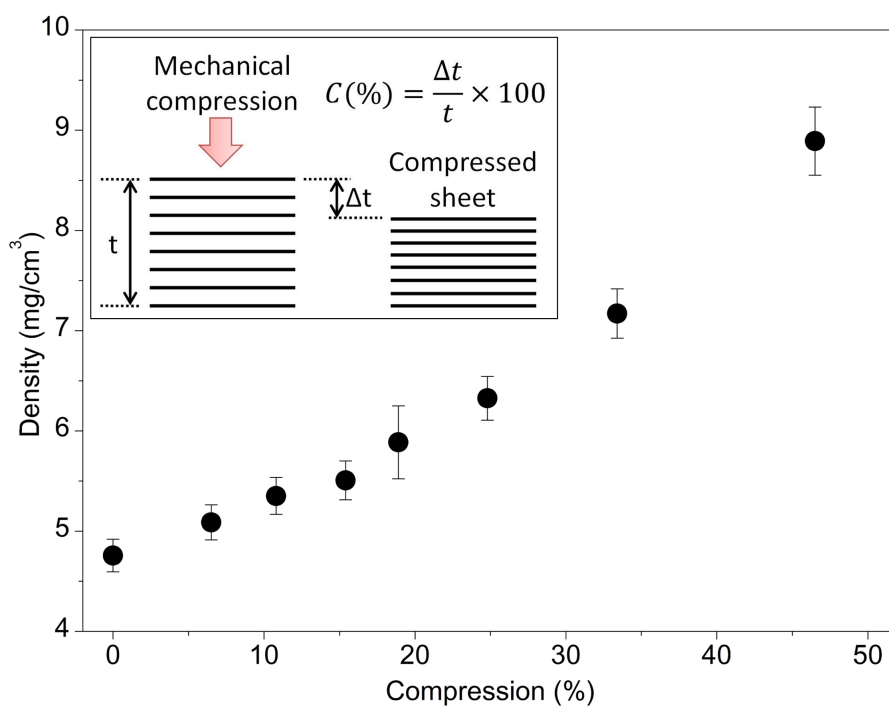


Figure 4-15. Density change of the CNT electrode as a function of the mechanical compression (The inset illustrates the mechanical compression of a planar CNT electrode.).

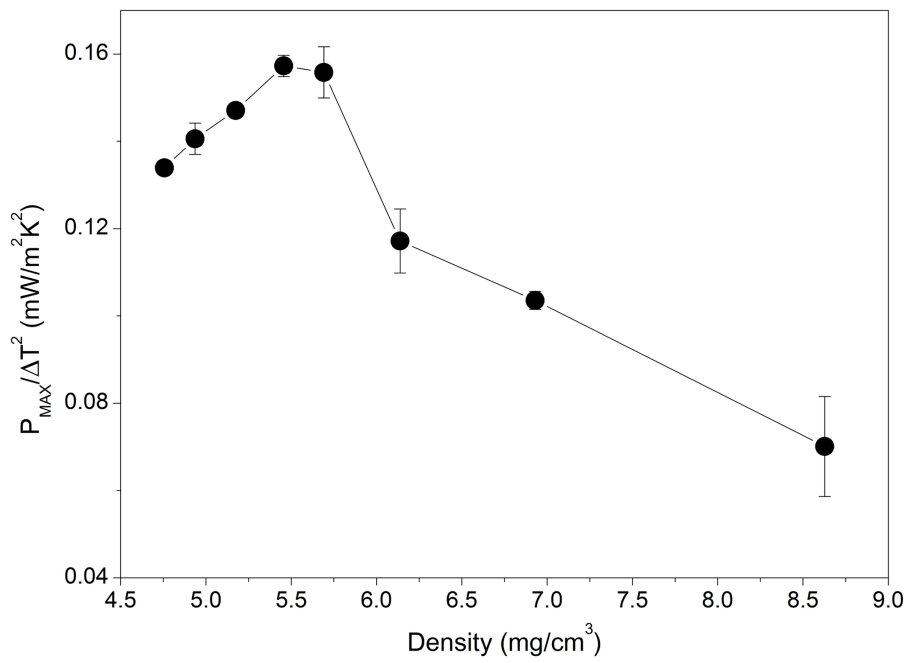


Figure 4-16. $P_{MAX}/\Delta T^2$ generated by the thermocell as a function of the electrode density.

The data in Figure 4-17 show the origin of this effect of sheet compression. The mass transport resistance increases with increasing level of compression, whereas the ohmic resistance decreases with increasing compression (inset of the Figure 4-17). Ohmic resistance decreases with increasing compression, because a shorter electron pathway to the external circuit results from an increased number of contacts between CNTs and a decreased electrode thickness. On the other hand, mass transport resistance, typically affected by ion accessibility into electrodes, is increased by compression, indicating sluggish ion diffusion within the compressed CNT network (Figure 4-18). Therefore, $P_{MAX}/\Delta T^2$ is maximized at an intermediate compression (15%), where mass transport resistance is not much affected by compression, but ohmic resistance is dramatically decreased.

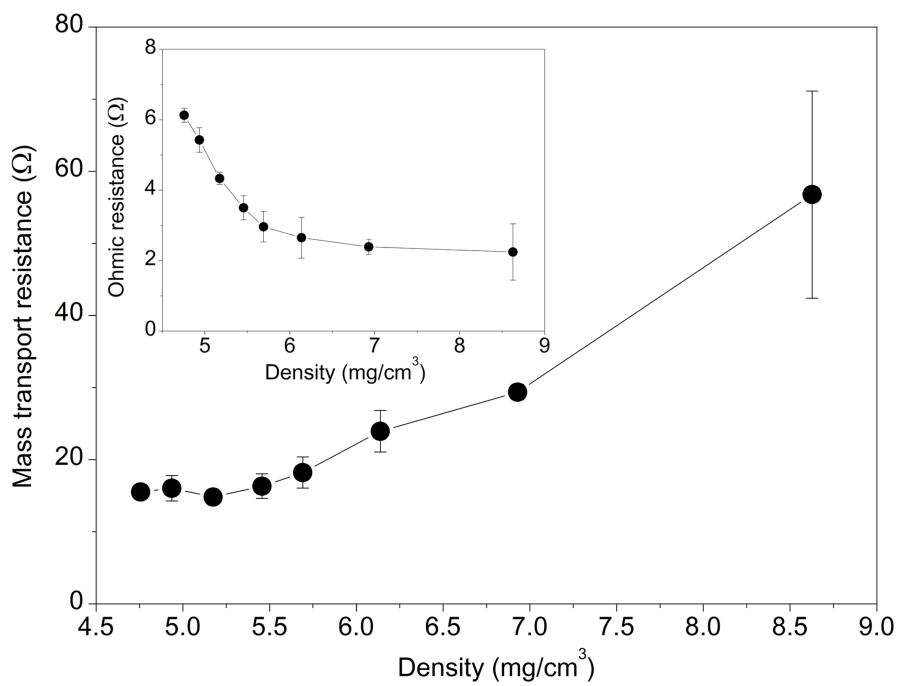


Figure 4-17. The dependence of mass transport and (inset) ohmic resistances on the electrode density.

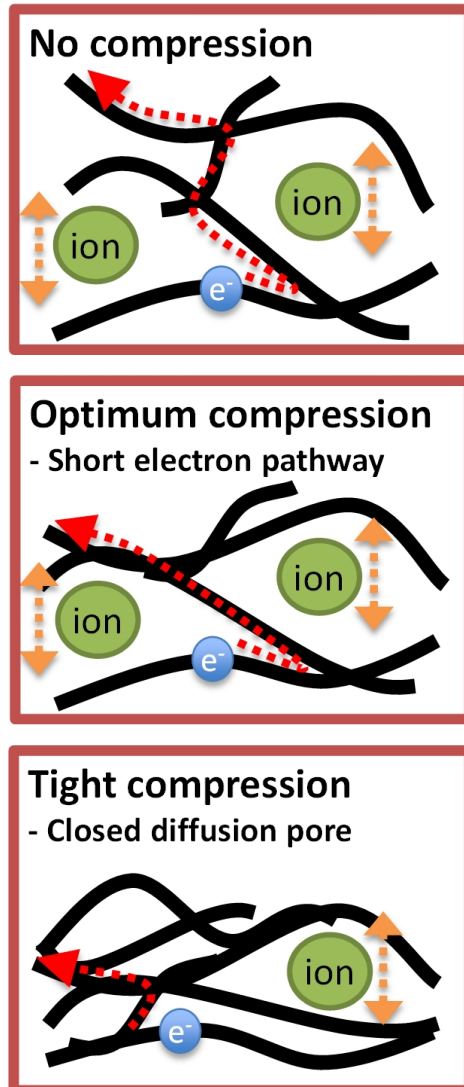


Figure 4-18. Schematic illustration of the effect of mechanical compression on the structure and properties of the CNT aerogel network. The ohmic resistance decreases with increasing compression, but too high a compression decreases pore size, thereby restricting ion diffusion.

4.4.4 Decoration CNT aerogel sheet with Pt nanoparticles

To realize further improvement in electrode performance, Pt nanoparticles were deposited on the thermally oxidized CNT aerogel sheet electrodes by chemical reduction of a platinum salt solution. This Pt nanoparticle deposition increases the electrode surface area for the thermocell reaction, and the catalytic activity of platinum reduces the charge transfer resistance [86]. The HR-TEM image of Figure 4-19 and 4-20a and the statistical size analysis of deposited Pt nanoparticles in Figure 4-20b show that platinum nanoparticles with an average diameter of 2.4 nm are uniformly deposited on the surfaces of individual CNTs and nanotube bundles to provide 86 wt% of Pt in the electrodes.

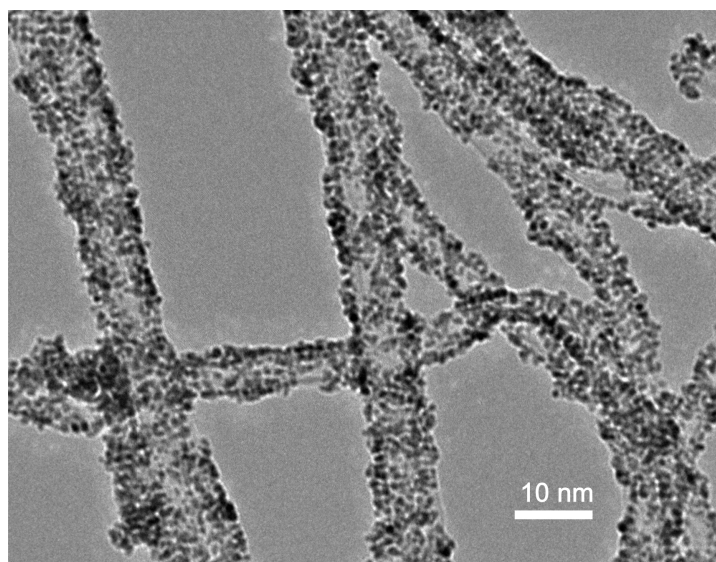
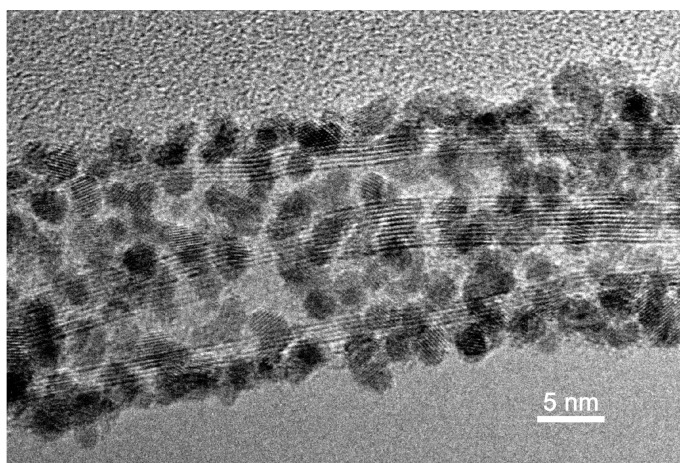
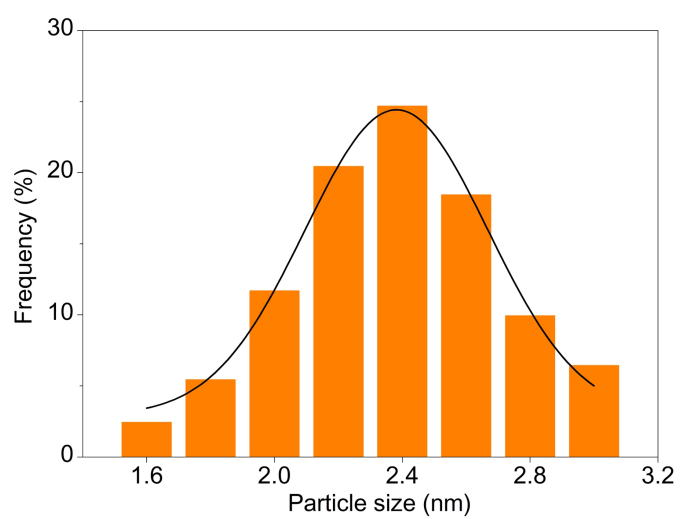


Figure 4-19. TEM image of CNTs uniformly decorated with Pt nanoparticles.



(a)



(b)

Figure 4-20. a) HR-TEM image of individual CNT decorated by Pt nanoparticles. b) Size distribution of Pt nanoparticles on CNTs.

Cyclic voltammetry (CV) measurements were used to obtain the changes in electroactive surface area (ESA) [87] and redox potential difference between oxidation and reduction that Pt deposition provided. The CV curves of Figure 4-21 indicate an increase in the faradaic peak current for the thermally oxidized sheet electrode and Pt-decorated thermally-oxidized sheet electrode (Pt-sheet) compared with that for the as-drawn sheet electrode. Moreover, the Pt-sheet has the highest faradaic current. This increased current can be attributed to the increased ESA, which according to the Randles-Sevcik equation is given by [88]:

$$I_p = 2.69 \times 10^5 \cdot ESA \cdot D^{1/2} \cdot n^{3/2} \cdot \nu^{1/2} \cdot C \quad (4.7)$$

where I_p is the faradaic peak current, D is the diffusion coefficient, ν is the potential scan rate, C is the concentration of probe molecule.

The redox potential differences and ESAs determined by CV are shown in Figure 4-22 for electrodes that are as-drawn, thermally oxidized, and platinum-deposited after chemical cleaning by thermal oxidation. This figure shows that the cleaned CNT electrode has a higher ESA and a smaller redox potential difference than the as-drawn CNT electrode, which led to the improved performance shown in Figure 4-13. The largest ESA and the lowest potential difference resulted (Figure 4-22) when Pt nanoparticles were deposited onto the cleaned surface of CNTs. These results indicate that the Pt-decorated sheet electrodes provide the highest performance in thermocells, because they yield the largest effective surface area and the greatest reduction in the potential difference between peaks for oxidation

and reduction. Electrochemical impedance spectroscopy (EIS) analysis was also performed to support the performance improvement. The equivalent series resistance, ESR (the intercept of the curve with the x-axis of the Nyquist plot [89] in the inset of Figure 4-23) is slightly reduced after Pt decoration. The Nyquist plot in Figure 4-23 shows that the charge transfer resistance (the diameter of the semicircle [90]) is lower for the thermally oxidized sheet than for the as-drawn sheet and that it is lowest for the Pt-decorated, thermally oxidized sheet. These observations from the EIS measurements agree with the CV results

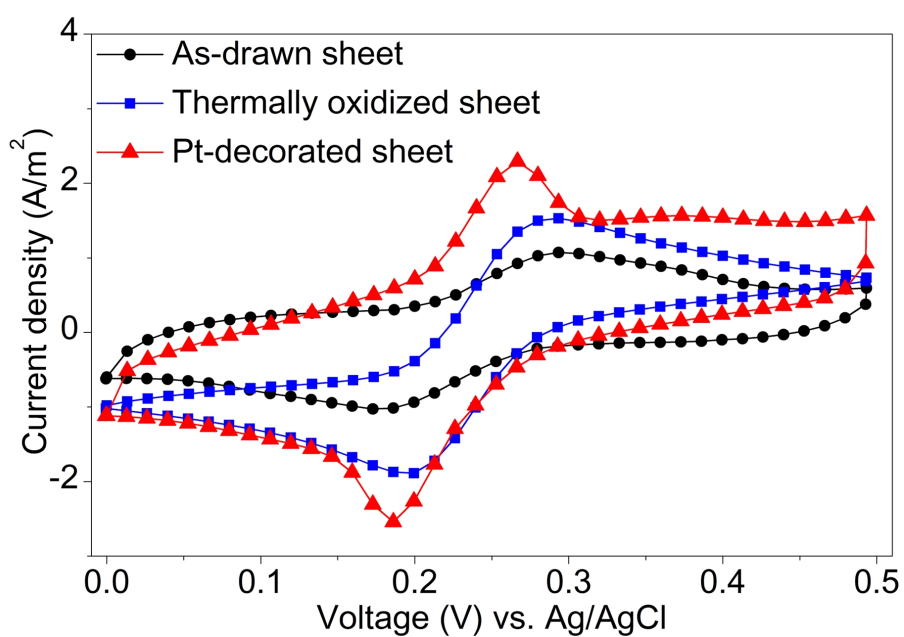


Figure 4-21. Cyclic voltammograms obtained at a 100 mV/s scan rate using as-drawn, thermally oxidized, and thermally oxidized and Pt deposited CNT electrodes.

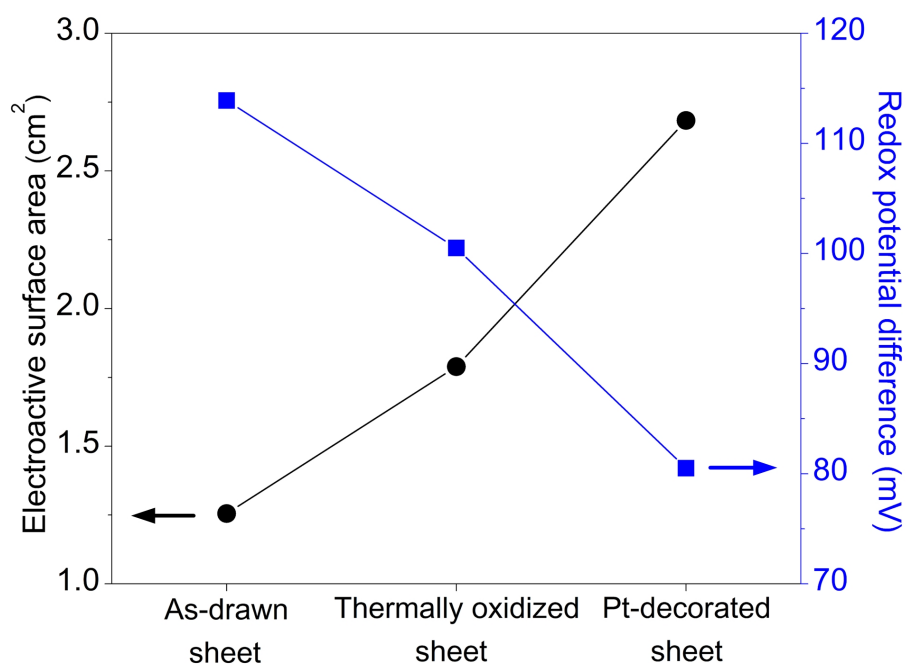


Figure 4-22. Electroactive surface area and redox potential difference for the above various CNT electrodes.

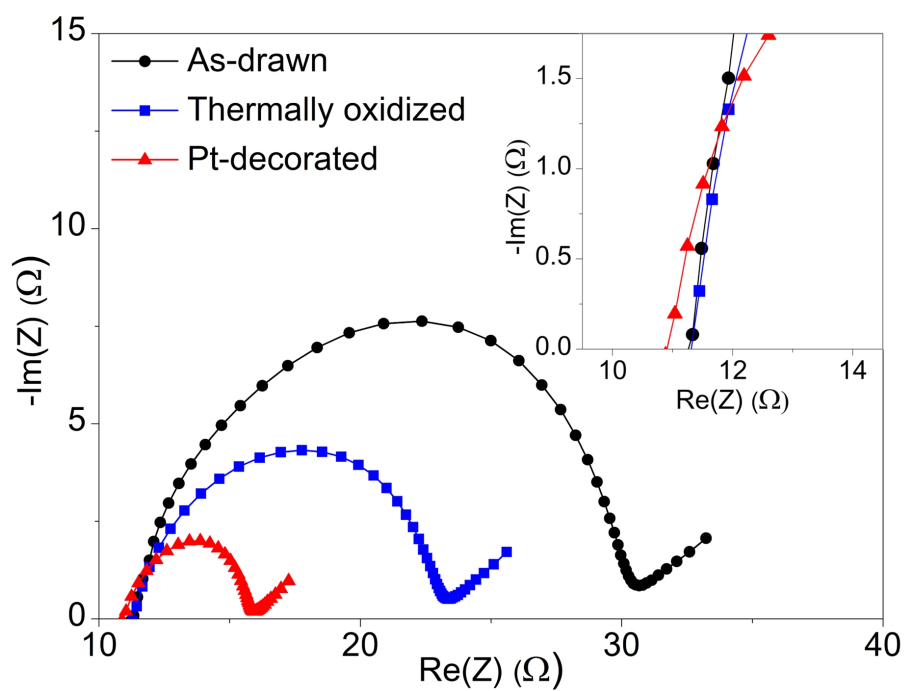


Figure 4-23. Nyquist impedance plots for various electrodes. The inset shows a close-up of the high frequency region of the curves.

4.4.5 Cylinder-type thermocell configuration

Building upon our results for planar electrodes, Thermocell performance was further optimized by using the cylindrical electrode configuration of Figure 4-5 (while deploying the same 0.4 M ferro/ferricyanide aqueous electrolyte as for the flat thermocells). The cylindrical electrodes pictured in this figure were fabricated by first using the apparatus of Figure 4-24 to wind a forest-drawn CNT sheet onto a 300 μm diameter tungsten wire (which facilitates current collection). The SEM images of Figure 4-25 show the realized highly uniform structure of the electrode sidewall and the orientation of the CNTs around the electrode circumference. Using the results of Figure 4-15 on the optimal degree of electrode compression to produce densification, a sheet electrode wound to a diameter of 3.5 mm was compressed to 3 mm diameter by using two grooved templates (shown in Figure 4-26) and inserted into a 3-mm inner diameter, cylindrical glass chamber to form the thermocell.

The volumetric density of as-drawn; thermally oxidized; thermally oxidized and Pt-decorated; and thermally oxidized, compressed, and Pt-decorated sheets for the cylindrical cell configuration are measured as 4.8, 2.9, 20.1 and 27.4, respectively.

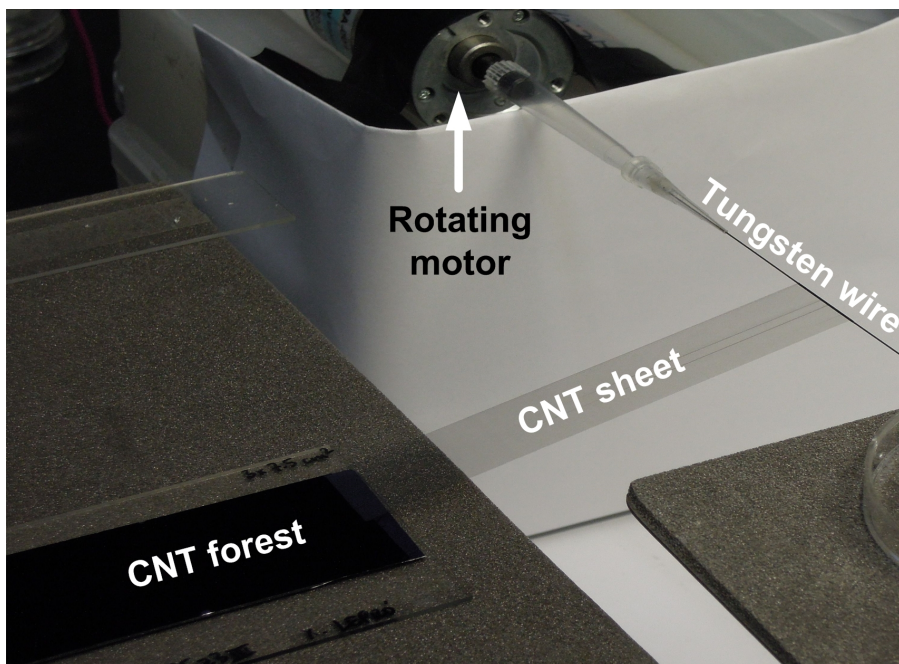


Figure 4-24. Experimental setup for preparation of cylindrical CNT electrode.

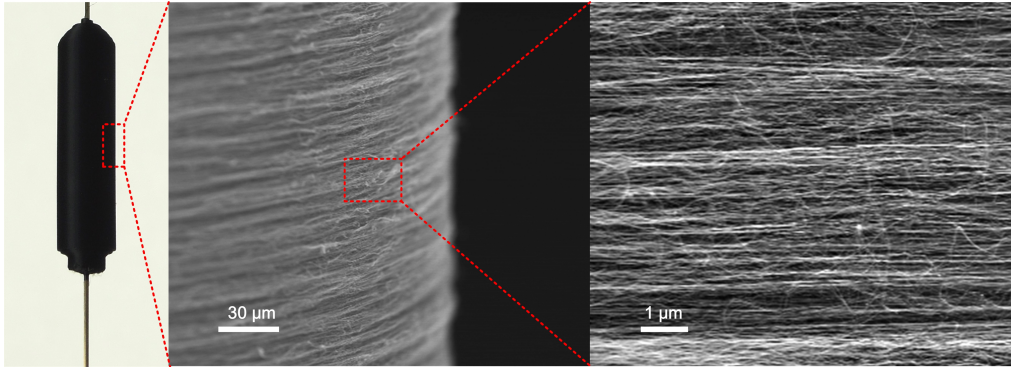


Figure 4-25. Photograph and SEM image of the CNT electrode.

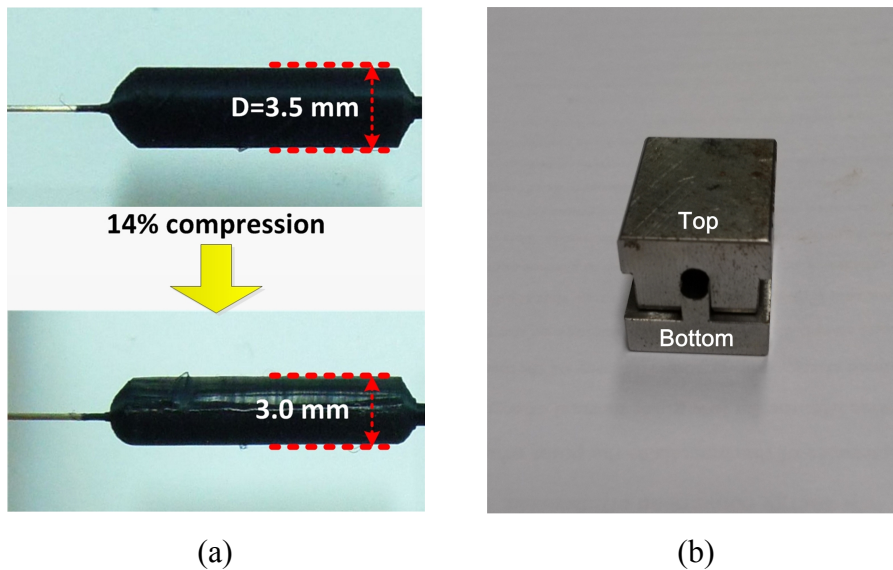


Figure 4-26. Optical images of a) cylindrical CNT electrode before (top) and after repeated compressions (bottom) in the compression jig (between which the cylindrical CNT sheet electrode was rotated about its long axis in the compression jig) and b) the two-part grooved template used as a compression jig for the compression of the cylindrical electrode.

The performance of the above thermocells containing differently prepared cylindrical CNT aerogel electrodes is presented in Figure 4-27 for $\Delta T \approx 51^\circ\text{C}$. The cylindrically configured as-drawn sheet electrode generates a P_{MAX} of 2.0 W/m^2 . These results show that removal of carbonaceous impurities by the described optimized thermal oxidation increases the power output to 3.7 W/m^2 , which is further increased for the cylindrical electrode thermocell to 6.0 W/m^2 when Pt nanoparticles are deposited onto the purified CNT aerogel sheets before assembly into cylindrical electrodes. Finally, the maximum power density was further enhanced to 6.6 W/m^2 when the cleaned, Pt-sheet electrode was laterally compressed. This output corresponds to an energy conversion efficiency of 4.3%, relative to the theoretically limiting Carnot cycle efficiency.

The open circuit voltage was $V_{\text{OC}} = 72 \text{ mV}$ and the ΔT thereby calculated (from this voltage and the Seebeck coefficient of 1.4 mV/K) was 51.4°C for all electrode types in the cylindrical thermocell configuration. The cell area, κ , and inter-electrode separation distance are $7.1 \times 10^{-6} \text{ m}^2$, 0.55 W/mK [91], and 2.5 cm , respectively. The short-circuit current obtained from as-drawn; thermally oxidized; thermally oxidized and Pt-decorated; and thermally oxidized, compressed, and Pt-decorated sheets in the cylindrical cell configuration are 0.8 , 1.5 , 2.3 and 2.6 mA , respectively. Using eq. 3.1, η values of 0.18 , 0.33 , 0.53 and 0.58% are attained through the use of cylindrical thermocell configuration for these cylindrical thermocells from differently processed CNT aerogel sheets, respectively.

The Carnot-relative energy conversion efficiency was calculated using eq. 3.1 and 3.2, the measured $\Delta T = 51.4^\circ\text{C}$, and a heat source temperature that

was held at $T_H = 100^\circ\text{C}$ for the experiments. The resulting calculated Carnot-relative efficiency was $\eta_r = 4.2\%$ for the optimized cylindrical thermocell (based on cylindrical electrodes made of thermally purified, optimally compressed, Pt-decorated CNT sheets), as shown in Figure 4-28. This thermocell efficiency is substantially higher than the previously reported record Carnot-relative for a thermocell, which is 2.63% [16].

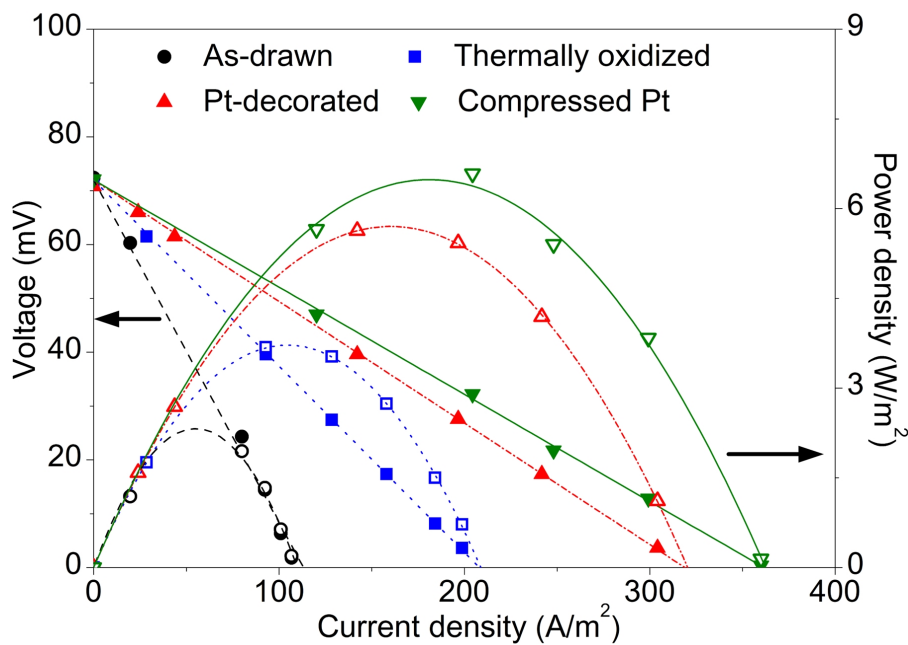


Figure 4-27. Cell voltage and power density versus current density for variously treated cell electrodes.

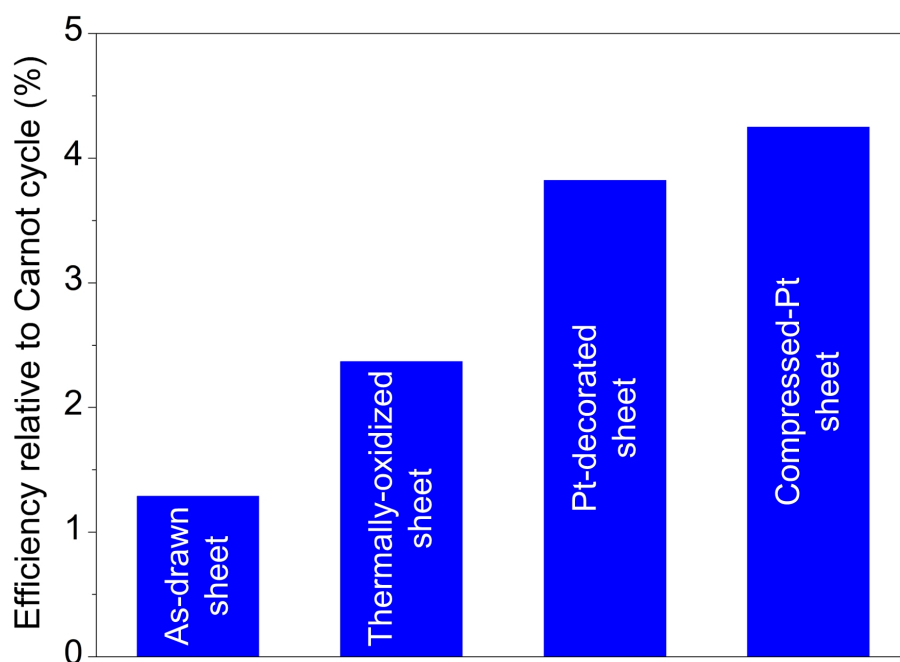


Figure 4-28. Energy conversion efficiency relative to a Carnot cycle for various CNT electrodes in the cylindrical cell configuration. All sheet samples (except the as-drawn) were purified by thermal oxidation before assembly into cylindrical electrodes.

4.5 Conclusion

A summary of data obtained is provided in Table 3 below. The thermo-electrochemical cell whose Carnot relative efficiency of 4.2% was described and the efficiency value is much higher than previously realized for a thermal-electrochemical energy harvester (2.6%). This thermocell uses structurally optimized CNT aerogel sheet electrodes, which are drawn from CNT forests and configured into jelly-roll-like scrolls, to maximize output power density. Normalized to cell cross-sectional area normal to a 51°C inter-electrode temperature difference, a power output of 2.53 mW/m²K² (maximum power density of 6.6 W/m²) was obtained simultaneously with a Carnot relative efficiency of 4.2%.

The ability to simultaneously obtain a record Carnot-relative efficiency (4.2%) and a record areal current density (6.6 W/m² for a temperature difference of only 51.4°C) bodes well for eventual practical deployment of thermo-electrochemical cells for harvesting low grade heat as electrical energy. This work demonstrates the importance of electrode purity, engineered porosity, and catalytic surfaces on thermocell performance and the ways that each predominately affects thermocell parameters. It is doubtful that thermal electrochemical cells will ever match the efficiencies obtained for costly thermoelectrics. However, potentially low cost (using future low-cost catalyst) and convenient deployability (like the demonstrated wrapping of flexible CNT sheet thermocells about hot pipes [4]) might eventually lead to their importance in the menagerie of means for practically harvesting thermal energy.

Table 3. Summary of data obtained from harvesting experiments performed using cylindrical thermocell.

| Electrode | As-drawn sheet | Thermally-oxidized sheet | Pt-decorated sheet | Compressed-Pt sheet |
|--|----------------|--------------------------|--------------------|---------------------|
| Density (mg/cm ²) | 4.8 | 2.9 | 20.1 | 27.4 |
| j_{sc} (A/m ²) | 112 | 205 | 331 | 367 |
| $P/\text{area} \cdot \Delta T^2$ (mW/m ² K ²) | 0.76 | 1.4 | 2.3 | 2.5 |
| $P/\text{mass} \cdot \Delta T^2$ (mW/kgK ²) | 16 | 48 | 11 | 9.2 |
| η_r (%) | 1.29 | 2.37 | 3.82 | 4.23 |

Chapter 5. Discussion and concluding remarks

The current dissertation is an attempt to develop plastic thermocells that consist of all pliable materials and to improve efficiency of thermocells using CNT aerogel sheet and multiple optimization strategies. With the plastic thermocell, waste thermal energy from arbitrary shaped heat sources can be scavenged. An investigation into the effects of removal of carbonaceous impurities, mechanical compression and decoration of platinum nanoparticles on thermal electrochemical cells' performance has been carried out. The enhanced understanding of these parameters has led to significant improvements in thermocell performance. Development of novel optimized CNT aerogel sheet has resulted in a record efficiency relative to a Carnot cycle of 4.3%.

While semiconductor-based solid-state thermoelectrics can reach at least ~20% of Carnot efficiency, the power conversion efficiencies of present thermocell is about ~4.3%. While major increases in the power conversion efficiencies are possible, based on increase of the effective thermoelectrochemical Seebeck coefficient and the ratio of ionic conductivity to thermal conductivity, it seems doubtful that electrochemical will ever exceed the thermal energy conversion efficiencies achievable for solid-state thermoelectrics. However, conventional solid-state thermoelectrics are expensive and inflexible, so they seem unsuitable for such applications as wrapping around a hot pipe that exists a chemical plant. In these applications, and many other where the thermal energy could otherwise be lost, the target is to maximize energy output as expressed as Wh/dollar, and

in this regime the electrochemical thermal cells might have major advantages (as suggested in a very preliminary way by previous comparison of Wh/dollar of solar and electrochemical thermocells [4]).

Development of plastic thermocell: To effectively harvest waste thermal energy from these arbitrary shaped heat sources, plastic thermocells with aqueous potassium ferricyanide/ferrocyanide electrolyte have been investigated as an alternative to conventional thermoelectrics for thermal energy harvesting. Plastic thermocells consist of all pliable materials such as polyethylene terephthalate (PET), fabrics, and wires. The plastic thermocell is flexible enough to be wearable on the human body and to be wrapped around cylindrical shapes. Hierarchical porous textiles coated with CNTs were also developed as an electrode to enhance the thermocell performance by lowering the three primary resistances. It has been shown that the thermocell charges up a capacitor when worn by a person on a T-shirt with a maximum output power density of 0.46 mW/m^2 . The electrical energy generated from waste pipe heat by a serial array of the thermocells can power a typical commercial LED whose turn-on voltage is 1.5 V. The results indicate that the thermocell developed here can serve as a self-sustainable energy source. The flexible thermo- electrochemical device introduced here should inspire further research in the area of waste heat recovery.

Improvement of thermocell efficiency: The deployed optimization strategies to improve thermocell efficiency involve use of CNT aerogel

sheets as electrodes, removal of low activity carbonaceous impurities that limit electron transfer kinetics, decoration of CNT sheets with catalytic platinum nanoparticles, mechanical compression of nanotube sheets to tune conductivity and porosity, and the utilization of cylindrical cell geometry. This thermocell uses structurally optimized CNT aerogel sheet electrodes, which are drawn from CNT forests and configured into jelly-roll-like scrolls, to maximize output power density. The output power density generated by thermocell with the optimized aerogel sheet reached 6.6 W/m^2 , which corresponds to a Carnot-relative efficiency (η_r) of 4.2%. To date this η_r is the highest reported value in thermocells. The ability to simultaneously obtain a record Carnot-relative efficiency (4.2%) and a record areal current density (6.6 W/m^2 for a temperature difference of only 51.4°C) bodes well for eventual practical deployment of thermo-electrochemical cells for harvesting low-grade heat as electrical energy. This work demonstrates the importance of electrode purity, engineered porosity, and catalytic surfaces on thermocell performance and the ways that each predominately affects thermocell parameters.

Bibliography

- [1] J. A. Turner, "A Realizable Renewable Energy Future", *Science*, 285, 687 (1999).
- [2] I. Dincer, "On thermal energy storage systems and applications in buildings", *Energy and Buildings*, 34, 377 (2002).
- [3] L. E. Bell, "Cooling, Heating, Generating Power, and Recovering Waste Heat with Thermoelectric Systems", *Science*, 321, 1457 (2008).
- [4] R. Hu; B. A. Cola; N. Haram; J. N. Barisci; S. Lee; S. Stoughton; G. Wallace; C. Too; M. Thomas; A. Gestos; M. E. d. Cruz; J. P. Ferraris; A. A. Zakhidov; R. H. Baughman, "Harvesting Waste Thermal Energy Using a Carbon-Nanotube-Based Thermo-Electrochemical Cell", *Nano Letters*, 10, 838 (2010).
- [5] M. Ujihara; G. P. Carman; D. G. Lee, "Thermal energy harvesting device using ferromagnetic materials", *Applied Physics Letters*, 91, (2007).
- [6] R. Shinnar; F. Citro, "Solar thermal energy: The forgotten energy source", *Technology in Society*, 29, 261 (2007).
- [7] R. H. Hammond; W. M. Risen Jr, "An electrochemical heat engine for direct solar energy conversion", *Solar Energy*, 23, 443 (1979).
- [8] H. Levin; C. F. Bonilla, "Thermogalvanic Potentials: I . The Application of Thermodynamics to Thermogalvanic Data (A Study

- of the Silver Chloride Electrode from 25° to 90°C)", *Journal of The Electrochemical Society*, 98, 388 (1951).
- [9] B. Burrows, "Discharge Behavior of Redox Thermogalvanic Cells", *Journal of The Electrochemical Society*, 123, 154 (1976).
- [10] T. Ikeshoji; S. K. Ratkje, "Thermoelectric Power of a Cell with Complex Formation", *Journal of The Electrochemical Society*, 133, 1107 (1986).
- [11] Y. Mua; T. I. Quickenden, "Power Conversion Efficiency, Electrode Separation, and Overpotential in the Ferricyanide/Ferrocyanide Thermogalvanic Cell", *Journal of The Electrochemical Society*, 143, 2558 (1996).
- [12] T. I. Quickenden; Y. Mua, "A Review of Power Generation in Aqueous Thermogalvanic Cells", *Journal of the Electrochemical Society*, 142, 3985 (1995).
- [13] C. B. Vining, "An inconvenient truth about thermoelectrics", *Nature Materials*, 8, 83 (2009).
- [14] A. Khaligh; Z. Peng; Z. Cong, "Kinetic Energy Harvesting Using Piezoelectric and Electromagnetic Technologies"; State of the Art", *Industrial Electronics, IEEE Transactions on*, 57, 850 (2010).
- [15] J. Tang; H.-T. Wang; D. H. Lee; M. Fardy; Z. Huo; T. P. Russell; P. Yang, "Holey Silicon as an Efficient Thermoelectric Material", *Nano Letters*, 10, 4279 (2010).
- [16] M. S. Romano; N. Li; D. Antiohos; J. M. Razal; A. Nattestad; S. Beirne; S. Fang; Y. Chen; R. Jalili; G. G. Wallace; R. Baughman; J. Chen,

- "Carbon Nanotube – Reduced Graphene Oxide Composites for Thermal Energy Harvesting Applications", *Advanced Materials*, 25, 6602 (2013).
- [17] T. J. Kang; S. L. Fang; M. E. Kozlov; C. S. Haines; N. Li; Y. H. Kim; Y. S. Chen; R. H. Baughman, "Electrical Power From Nanotube and Graphene Electrochemical Thermal Energy Harvesters", *Advanced Functional Materials*, 22, 477 (2012).
- [18] E. D. Eastman, "THERMODYNAMICS OF NON-ISOTHERMAL SYSTEMS", *Journal of the American Chemical Society*, 48, 1482 (1926).
- [19] E. D. Eastman, "THEORY OF THE SORET EFFECT", *Journal of the American Chemical Society*, 50, 283 (1928).
- [20] T. I. Quickenden; C. F. Vernon, "Thermogalvanic conversion of heat to electricity", *Solar Energy*, 36, 63 (1986).
- [21] A. J. deBethune; T. S. Licht; N. Swendeman, "The Temperature Coefficients of Electrode Potentials: The Isothermal and Thermal Coefficients—The Standard Ionic Entropy of Electrochemical Transport of the Hydrogen Ion", *Journal of The Electrochemical Society*, 106, 616 (1959).
- [22] P. D. Miller; A. B. Tripler; J. J. Ward, "The Application of Irreversible Thermodynamics to the Thermogalvanic Behavior of Copper - Copper Sulfate Systems", *Journal of The Electrochemical Society*, 113, 746 (1966).

- [23] J. N. Agar; C. Y. Mou; J. L. Lin, "Single-ion heat of transport in electrolyte solutions: a hydrodynamic theory", *The Journal of Physical Chemistry*, 93, 2079 (1989).
- [24] J. Newman, "Thermoelectric effects in electrochemical systems", *Industrial & Engineering Chemistry Research*, 34, 3208 (1995).
- [25] R. Venkatasubramanian; E. Siivola; T. Colpitts; B. O'Quinn, "Thin-film thermoelectric devices with high room-temperature figures of merit", *Nature*, 413, 597 (2001).
- [26] S. Iijima, "Helical microtubules of graphitic carbon", *Nature*, 354, 56 (1991).
- [27] H. L. Tang; J. G. Cyster, "Chemokine Up-Regulation and Activated T Cell Attraction by Maturing Dendritic Cells", *Science*, 284, 819 (1999).
- [28] C. Journet; W. K. Maser; P. Bernier; A. Loiseau; M. L. de la Chapelle; S. Lefrant; P. Deniard; R. Lee; J. E. Fischer, "Large-scale production of single-walled carbon nanotubes by the electric-arc technique", *Nature*, 388, 756 (1997).
- [29] A. G. Rinzler; J. Liu; H. Dai; P. Nikolaev; C. B. Huffman; F. J. Rodríguez-Macías; P. J. Boul; A. H. Lu; D. Heymann; D. T. Colbert; R. S. Lee; J. E. Fischer; A. M. Rao; P. C. Eklund; R. E. Smalley, "Large-scale purification of single-wall carbon nanotubes: process, product, and characterization", *Appl Phys A*, 67, 29 (1998).
- [30] M. Endo; K. Takeuchi; K. Kobori; K. Takahashi; H. W. Kroto; A. Sarkar, "Pyrolytic carbon nanotubes from vapor-grown carbon fibers", *Carbon*, 33, 873 (1995).

- [31] P. Nikolaev; M. J. Bronikowski; R. K. Bradley; F. Rohmund; D. T. Colbert; K. A. Smith; R. E. Smalley, "Gas-phase catalytic growth of single-walled carbon nanotubes from carbon monoxide", *Chemical Physics Letters*, 313, 91 (1999).
- [32] J. Liu; A. G. Rinzler; H. Dai; J. H. Hafner; R. K. Bradley; P. J. Boul; A. Lu; T. Iverson; K. Shelimov; C. B. Huffman; F. Rodriguez-Macias; Y.-S. Shon; T. R. Lee; D. T. Colbert; R. E. Smalley, "Fullerene Pipes", *Science*, 280, 1253 (1998).
- [33] I. W. Chiang; B. E. Brinson; A. Y. Huang; P. A. Willis; M. J. Bronikowski; J. L. Margrave; R. E. Smalley; R. H. Hauge, "Purification and Characterization of Single-Wall Carbon Nanotubes (SWNTs) Obtained from the Gas-Phase Decomposition of CO (HiPco Process)", *The Journal of Physical Chemistry B*, 105, 8297 (2001).
- [34] J.-M. Bonard; T. Stora; J.-P. Salvetat; F. Maier; T. Stöckli; C. Duschl; L. Forró; W. A. de Heer; A. Châtelain, "Purification and size-selection of carbon nanotubes", *Advanced Materials*, 9, 827 (1997).
- [35] S. Bandow; A. M. Rao; K. A. Williams; A. Thess; R. E. Smalley; P. C. Eklund, "Purification of Single-Wall Carbon Nanotubes by Microfiltration", *The Journal of Physical Chemistry B*, 101, 8839 (1997).
- [36] G. S. Duesberg; M. Burghard; J. Muster; G. Philipp, "Separation of carbon nanotubes by size exclusion chromatography", *Chemical Communications*, 435 (1998).
- [37] S. A. Curran; P. M. Ajayan; W. J. Blau; D. L. Carroll; J. N. Coleman; A. B. Dalton; A. P. Davey; A. Drury; B. McCarthy; S. Maier; A. Strevens,

- "A Composite from Poly(m-phenylenevinylene-co-2,5-dioctoxy-p-phenylenevinylene) and Carbon Nanotubes: A Novel Material for Molecular Optoelectronics", *Advanced Materials*, 10, 1091 (1998).
- [38] R. Bandyopadhyaya; E. Nativ-Roth; O. Regev; R. Yerushalmi-Rozen, "Stabilization of Individual Carbon Nanotubes in Aqueous Solutions", *Nano Letters*, 2, 25 (2001).
- [39] M. T. Martinez; M. A. Callejas; A. M. Benito; W. K. Maser; M. Cochet; J. M. Andres; J. Schreiber; O. Chauvet; J. L. G. Fierro, "Microwave single walled carbon nanotubes purification", *Chemical Communications*, 1000 (2002).
- [40] E. Vazquez; V. Georgakilas; M. Prato, "Microwave-assisted purification of HiPCO carbon nanotubes", *Chemical Communications*, 2308 (2002).
- [41] L. Kavan; P. Raptá; L. Dunsch; M. J. Bronikowski; P. Willis; R. E. Smalley, "Electrochemical Tuning of Electronic Structure of Single-Walled Carbon Nanotubes: In-situ Raman and Vis-NIR Study", *The Journal of Physical Chemistry B*, 105, 10764 (2001).
- [42] M. S. Dresselhaus; G. Dresselhaus; A. Jorio; A. G. Souza Filho; R. Saito, "Raman spectroscopy on isolated single wall carbon nanotubes", *Carbon*, 40, 2043 (2002).
- [43] E. F. Antunes; A. O. Lobo; E. J. Corat; V. J. Trava-Airoldi; A. A. Martin; C. Veríssimo, "Comparative study of first- and second-order Raman spectra of MWCNT at visible and infrared laser excitation", *Carbon*, 44, 2202 (2006).

- [44] M. S. Dresselhaus; G. Dresselhaus; R. Saito; A. Jorio, "Raman spectroscopy of carbon nanotubes", *Physics Reports*, 409, 47 (2005).
- [45] U. Ritter; P. Scharff; C. Siegmund; O. P. Dmytrenko; N. P. Kulish; Y. I. Prylutskyy; N. M. Belyi; V. A. Gubanov; L. I. Komarova; S. V. Lizunova; V. G. Poroshin; V. V. Shlapatskaya; H. Bernas, "Radiation damage to multi-walled carbon nanotubes and their Raman vibrational modes", *Carbon*, 44, 2694 (2006).
- [46] Y. Qi; M. C. McAlpine, "Nanotechnology-enabled flexible and biocompatible energy harvesting", *Energy & Environmental Science*, 3, 1275 (2010).
- [47] T. Hirai; K. Shindo; T. Ogata, "Charge and Discharge Characteristics of Thermochargeable Galvanic Cells with an $[\text{Fe}(\text{CN})_6]^{4-} / [\text{Fe}(\text{CN})_6]^{3-}$ Redox Couple", *Journal of the Electrochemical Society*, 143, 1305 (1996).
- [48] R. J. M. Vullers; R. van Schaijk; I. Doms; C. Van Hoof; R. Mertens, "Micropower energy harvesting", *Solid-State Electronics*, 53, 684 (2009).
- [49] V. Leonov; T. Torfs; P. Fiorini; C. Van Hoof, "Thermoelectric Converters of Human Warmth for Self-Powered Wireless Sensor Nodes", *Sensors Journal, IEEE*, 7, 650 (2007).
- [50] E. A. Aydin; I. Güler, "Recent advances on body-heat powered medical devices", *Recent Patents on Biomedical Engineering*, 4, 33 (2011).

- [51] G. J. Snyder; J. R. Lim; C.-K. Huang; J.-P. Fleurial, "Thermoelectric microdevice fabricated by a MEMS-like electrochemical process", *Nat Mater*, 2, 528 (2003).
- [52] J. Weber; K. Potje-Kamloth; F. Haase; P. Detemple; F. Völklein; T. Doll, "Coin-size coiled-up polymer foil thermoelectric power generator for wearable electronics", *Sensors and Actuators A: Physical*, 132, 325 (2006).
- [53] D. Kraemer; B. Poudel; H. P. Feng; J. C. Caylor; B. Yu; X. Yan; Y. Ma; X. Wang; D. Wang; A. Muto; K. McEnaney; M. Chiesa; Z. Ren; G. Chen, "High-performance flat-panel solar thermoelectric generators with high thermal concentration", *Nat Mater*, 10, 532 (2011).
- [54] K. T. Settaluri; H. Y. Lo; R. J. Ram, "Thin Thermoelectric Generator System for Body Energy Harvesting", *J Electron Mater*, 41, 984 (2012).
- [55] C. A. Hewitt; A. B. Kaiser; S. Roth; M. Craps; R. Czerw; D. L. Carroll, "Multilayered Carbon Nanotube/Polymer Composite Based Thermoelectric Fabrics", *Nano Letters*, 12, 1307 (2012).
- [56] T. J. Abraham; D. R. MacFarlane; J. M. Pringle, "Seebeck coefficients in ionic liquids -prospects for thermo-electrochemical cells", *Chemical Communications*, 47, 6260 (2011).
- [57] G. J. Snyder; E. S. Toberer, "Complex thermoelectric materials", *Nature Materials*, 7, 105 (2008).
- [58] L. Hu; M. Pasta; F. L. Mantia; L. Cui; S. Jeong; H. D. Deshazer; J. W. Choi; S. M. Han; Y. Cui, "Stretchable, porous, and conductive energy textiles", *Nano Letters*, 10, 708 (2010).

- [59] E. R. Nightingale, "Phenomenological Theory of Ion Solvation. Effective Radii of Hydrated Ions", *The Journal of Physical Chemistry*, 63, 1381 (1959).
- [60] E. A. d. Morais; G. Alvial; R. Longuinhos; J. M. A. Figueiredo; R. G. Lacerda; A. S. Ferlauto; L. O. Ladeira, "Enhanced electrochemical activity using vertically aligned carbon nanotube electrodes grown on carbon fiber", *Materials Research*, 14, 403 (2011).
- [61] J. I. Kim; S. J. Park, "A study of ion charge transfer on electrochemical behaviors of poly(vinylidene fluoride)-derived carbon electrodes", *Journal of Analytical and Applied Pyrolysis*, 98, 22 (2012).
- [62] Y. Juan; Q. Ke-qiang, "Preparation of Activated Carbon by Chemical Activation under Vacuum", *Environmental Science and Technology*, 43, 3385 (2009).
- [63] K. Babel; K. Jurewicz, "KOH activated carbon fabrics as supercapacitor material", *Journal of Physics and Chemistry of Solids*, 65, 275 (2004).
- [64] L. Bao; X. Li, "Towards textile energy storage from cotton T-shirts", *Advanced Materials*, 24, 3246 (2012).
- [65] G. Lota; K. Fic; E. Frackowiak, "Carbon nanotubes and their composites in electrochemical applications", *Energy & Environmental Science*, 4, 1592 (2011).
- [66] T. J. Kang; A. Choi; D. H. Kim; K. Jin; D. K. Seo; D. H. Jeong; S. H. Hong; Y. W. Park; Y. H. Kim, "Electromechanical properties of CNT-

- coated cotton yarn for electronic textile applications", *Smart Materials and Structures*, 20, 015004 (2011).
- [67] Q. Cheng; J. Tang; J. Ma; H. Zhang; N. Shinya; L. C. Qin, "Graphene and carbon nanotube composite electrodes for supercapacitors with ultra-high energy density", *Physical Chemistry Chemical Physics*, 13, 17615 (2011).
- [68] J. M. Nugent; K. S. V. Santhanam; A. Rubio; P. M. Ajayan, "Fast Electron Transfer Kinetics on Multiwalled Carbon Nanotube Microbundle Electrodes", *Nano Letters*, 1, 87 (2001).
- [69] R. Saliba; B. Agricole; C. Mingotaud; S. Ravaine, "Voltammetric and Impedance Analysis of Dimethyldioctadecylammonium/Prussian Blue Langmuir–Blodgett Films on ITO Electrodes", *The Journal of Physical Chemistry B*, 103, 9712 (1999).
- [70] Y. Xiao; J.-Y. Lin; S.-Y. Tai; S.-W. Chou; G. Yue; J. Wu, "Pulse electropolymerization of high performance PEDOT/MWCNT counter electrodes for Pt-free dye-sensitized solar cells", *Journal of Materials Chemistry*, 22, 19919 (2012).
- [71] C. F. Curtiss; R. B. Bird, "Multicomponent Diffusion", *Industrial & Engineering Chemistry Research*, 38, 2515 (1999).
- [72] X. Lu; Y. Xiao; Z. Lei; J. Chen, "Graphitized macroporous carbon microarray with hierarchical mesopores as host for the fabrication of electrochemical biosensor", *Biosensors and Bioelectronics*, 25, 244 (2009).
- [73] J. Zhao; F. Cheng; C. Yi; J. Liang; Z. Tao; J. Chen, "Facile synthesis of hierarchically porous carbons and their application as a catalyst

- support for methanol oxidation", *Journal of Materials Chemistry*, 19, 4108 (2009).
- [74] Z. Wang; E. R. Kiesel; A. Stein, "Silica-free syntheses of hierarchically ordered macroporous polymer and carbon monoliths with controllable mesoporosity", *Journal of Materials Chemistry*, 18, 2194 (2008).
- [75] Y. Deng; C. Liu; T. Yu; F. Liu; F. Zhang; Y. Wan; L. Zhang; C. Wang; B. Tu; P. A. Webley; H. Wang; D. Zhao, "Facile Synthesis of Hierarchically Porous Carbons from Dual Colloidal Crystal/Block Copolymer Template Approach", *Chemistry of Materials*, 19, 3271 (2007).
- [76] Y. Li; Z.-Y. Fu; B.-L. Su, "Hierarchically Structured Porous Materials for Energy Conversion and Storage", *Adv Funct Mater*, 22, 4634 (2012).
- [77] M. Zhang; S. Fang; A. A. Zakhidov; S. B. Lee; A. E. Aliev; C. D. Williams; K. R. Atkinson; R. H. Baughman, "Strong, Transparent, Multifunctional, Carbon Nanotube Sheets", *Science*, 309, 1215 (2005).
- [78] X. Jining; Z. Nanyan; K. V. Vijay, "Functionalized carbon nanotubes in platinum decoration", *Smart Materials and Structures*, 15, S5 (2006).
- [79] E. A. Ali; N. G. Yuri; H. B. Ray, "Mirage effect from thermally modulated transparent carbon nanotube sheets", *Nanotechnology*, 22, 435704 (2011).

- [80] A. A. Wragg; A. A. Leontaritis, "Local mass transfer and current distribution in baffled and unbaffled parallel plate electrochemical reactors", *Chemical Engineering Journal*, 66, 1 (1997).
- [81] P. Cañizares; J. García-Gómez; I. Fernández de Marcos; M. A. Rodrigo; J. Lobato, "Measurement of Mass-Transfer Coefficients by an Electrochemical Technique", *Journal of Chemical Education*, 83, 1204 (2006).
- [82] J.-M. Moon; K. H. An; Y. H. Lee; Y. S. Park; D. J. Bae; G.-S. Park, "High-Yield Purification Process of Singlewalled Carbon Nanotubes", *The Journal of Physical Chemistry B*, 105, 5677 (2001).
- [83] H.-T. Fang; C.-G. Liu; C. Liu; F. Li; M. Liu; H.-M. Cheng, "Purification of Single-Wall Carbon Nanotubes by Electrochemical Oxidation", *Chemistry of Materials*, 16, 5744 (2004).
- [84] A. G. Rinzler; J. Liu; H. Dai; P. Nikolaev; C. B. Huffman; F. J. Rodriguez-Macias; P. J. Boul; A. H. Lu; D. Heymann; D. T. Colbert; R. S. Lee; J. E. Fischer; A. M. Rao; P. C. Eklund; R. E. Smalley, "Large-scale purification of single-wall carbon nanotubes: Process, product, and characterization", *Applied Physics A: Materials Science and Processing*, 67, 29 (1998).
- [85] H. Im; H. Moon; J. Lee; I. Chung; T. Kang; Y. Kim, "Flexible thermocells for utilization of body heat", *Nano Res.*, 7, 1 (2014).
- [86] J. M. Rubi; S. Kjelstrup, "Mesoscopic Nonequilibrium Thermodynamics Gives the Same Thermodynamic Basis to Butler–Volmer and Nernst Equations", *The Journal of Physical Chemistry B*, 107, 13471 (2003).

- [87] M. Pacios; M. del Valle; J. Bartroli; M. J. Esplandiu, "Electrochemical behavior of rigid carbon nanotube composite electrodes", *Journal of Electroanalytical Chemistry*, 619–620, 117 (2008).
- [88] P. Papakonstantinou; R. Kern; L. Robinson; H. Murphy; J. Irvine; E. McAdams; J. McLaughlin; T. McNally, "Fundamental Electrochemical Properties of Carbon Nanotube Electrodes", *Fullerenes, Nanotubes and Carbon Nanostructures*, 13, 91 (2005).
- [89] S.-M. Park; J.-S. Yoo, "Peer Reviewed: Electrochemical Impedance Spectroscopy for Better Electrochemical Measurements", *Analytical Chemistry*, 75, 455 A (2003).
- [90] J. E. B. Randles, "Kinetics of rapid electrode reactions", *Discussions of the Faraday Society*, 1, 11 (1947).
- [91] M. Romano; S. Gambhir; J. Razal; A. Gestos; G. Wallace; J. Chen, "Novel carbon materials for thermal energy harvesting", *J Therm Anal Calorim*, 109, 1229 (2012).

초 록

자원 부족의 문제가 심각히 대두되면서 낮은 등급의 폐열 수집에 대한 관심이 고조되고 있다. 폐열 수집 기술의 확산을 위해서는 낮은 에너지 변환 효율을 개선하고 에너지 수집 장치의 단가를 줄이는 노력이 필요하다. 온도차 부식 전지 혹은 열-전기화학 전지로도 알려진 열전지는 전해질의 전기화학적 산화/환원 전위의 온도 의존성에 기반하여 전력을 생산한다. 따라서 열전지 기술은 폐열 에너지 회수를 위한 가장 효과적인 대처 기술로 최근 주목을 받고 있다. 열전지는 온도차를 갖는 양단 전극과 산화/환원 매개체로 구성된다. 상대 전극에 비해 높은 온도를 갖는 음극에서는 매개체의 산화 반응이 발생하며, 생성된 전자를 전극으로 전달한다. 전극으로 전달된 전자는 외부 부하를 통해 양극으로 전달되고, 전해질 내에 반응물은 상대 전극으로 이동한다. 이를 통해 열전지는 전력을 생산한다.

대규모의 발전소와 산업시설에서 많은 양의 폐열이 발생한다. 막대한 양의 폐열은 대부분 파이프와 같은 곡면 형태의 열원으로 방출된다. 이러한 곡면 열원의 폐열을 효과적으로 회수하기 위해 유연 열전지를 제작하였다. PET 필름과 섬유 소재로 구성된 열전지는 파이프 또는 인체에 부착할 수 있어 효과적으로 폐열 에너지를 수집할 수 있다. 유연 열전지의 직렬 연결을 통해 파이프의 폐열을 전기로 변환하여

LED 를 구동하였다. 또한, 열전지를 티셔츠에 탑재하여 인체로부터 전기를 생산하여 캐패시터에 충전하는데 성공하였다.

열전지 기술은 열-전기에너지의 직접 변환, 단순한 구성요소, 반영구적 내구성, 낮은 유지비용 및 탄소 무배출이라는 장점을 가진다. 하지만, 열전지의 에너지 변환효율이 낮은 단점을 가지고 있어 추후 상업적 이용을 위해서는 에너지 변환효율의 향상이 필요하다. 열전지 성능의 주된 비가역 손실 원인은 다음과 같이 크게 세가지로 나눌 수 있다. 1) 전극 재료와 산화/환원 매개체 경계에서의 활성화 손실, 2) 전해질 용액의 낮은 이온 전도도에 기인한 저항 손실 및 3) 전극 및 전지 내 물질 수송 손실. 기존의 효율 향상연구는 개별적인 손실에 집중한 반면, 본 연구에서는 세가지의 주된 비가역 손실을 해소하기 위해 전극의 선택과 후처리 기법을 적용하였다. 전극 재료는 물질 수송 능력이 뛰어난 탄소나노튜브 에어로젤을 선택하였고, 탄소나노튜브 표면의 비정질 탄소를 제거하고 균일한 백금 나노입자를 형성하여 활성화 손실을 감소시켰다. 마지막으로 기계적 압축 변위를 조절하여 저항 손실 또한 줄일 수 있었다. 최적화된 탄소나노튜브 에어로젤을 열전지의 전극으로 활용한 결과, 51°C 의 온도차에서 6.6 W/m² 의 전력을 생산하였다. 이는 카르노 대비 4.2%의 효율에 해당하며, 기존 최고 효율인 2.6% (카르노 대비 효율)를 크게 뛰어넘은 결과이다.

키워드: 탄소나노튜브, 열-전기화학 전지, 폐열 회수, 고효율 열전지,
유연 열전지

학번: 2008-30863